Energy and Charge Transfer in Organic Materials and Its Spectroscopic Signature: An Ab Initio Approach

by

Kyle Luke Williams

A dissertation submitted in partial fulfillment
of the requirements for the degree of
Doctor of Philosophy
(Chemistry)
in the University of Michigan
2018

Doctoral Committee:

Professor Eitan Geva, Chair
Professor Kevin Kubarych
Professor Jennifer Ogilvie
Assistant Professor Paul Zimmerman

Kyle L. Williams
klwill@umich.edu
ORCID iD: 0000-0002-7610-555X

In loving memory of Christopher Williams.

ACKNOWLEDGEMENTS

First and foremost, I would like to express my sincerest thanks to Prof. Eitan Geva for his support and encouragement throughout the length of my Ph.D. I am truly grateful for his compassion and understanding during a time of personal turmoil, and for his confidence in me. I would also like to acknowledge my committee members, Prof. Kevin Kubarych, Prof. Jennifer Ogilvie, and Prof. Paul Zimmerman, for their guidance during this endeavor. Additionally, I would like to thank my advisor at Montclair State University, Dr. Johannes Schelvis, for inspiring me to pursue this degree.

I would also like to thank my fellow Geva lab members, past and present, for their collaboration and thoughtful discussions, including Dr. Xiang Sun, Dr. Surma Talapatra, Dr. Myeong Lee, Michael Lenard, and Ellen Mulvihill. I would like to specifically thank Dr. Alexander Schubert for his guidance and support on the organic scintillation project, as well as Dr. Heidi Phillips–Hendrickson for her encouragement and assistance on the *compute-to-learn* project during its nascent stages. I would additionally like to acknowledge Blair Winograd and Alicia Welden for their contributions to the *compute-to-learn* project.

I also would like to express my gratitude to my parents, Mark and Candice Williams, for always believing in me. Their love and encouragement has been the foundation for my success, and I am eternally grateful for the sacrifices that they have made. Additionally, I would like to thank my brother, Jonathan Williams, particularly for his assistance with my other responsibilities while I worked feverishly to

complete this dissertation.

I would like to also acknowledge Jake Boissonnault, Samuel Esarey, Nathan Ulrich, Molly Bilderback–Ulrich, Kyle Ferguson, Jacob Lutter, Isabel Colon-Bernal, and Reese (the dog), for their friendship over these past five years, and for the fun and enjoyment that we have had. Finally, I would like to recognize my beloved dog, Izzy, who rescued me as much as I rescued her, and serves as a constant source of comfort.

TABLE OF CONTENTS

CHAPTER

LIST OF FIGURES

Figure

LIST OF TABLES

Table

LIST OF ABBREVIATIONS

2DIR two-dimensional infrared spectroscopy

CDFT constrained DFT

C–PCM conductor-like polarizable continuum model

CT charge transfer

DFT density functional theory

DMA *N,N*–dimethylaniline

DOF degrees of freedom

FCD fragment charge difference

FGR Fermi's golden rule

FOM figure of merit

GGA generalized gradient approximation

GSIs graduate student instructors

HF Hartree–Fock

HOMO highest occupied molecular orbital

HRFs Huang–Rhys factors

IC Internal conversion

IRB Institutional Review Board

ISC intersystem crossing

KS Kohn–Sham

LDA local density approximation

LR long-range

LUMO lowest unoccupied molecular orbital

LSC linearized semiclassical

MD molecular dynamics

OFETs organic field-effect transistors

OLEDs organic light-emitting diodes

OPVs organic photovoltaics

OT–RSH optimally-tuned RSH

OT–SRSH optimally-tuned screened RSH

PCBM phenyl–C_{61}–butyric acid methyl ester

PCM polarizable continuum model

PES potential energy surface

PSD pulse-shape discrimination

RSH range-separated hybrid

SOC Spin–orbit coupling

SR short-range

STR Stark tuning rate

TDDFT time-dependent density functional theory

THF tetrahydrofuran

TTA triplet–triplet annihilation

VSEs vibrational Stark effects

xc exchange–correlation

ABSTRACT

Energy and charge transfer processes in organic materials have received a tremendous amount of attention in recent years, due to their impact on functionality within a wide range of applications. One prominent example is the field of organic photovoltaics (OPVs), where significant improvements in power conversion efficiency and durability have been achieved over the last decade. Another example is organic scintillators, which have seen a renewed interest due to the constrained supply of helium–3 gas, as well as their ability to discriminate between types of ionizing radiation. Advancement in the design of organic photovoltaic and luminescent materials can be facilitated by molecular level insights into the processes of energy transfer, gained through both experimental observations and theoretical and computational modeling. Thus, this thesis utilizes computational techniques to investigate excited states, and their spectroscopic signatures, in molecular systems that are experimentally relevant for OPVs and organic scintillators.

In Chapter II of this thesis, a computational protocol based on density functional theory (DFT) is presented for calculating the dependence of the vibrational frequency of a carbonyl reporter mode on the electronic state of the molecular system, in the context of charge transfer (CT) in organic molecules. This protocol was utilized to study a system consisting of a phenyl–C_{61}–butyric acid methyl ester electron acceptor with a *N,N*–dimethylaniline donor, in which small frequency shifts of less than 4 cm^{-1} were observed between the ground state and the CT excited state. A Stark tuning rate of 0.768 cm^{-1}/(MV/cm) was calculated between the vibrational frequency and

the electric field.

In Chapter III of this thesis, the CT process in a carotenoid–porphyrin–C_{60} molecular triad was investigated in its two primary conformations (bent/linear) with an explicit tetrahydrofuran solvent via molecular dynamics. Vibrational frequency distributions were calculated for the amide I mode and found to be sensitive to the three electronic states relevant to CT: the $\pi\pi^*$ excited state, the porphyrin-to-C_{60} CT state, and the carotenoid-to-C_{60} charge-separated state, with shifts as large as 40–60 cm^{-1} observed between the CT1 and CT2 states. Rate constants between these states were calculated with a hierarchy of approximations based on the linearized semiclassical method. The CT process was determined to occur via a two-step mechanism, $\pi\pi^* \rightarrow \mathrm{CT1} \rightarrow \mathrm{CT2}$, where the second step is mediated by the bent-to-linear conformation change.

In Chapter IV of this thesis, the role of intersystem crossing (ISC) from S_1 to T_n in the pulse-shape discrimination (PSD) ability of single-crystal *trans*–stilbene was investigated. Time-dependent DFT was used with the newly developed OT–SRSH–PCM method to calculate the excited states, and an equilibrium Fermi's golden rule approach was employed to calculate transition rate constants. The ISC rates were found to be too slow to compete with prompt fluorescence, and thus do not significantly impact the PSD ability. Deuteration of *trans*–stilbene was found to have a retarding effect on the ISC rates, with rate constants reduced by as much as 30%.

Finally, in Chapter V of this thesis, a novel compute-to-learn pedagogy is presented, in which students design and develop interactive demonstrations of physical chemistry concepts in a peer-led studio environment. The rationale behind the pedagogy and improvements made over the course of three iterations are discussed, as well as an initial assessment of the pedagogy conducted via end-of-semester interviews.

CHAPTER I

Introduction

1.1 Charge Transfer in Organic Materials

Organic materials offer a wide variety of applications and have received a great deal of interest in recent decades, particularly in the area of organic electronics.[1–4] In fact, organic semiconductors have seen tremendous advancement in technologies such as organic light-emitting diodes (OLEDs), organic field-effect transistors (OFETs), and organic photovoltaics (OPVs).[5–9] Organic materials can offer significant advantages over traditional semiconductor materials, but also typically have some limitations. In the case of OPVs, they allow for flexible form factors and offer significant cost savings, but power conversion efficiencies are not yet able to compete with inorganic photovoltaics.[10] The performance of OPVs depends on the various energy and charge transfer processes that occur in the π-conjugated materials.[1] A better fundamental understanding of these processes, as well as improved methods of studying them, are therefore critical to continued advancement.

Photoinduced charge transfer (CT) in OPV thin-films has been studied by Asbury and coworkers,[11–22] utilizing ultrafast two-dimensional infrared spectroscopy (2DIR) techniques that take advantage a vibrational reporter mode. The frequency of the mode is sensitive to vibrational Stark effects (VSEs)[14,23,24] that arise from changes in the local electric field. VSEs have been used with enzymes to map frequency shifts of vibrational probes to changes in the electric field induced by mutations in the active site.[23,25–27] To examine whether this technique can be applied to obtain a time-resolved picture of CT processes in OPVs, we have developed protocols based on density functional theory (DFT) for calculating the dependence of the vibrational frequency on the electronic state of the molecular system. A brief overview of DFT is provided in the next section, as well as a method for constraining charges and calculating CT states.

1.1.1 Density Functional Theory and Charge Constraints

Kohn–Sham (KS) DFT is based on the foundational theorems of Hohenberg and Kohn,[28] proving that the ground state energy is determined by the electron density and that the density obeys the variational principle. This showed that there is a direct relationship between the electron density and the wave function, as $\rho \rightarrow v_{\text{ext}} \rightarrow \Psi_0$, but it did not offer any advantage over molecular orbital theory.[29] Kohn and Sham, however, devised an approach that involves using a fictitious system of non-interacting electrons that has the same density as the real system of interest with electrons that do interact.[30] In this formalism, the ground state energy can be written as a functional of the density:

$$E[\rho] = F_{\text{KS}}[\rho] + \int \mathrm{d}r\, v(r)\rho(r) \tag{1.1}$$

where $\rho(r)$ is the electron density, $v(r)$ is the external potential, and $F_{\text{KS}}[\rho] = T_s[\rho] + E_H[\rho] + E_{xc}[\rho]$, in which $T_s[\rho]$ is the non-interacting kinetic energy, $E_H[\rho]$ is the classical Coulomb electron repulsion energy, and $E_{\text{xc}}[\rho]$ is the exchange–correlation (xc) energy.[31] Variational minimization with respect to the orbitals yields

$$-\frac{1}{2}\nabla^2\psi_i + v_{\text{KS}}(r)\psi_i = \epsilon_i\psi_i \tag{1.2}$$

where ψ_i and ϵ_i are the orbitals and energies, respectively, and $v_{\mathrm{KS}}(r)$ is given by

$$v_{\mathrm{KS}}(r) = v_{\mathrm{ext}}(r) + v_{\mathrm{el}}(r) + \frac{\delta E_{xc}[\rho]}{\delta\rho(r)} \tag{1.3}$$

in which $\delta E_{xc}[\rho]/\delta\rho(r)$ is the functional derivative of E_{xc} with respect to ρ.

DFT is exact in principle, but the explicit form of the xc functional is not known and must therefore be approximated in practice.[29] While Kohn and Sham initially proposed an xc functional based on the simple local density approximation (LDA), numerous functionals have since been developed based on increasingly more sophisticated models. Density functionals are often categorized as belonging to rungs on "Jacob's DFT Ladder",[32] with the first four rungs consisting of LDA, generalized gradient approximation (GGA), meta–GGA, and hybrid density functionals, respectively. Performance typically improves with each rung of the ladder, with hybrid functionals being most widely used (e.g., the B3LYP functional).[33,34] Traditional global hybrid functionals, which incorporate a portion of exact Hartree–Fock (HF) exchange energy, perform poorly for the case of charge transfer, whereas so-called range-separated hybrid (RSH) functionals, which are detailed in Section 1.2.2, have been shown to perform well.[35]

Constraints can be imposed on properties such as charge or spin via an approach known as constrained DFT (CDFT). This involves supplementing the DFT energy functional, $E[\rho(r)]$, with a Lagrange multiplier of the general form[36]

$$E(N) = \min_{\rho} \max_{V} \left(E[\rho(r)] + W[\rho, V; N]\right) \tag{1.4}$$

where $W[\rho, V; N]$ is spin-dependent and given by

$$W[\rho, V; N] \equiv V \left(\sum_{\sigma} \int \mathrm{d}r\, w^{\sigma}(r) \rho^{\sigma}(r) - N \right) \tag{1.5}$$

Here, V is the Lagrange multiplier, N is the number of electrons, and w^{σ} is a weight function of spin σ that defines the property of interest. Using a population analysis scheme, such as that of Becke,[37] the charge can be constrained on molecular fragments.[38] This provides a direct way to calculate CT excited states at a cost similar to a standard DFT calculation. We utilize this method in Chapters II and III to investigate the spectroscopic signature of CT in organic donor–acceptor molecules.

1.2 Organic Scintillators and Pulse-Shape Discrimination

Organic scintillators have seen a renewed interest in recent years, due in part to the constrained supply of ^{3}He gas, which is widely used for neutron detection.[39] Organic scintillators also have the unique ability to distinguish between types of ionizing radiation, such as neutron and gamma particles (specifically, uncharged particles).[40] In these materials, ionizing radiation results in a complex cascade of events that ultimately leads to the emission of light, which can be analyzed by means of photomultipliers.[41] Incident particles produce activated species (excitations and ionizations) through central and distant collisions, as well as Compton scattering, generating a cylindrical path of high activation density referred to as the track. A schematic illustration of the distribution of activations is shown in Figure 1.1.

Slow secondary electrons are mainly confined to the track and contribute to the high concentration of activation, whereas fast secondary electrons, caused by central collisions, travel outside the track and lead to small highly-activated regions. The high energy excitations consist of singlet states (S_n), produced primarily via distant collisions and inelastic scattering, and triplet states (T_n), created primarily by ion–electron recombination. Outside of the densely activated areas, where interactions are negligible, excited species will undergo rapid internal conversion down to S_1 and T_1, which leads to prompt fluorescence ($\mathrm{S}_1 \rightarrow \mathrm{S}_0$). In regions of high activation concentration, however, interactions between excited species are more important and can

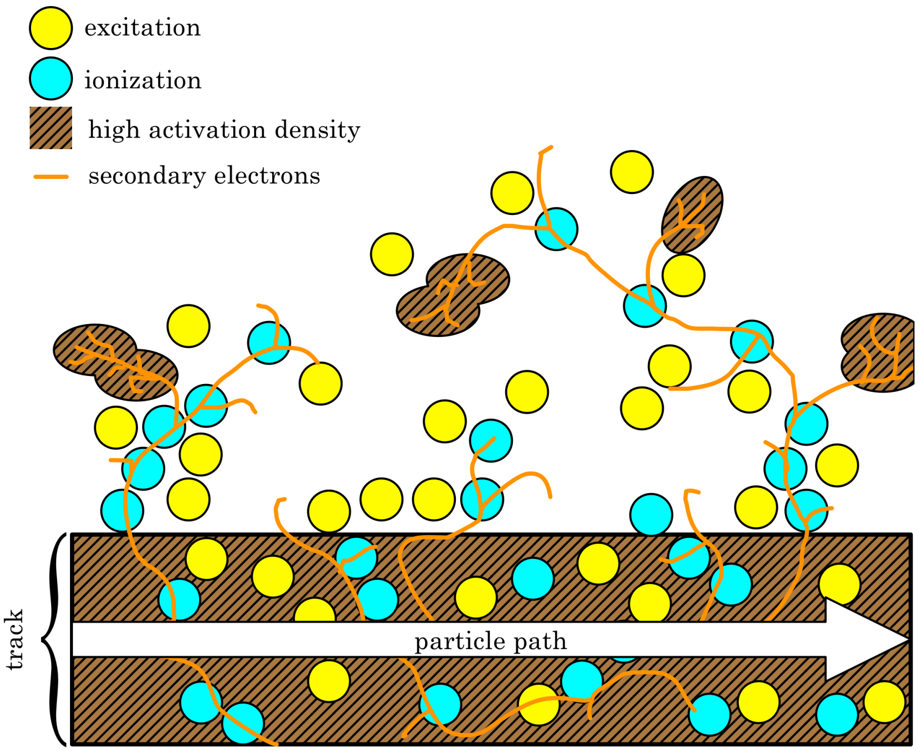

Figure 1.1: A schematic illustration of the distribution of activations caused by a charged particle in an organic scintillator, adapted from Reference 41.

produce ionizations (e.g., $S_n + S_m \rightarrow S_0 + [I^+ + e^-]$). Subsequent ion recombinations lead to higher concentrations of triplet states, and thus triplet–triplet interactions play an important role as well. In fact, a delayed fluorescence process occurs via formation of S_1 states due to triplet–triplet annihilation (TTA).

This delayed fluorescence provides a means of distinguishing between different types of radiation. Fluorescence emission shows an intense peak that decays exponentially with time due to the prompt fluorescence, as well as a non-exponentially decaying tail caused by the delayed fluorescence.[40–42] Gamma radiation activates species primarily through Compton scattering, whereas neutron radiation causes proton recoils. These interactions have different activation characteristics, which impacts the ratio of prompt to delayed fluorescence. The tail-to-total emission ratio, an example of which is shown in Figure 1.2 for *trans*–stilbene, can then be used to discriminate between types of ionizing radiation. This pulse-shape discrimination (PSD) can be used to identify a radioactive material based on its characteristic ratio of neutron to gamma particle emission.

Recent experiments have shown deuteration of single crystal *trans*–stilbene leads to an improvement in the PSD ability,[44] as shown in Figure 1.2. The effect of deuteration on the underlying processes that play an important role in PSD is thus of great interest. The excited state processes that impact PSD include intersystem crossing (ISC) from $S_1 \rightarrow T_1$, triplet migration through the material, and TTA. One method for modeling excited states is linear-response time-dependent density functional theory (TDDFT), an overview of which is presented in the next section.

1.2.1 Time-Dependent Density Functional Theory

Similar to the Hohenberg–Kohn theorems of ground state DFT, the Runge–Gross theorem forms the foundation of TDDFT.[45] This theorem proves that there is a direct relationship between a time-dependent external potential, $v_{ext}(r,t)$ and the electron density, $\rho(r,t)$.[46] Runge and Gross also showed that the variational principle holds true with respect to the quantum mechanical action, which is analogous to the energy.[45] Like with ground state DFT, the KS approach can be applied to provide a reasonable means of minimizing the action with respect to the density. The action functional is then given by

$$A[\rho] = A_{\mathrm{KS}}[\rho] - A_{xc}[\rho] - \frac{1}{2}\int_{\tau_0}^{\tau_1} \mathrm{d}\tau\, t'(\tau) \int \mathrm{d}r \int \mathrm{d}r'\, \frac{\rho(r,\tau)\rho(r',\tau)}{|r-r'|} \tag{1.6}$$

and the xc potential is

$$v_{xc}(r,t) = \left.\frac{\delta A_{xc}[\rho]}{\delta \rho(r,\tau)}\right|_{\rho=\rho(r,t)} \tag{1.7}$$

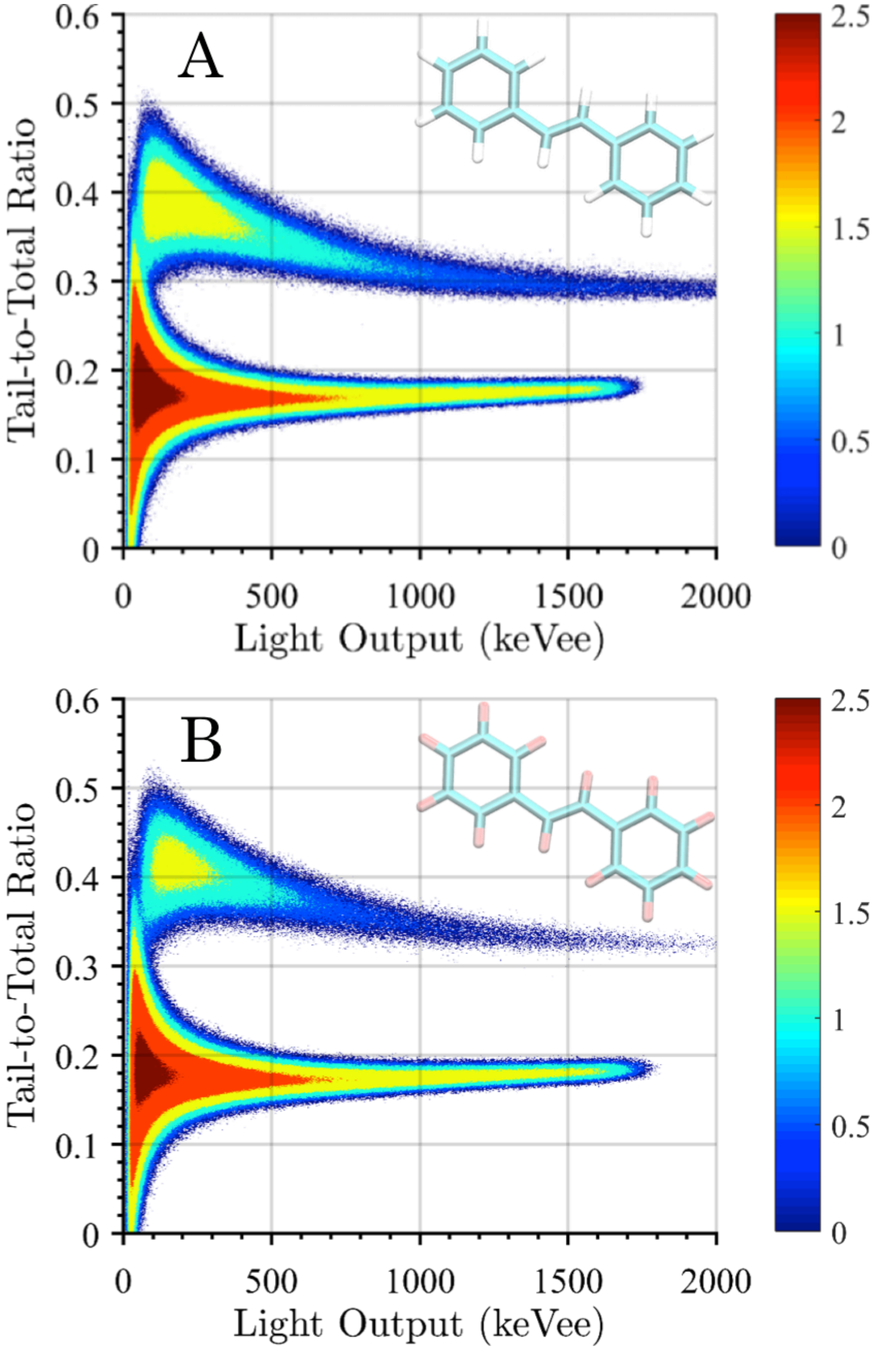

Figure 1.2: Pulse shape discrimination scatter plots for (A) *trans*–stilbene and (B) deuterated *trans*–stilbene–d_{12}, adapted from Reference 43.

While the Runge–Gross theorem tells us that the energies of the excited states are functionals of the electron density, as with ground state DFT it is not known how to exactly express such a functional.

One approach for obtaining excited state properties is to use linear response theory, which provides the time-dependent response of the density of the ground state system to a weak perturbing electric field. In the KS approach, the change in the ground state density in response to a small change in the external potential is given by[46]

$$\delta\rho_\sigma(r,\omega) = \sum_{\sigma'} \int \mathrm{d}r'\, \chi^{\mathrm{KS}}_{\sigma\sigma'}(r,r',\omega)\delta v^{\mathrm{KS}}_{\sigma'}(r',\omega) \tag{1.8}$$

$\chi^{\mathrm{KS}}_{\sigma\sigma'}(r,r',\omega)$ is the response function of the noninteracting KS electrons, and is given by

$$\chi^{\mathrm{KS}}_{\sigma\sigma'}(r,r',\omega) = \delta_{\sigma\sigma'} \sum_{jk}^{\infty} (f_{k\sigma} - f_{j\sigma}) \frac{\varphi_{j\sigma}(r)\varphi^*_{j\sigma}(r')\varphi_{k\sigma}(r')\varphi^*_{k\sigma}(r)}{\omega - (\epsilon_{j\sigma} - \epsilon_{k\sigma} + i\eta} \tag{1.9}$$

where $\varphi_{j\sigma}(r)$ and $\epsilon_{j\sigma}$ are the KS orbitals and corresponding energies, $f_{j\sigma}$ is the orbital occupation number, and η is a positive infinitesimal. The linear response can ultimately be represented as an eigenvalue problem by applying the single pole approximation, which assumes a single particle excitation between one occupied and one virtual orbital.[47] This leads to the so-called Casida equation:[48]

$$\begin{pmatrix} \hat{A} & \hat{B} \\ \hat{B}^* & \hat{A}^* \end{pmatrix} \begin{pmatrix} X \\ Y \end{pmatrix} = \omega \begin{pmatrix} 1 & 0 \\ 0 & -1 \end{pmatrix} \begin{pmatrix} X \\ Y \end{pmatrix} \tag{1.10}$$

where ω is the transition frequency, X and Y represent the occupied-to-virtual and virtual-to-occupied contributions to the perturbation density, and the matrix elements for A and B are

$$A_{ia\sigma,jb\sigma'} = \delta_{ij}\delta_{ab}\delta_{\sigma\sigma'}(\epsilon_{a\sigma} - \epsilon_{i\sigma}) + K_{ia\sigma,jb\sigma'} \tag{1.11}$$

$$B_{ia\sigma,jb\sigma'} = K_{ia\sigma,jb\sigma'} \tag{1.12}$$

In this way excitation energies and excited state electron densities can be calculated.

1.2.2 Dielectric Screening with Optimally Tuned Range-Separated Hybrid Functionals

Pure xc functionals do not qualitatively model the correct $1/r$ asymptotic behavior of the xc potential, as they fail to account for non-local effects.[49,50] Hybrid functionals add a fraction of exact HF exchange energy to the GGA exchange, and typically perform better than the original GGA functional for calculating a number of molecular properties.[51] Traditional hybrid functionals apply the HF exchange globally, but a more recent approach incorporates HF exchange only at large inter-electronic distances where it is more important. These so-called RSH functionals[52,53] separate the repulsive inter-electron coulomb potential into long-range (LR) and short-range (SR) components of the general form[54]

$$\frac{1}{r} = \frac{\alpha + \beta \mathrm{erf}(\gamma r)}{r} + \frac{1 - [\alpha + \beta \mathrm{erf}(\gamma r)]}{r} \tag{1.13}$$

where r is the inter-electronic distance and α, β, and γ are adjustable parameters. The first term accounts for the SR interaction, while the second term accounts for the LR interaction. The xc energy can then be calculated according to

$$\begin{aligned} E_{\mathrm{xc}}^{\mathrm{RSH}} &= \alpha E_{\mathrm{x,F}}^{\mathrm{SR},\gamma} + (1-\alpha)E_{\mathrm{x,GGA}}^{\mathrm{SR},\gamma} + (\alpha+\beta)E_{\mathrm{x,F}}^{\mathrm{LR},\gamma} \\ &\quad + (1-\alpha-\beta)E_{\mathrm{x,GGA}}^{\mathrm{LR},\gamma} + E_{\mathrm{c,GGA}} \end{aligned} \tag{1.14}$$

Here 'SR,γ' and 'LR,γ' indicate that the electronic repulsion, $1/r$, has been replaced by the corresponding SR and LR terms from Equation 1.13, respectively. In order for the xc potential to be asymptotically correct, the exchange energy should tend to 100% Fock exchange at large inter-electronic distances, which is accomplished by setting $\alpha + \beta = 1$.[55,56] This simplifies Equation 1.14 to

$$E_{\mathrm{xc}}^{\mathrm{RSH}} = \alpha E_{\mathrm{x,F}}^{\mathrm{SR},\gamma} + (1-\alpha) E_{\mathrm{x,GGA}}^{\mathrm{SR},\gamma} + E_{\mathrm{x,F}}^{\mathrm{LR},\gamma} + E_{\mathrm{c,GGA}} \tag{1.15}$$

With such RSH functionals, the γ parameter can be optimally tuned for a given system in the gas phase to obey Koopman's theorem[57–61] by minimizing the target function

$$J^2(\gamma) = (\epsilon_{\mathrm{H},n}^{\gamma} + I_n^{\gamma})^2 + (\epsilon_{\mathrm{H},a}^{\gamma} + I_a^{\gamma})^2 \tag{1.16}$$

where $\epsilon_{\mathrm{H}}^{\gamma}$ is the highest occupied molecular orbital (HOMO) energy, I^{γ} is the ionization potential, and 'n' and 'a' indicate the neutral and anionic species, respectively. It is also possible to tune α using this same procedure, although a value of around 0.20 is typically selected without tuning.[62] These optimally-tuned RSH (OT–RSH) functionals yield gaps between the HOMO and the lowest unoccupied molecular orbital (LUMO) that are in excellent agreement with fundamental gaps,[56] while also producing accurate CT excitations with linear-response TDDFT.[55,63,64] When solvating a system using a polarizable continuum model (PCM), however, the tuning procedure becomes more complicated.[55]

Several different approaches for tuning with PCM have been proposed,[62] such as the optimally-tuned screened RSH (OT–SRSH) method[65] that has recently been developed. In the OT–SRSH approach, γ is optimally tuned in the gas phase, and the electronic repulsion is screened by the dielectric constant, ϵ, of the environment,[62,65] which can be calculated using the Clausius–Mossotti equation.[35,66] This is accomplished by replacing $1/r$ in Equation 1.13 with $1/\epsilon r$, which leads to $\alpha + \beta = 1/\epsilon$ (rather than 1). In practice, α can be optimally tuned while selecting a value for β such that it conforms to the $\alpha + \beta = 1/\epsilon$ constraint, with the value for γ retained from the gas phase tuning.[62] Solid state TDDFT calculations using OT–SRSH have been shown to accurately predict gap renormalization, band structures, and photoemission and optical spectra.[65,67–69] in contrast to previous approaches, we perform the α tuning within the PCM environment (OT–SRSH–PCM). This approach was recently shown to compare well with ionization energies measured in thin film environments.[70] These features make this an attractive method for investigating the underlying processes involved in PSD in organic scintillators. In Chapter IV, we utilize this approach in conjunction with an equilibrium Fermi's golden rule (FGR) approach to investigate ISC and its impact on PSD.

CHAPTER II

Probing Charge Transfer in Organic Donor–Acceptor Systems by Mapping Vibrational Reporter Modes to the Local Electric Field

Contributions: Conception and design of study; acquisition, analysis, and interpretation of data; drafting and revision of final version to be published.

2.1 Introduction

Given the significant environmental impacts associated with using traditional fossil fuels to meet the increasing global energy demand, solar energy is expected to play an increasingly more important role in energy production. Solar energy production in the United States has increased approximately tenfold over the past decade, from less than 0.1% to nearly 1% of the total energy produced.[71] While current solar cells predominantly use technologies based on inorganic materials, such as silicon or $CuInGaSe_2$ (CIGS), organic photovoltaic materials have been an area of intense research, particularly over the last decade.[1–4,72] Organic semiconductor materials offer significant advantages over typical inorganic solar cells, such as synthetic variability, reduced cost of materials and processing, and flexible form factors.[73–77] In recently developed OPV materials power conversion efficiencies have surpassed 13%,[10,78] with

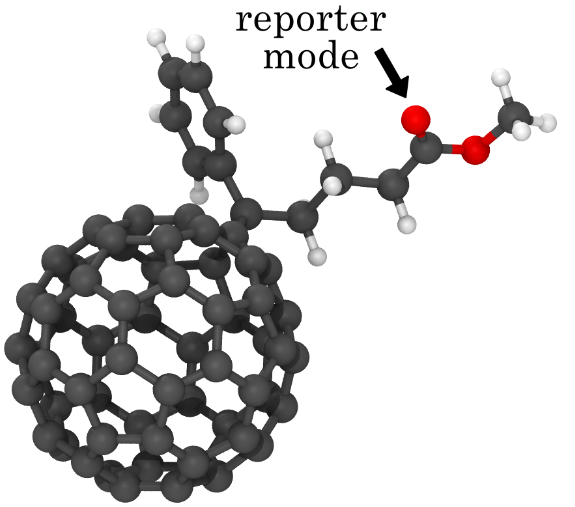

Figure 2.1: A PCBM molecule with the carbonyl reporter mode indicated.

production-quality cells currently yielding around 7-8%.[78] As there is still significant room for improvement, a better understanding of the charge transfer process in these materials is of significant interest.[79]

A typical OPV thin-film consists of a molecular electron acceptor, such as phenyl–C_{61}–butyric acid methyl ester (PCBM), that is blended with a polymeric electron donor and forms nanoclusters within the film. Ultrafast 2DIR techniques have been utilized to monitor the photoinduced CT process in such OPVs via a vibrational probe.[11–22] The carbonyl in the methyl ester group of PCBM (see Figure 2.1) is sensitive to the surrounding environment, and thus there is a frequency shift observed at the interface between the acceptor and donor materials. This frequency gradient between the interface and the bulk makes the CO stretch a useful reporter mode for 2DIR, with pump–probe experiments showing a blue frequency shift of about 5–10 cm^{-1}, enabling monitoring of the charge separation process. The frequency shift is due, at least in part, to VSEs[14,23,24] induced by changes in the local electric field.

Vibrational Stark spectroscopy has been used extensively with CO, NO, and CN modes to probe the active sites of proteins, which can exhibit significant electric field variations throughout.[23,25–27] In these experiments, the primary interaction of the electric field is with the change in dipole moment of the vibration, such that the relationship between the frequency and the field is of the form[27]

$$hc\Delta\bar{\nu}_{\mathrm{obs}} = -\Delta\boldsymbol{\mu} \cdot \Delta\boldsymbol{F}_{\mathrm{protein}} \tag{2.1}$$

where $\Delta\bar{\nu}_{\mathrm{obs}}$ is the observed frequency shift, $\Delta\boldsymbol{\mu}$ is the change in the dipole moment of the vibration, and $\Delta\boldsymbol{F}_{\mathrm{protein}}$ is the change in the electric field of the protein. $\Delta\boldsymbol{\mu}$ is referred to as the Stark tuning rate (STR) when expressed in units of $\mathrm{cm}^{-1}/(\mathrm{MV/cm})$, and for a localized mode is oriented in the direction of the bond. The STR is composed of an anharmonic contribution, as well as a contribution from geometric distortions induced by the electric field.[80]

In the case of charge transfer, VSEs have successfully been utilized to study the intramolecular CT process in a molecular dye by using an IR-active solvation shell as a vibrational probe.[81] The change in electric field induced by the CT reaction leads to VSEs that shift the frequency of the probe by a few wavenumbers, which can be observed spectroscopically. In this chapter, we investigate VSEs in a molecular donor–acceptor system using a carbonyl reporter mode located on the electron acceptor. Calculations were performed using DFT, which has been shown to yield STRs that agree quantitatively with experimental results.[80]

The remainder of this chapter is organized as follows. The computational methods used to calculate vibrational frequencies and electric fields are detailed in Section 2.2. The results of these calculations are reported in Section 2.3. The conclusions are discussed in Section 2.4.

2.2 Computational Methods

Optimized geometries and energies were calculated using DFT with the ωB97X–D RSH functional[82,83] in the 6-311G(d,p) basis set,[84] with CDFT used to model the

CT states. All electronic structure calculations were performed using the Q-Chem 4.4 software package.[85] Vibrational frequencies for the carbonyl reporter modes were determined by varying the bond length about the center of mass over a range of $\sim$0.8 Å, and calculating the potential energies at each point. The potential energies were then fit to a Morse potential[86] (Equation 2.2) using the Mathematica 10.2 software package,[87] an example of which is illustrated in Figure 2.2. The fundamental frequency, ω_0, was then calculated according to Equation 2.3[88] using the well depth, D_e, and curvature, α, terms obtained from the Morse potential, where μ is the reduced mass of the carbonyl (6.86 amu). The anharmonic constant, x_e, was calculated via Equation 2.4.[88]

$$V(r) = D_e(1 - e^{-a(r-r_e)})^2 \qquad \text{Morse Potential} \tag{2.2}$$

$$\omega_0 = \frac{\alpha}{2\pi c}\sqrt{\frac{2D_e}{\mu}} \qquad \text{Fundamental Frequency} \tag{2.3}$$

$$x_e = \frac{h\omega_0 c}{4D_e} \qquad \text{Anharmonic Constant} \tag{2.4}$$

External electric fields ranging from -25 to 25 MV/cm were applied along the bond of the carbonyl probe for each system, and the frequencies were calculated via the method described above. The change in dipole moment is oriented in the direction of the mode, so STRs can be obtained from frequency–field correlation plots via linear fitting.[89] CDFT was used to optimize the CT state geometries of the donor–acceptor systems, as well as to calculate the single point energies used for the frequency calculations. Electric fields were assumed to be homogeneous and calculated at the center of mass of the carbonyl using Mulliken partial atomic charges[90] according to Coulomb's law

$$\boldsymbol{F} = \frac{1}{4\pi\epsilon_0}\sum_i \frac{q_i}{|\boldsymbol{r}_i|^2}\hat{\boldsymbol{r}}_i \tag{2.5}$$

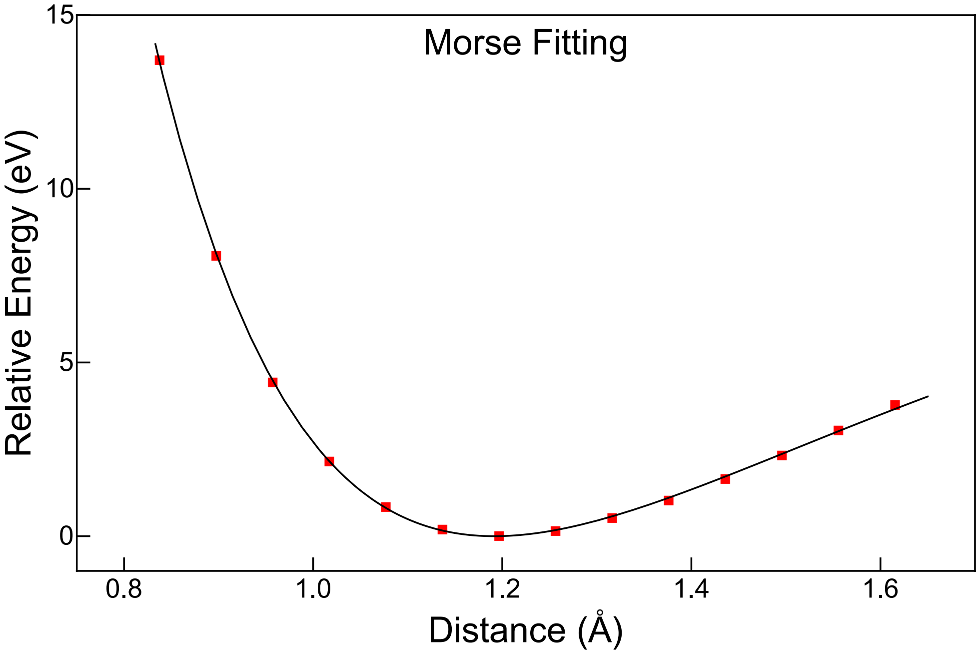

Figure 2.2: Example potential energy curve obtained by fitting a Morse potential to the single point energies calculated at different C=O bond lengths using DFT with the ωB97X-D functional.

where ϵ_0 is the permittivity constant, q_i is the Mulliken partial charge of atom i, $\boldsymbol{r}_i$ is the vector from the carbonyl to atom i, and $\hat{\boldsymbol{r}}_i$ is the corresponding unit vector. The resulting electric field was then projected onto the CO bond to determine the field strength observed in the direction of the dipole. The charge of the carbonyl was not included in calculation of the electric field.

2.3 Results and Discussion

In this study, we calculated STRs for carbonyl modes in the molecular donor–acceptor systems shown in Figure 2.3 by applying an external electric field along the bond axis. Formaldehyde (CH_2O) was initially examined as a simple test case for this approach, and Figure 2.4 clearly shows a linear relationship between the frequency and field strength with a tuning rate of 0.376 $\text{cm}^{-1}/(\text{MV/cm})$. In order to investigate VSEs in fullerene-based CT systems, we selected C_{60} with a heterocyclic bridged *N*,*N*–

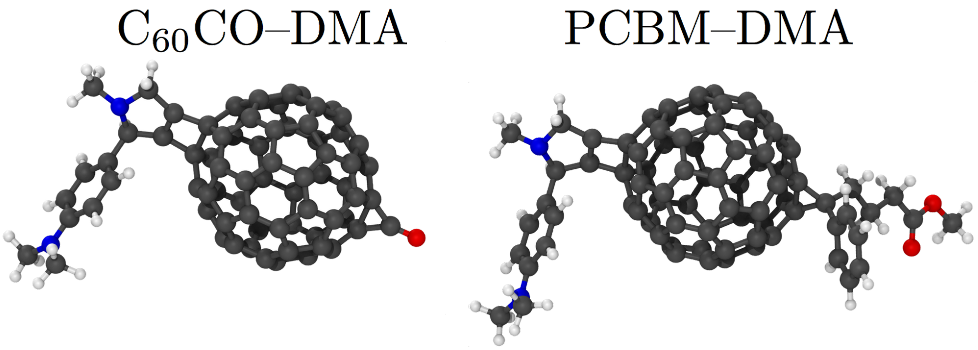

Figure 2.3: Molecular structures of C_{60}CO–DMA and PCBM–DMA.

dimethylaniline (DMA)[91] as an initial benchmark, due to the reduced computational cost associated with its relatively small size. We affixed a carbonyl to the C_{60} and calculated an STR of 1.026 $\text{cm}^{-1}/(\text{MV/cm})$ from an applied external field, which agrees quite well with typical ketone tuning rates of about 0.7–1.0 $\text{cm}^{-1}/(\text{MV/cm})$.[92] Given this encouraging result we proceeded to examine a PCBM–DMA system, as PCBM is one of the most commonly used electron acceptors in OPV materials. The STR was found to be 0.656 $\text{cm}^{-1}/(\text{MV/cm})$ in this case, which also agrees fairly well with reported STR ranges.[92]

Having shown that the carbonyls in these two donor–acceptor systems exhibit large STRs, the next question to address is whether CT induces a significant change to the electric field. For each system, we examined different configurations in which the position of the DMA relative to the reporter mode was varied (Figures 2.5 and 2.6). This was done to change the electric field strength observed at the carbonyl, as well as alter the orientation of the dipole relative to the CT reaction coordinate. Four different configurations were examined for C_{60}CO–DMA and seven different configurations for PCBM–DMA. Frequencies and electric fields were calculated for each of the configurations in the ground state and CT state, with the frequency–field correlation plots shown in Figures 2.5 and 2.6. The primary contributions to the STR, anharmonicity and field-induced geometric distortions,[80] are accounted for via the Morse potential and the geometry re-optimization in the CT state, respectively.

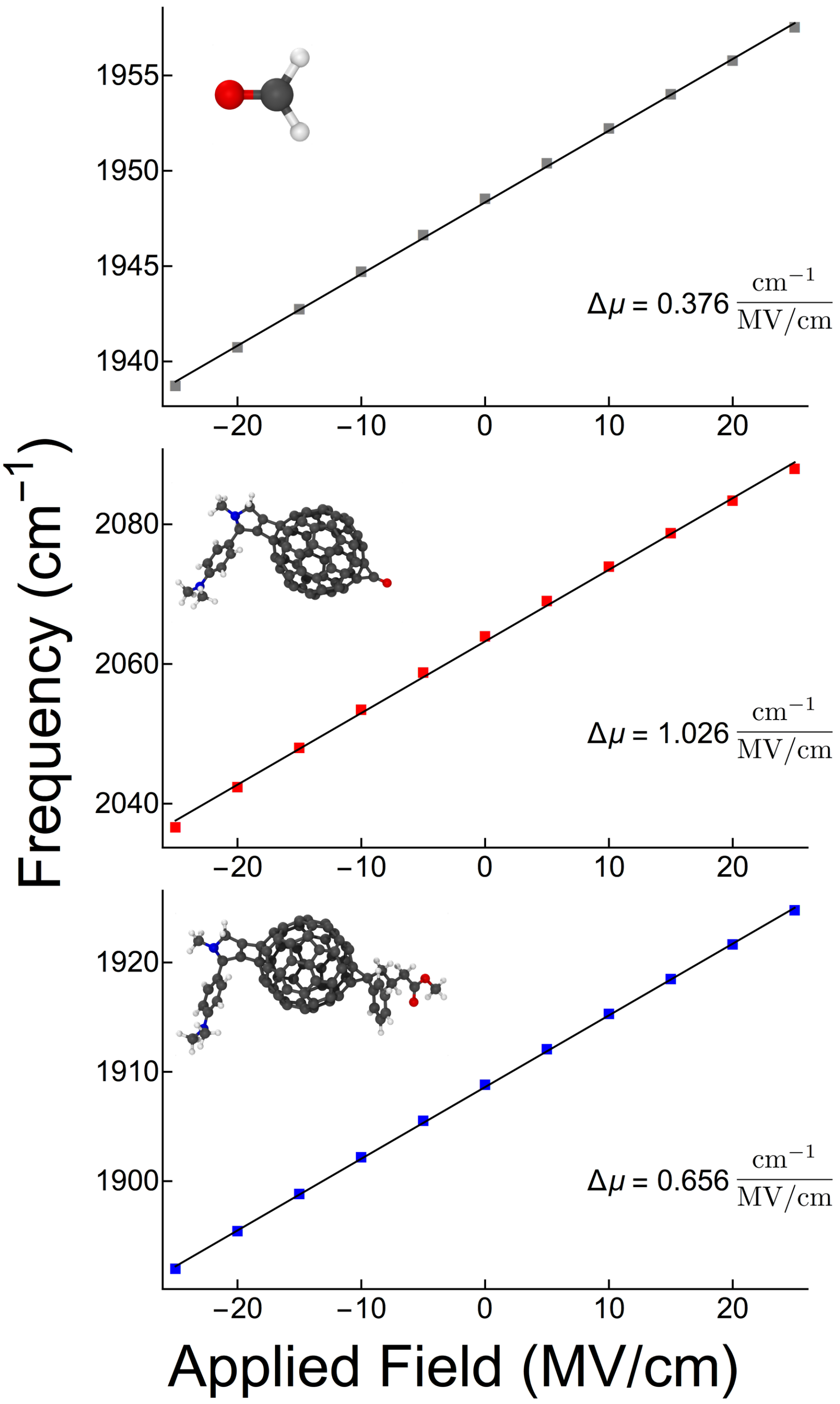

Figure 2.4: Effect of an applied electric field on the vibrational frequency of the carbonyl reporter mode for each of the model systems. Formaldehyde is shown in gray, C_{60}CO-DMA is shown in red, and PCBM-DMA is shown in blue, with Stark tuning rates ($\Delta\mu$) displayed for each in $\mathrm{cm}^{-1}/(\mathrm{MV/cm})$.

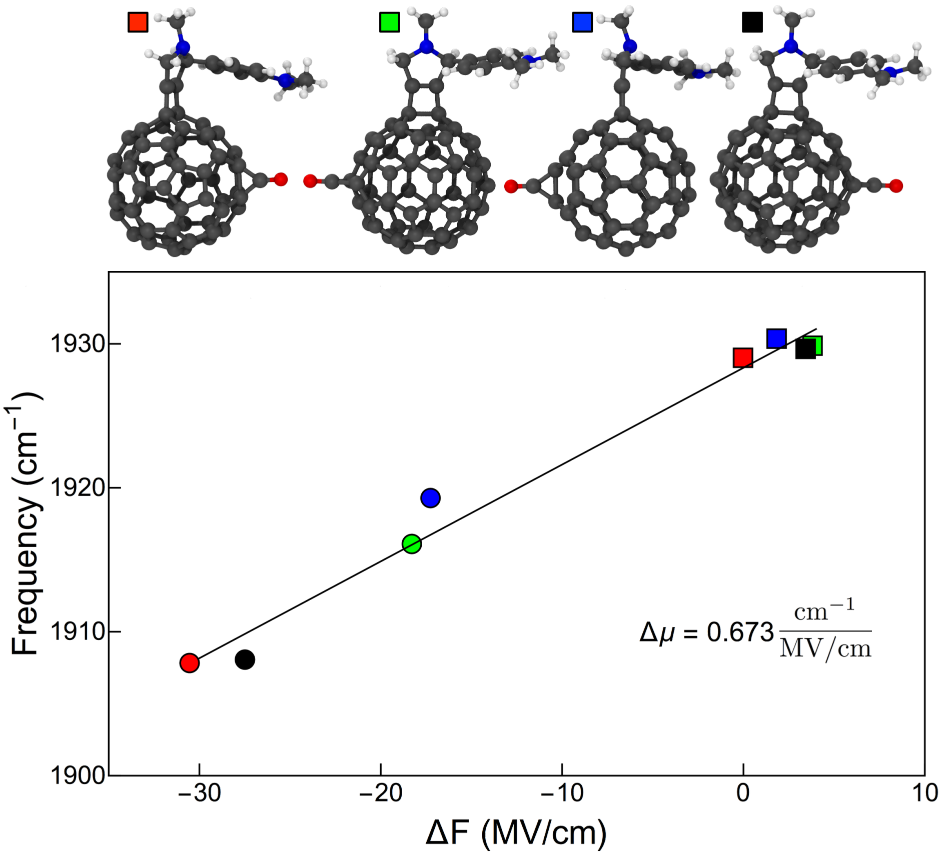

Figure 2.5: Frequency–field correlation plot for C_{60}–DMA, with ground state configurations (squares) and their corresponding CT states (circles) indicated by matching colors. For each configuration, the position of DMA was varied relative to that of the carbonyl reporter. The Stark tuning rate ($\Delta\mu$) is shown in cm^{-1}/(MV/cm).

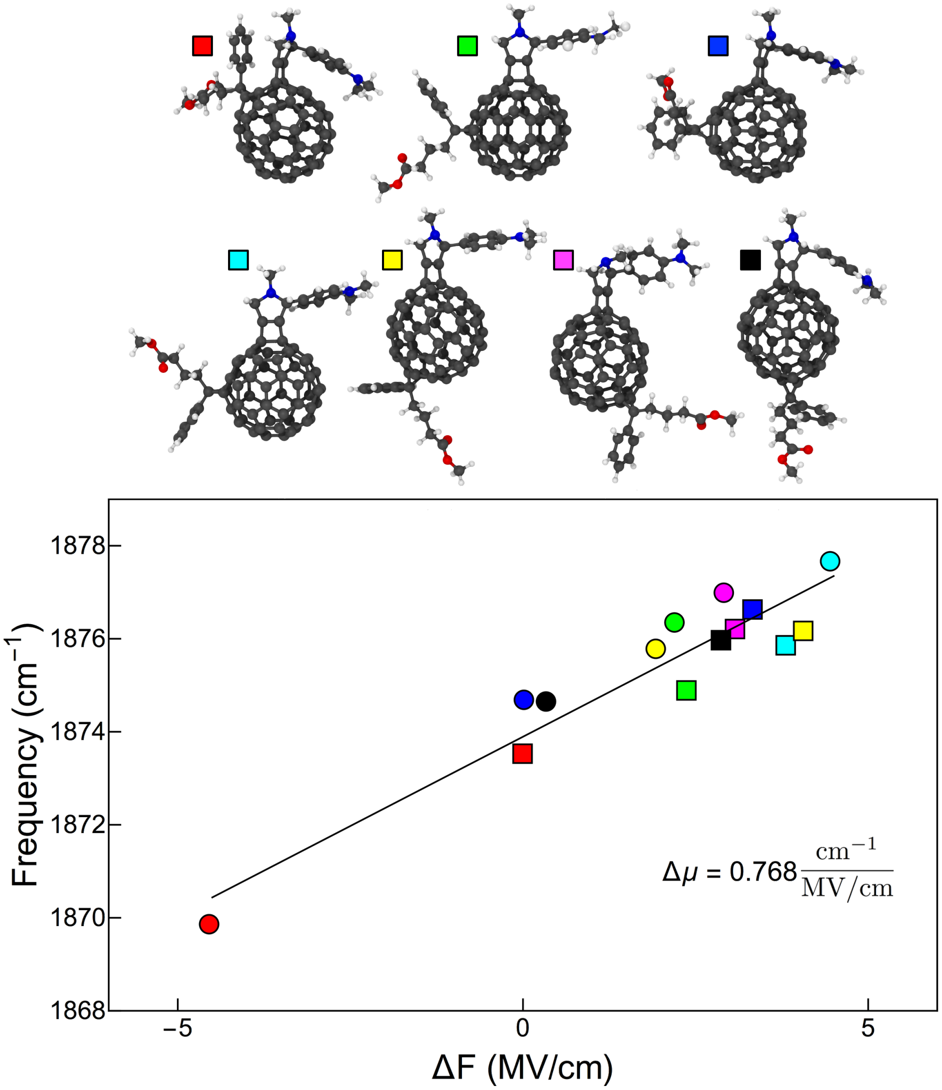

Figure 2.6: Frequency–field correlation plot for PCBM–DMA, with ground state configurations (squares) and their corresponding CT states (circles) indicated by matching colors. For each configuration, the position of DMA was varied relative to that of the cabronyl reporter. The Stark tuning rate ($\Delta\mu$) is shown in cm^{-1}/(MV/cm).

In C_{60}CO–DMA (Figure 2.5), the position of the carbonyl does not have a significant impact on the field strength in the ground state, with a range of about 4 MV/cm, but has a more notable effect in the CT state (>10 MV/cm). In all configurations there is a significant change in the electric field of about 20–30 MV/cm between the ground state and the CT state, with a more pronounced effect in the two configurations where the C=O is positioned closer to the DMA moiety. The large differences in field strength can be explained by the close proximity of the carbonyl to the fullerene, over which the negative charge is delocalized in the CT state. There is a strong linear relationship between the frequency and the field strength, with a tuning rate of 0.673 cm^{-1}/(MV/cm). While this is smaller than the STR of 1.026 cm^{-1}/(MV/cm) calculated by applying an external field, it remains close to the range expected for a carbonyl. This discrepancy suggests that the frequency shift is also affected by through-bond quantum-chemical factors that cannot be described in purely electrostatic terms.

In PCBM–DMA (Figure 2.6), the position of DMA relative to the methyl ester similarly does not have a significant effect on the field strength in the ground state, again with a range of about 4 MV/cm, while the impact in the CT state is not as significant as with C_{60}CO–DMA. The effect of CT on the field strength is less pronounced than in C_{60}CO–DMA, ranging from a negligible impact to nearly 5 MV/cm. CT has a reduced impact in this case due to the greater distance of the C=O from the fullerene. Given the tuning rate of 0.768 cm^{-1}/(MV/cm), this translates to relatively minor frequency shifts of less than 4 cm^{-1} due to charge transfer, which are smaller than the blue frequency shifts observed experimentally in OPV thin films of about 5–10 cm^{-1}.[16] It should also be noted that these calculated frequencies undergo both red and blue shifts, depending on the relative position of the DMA. This likely indicates that the small CO dipole moment changes direction under the influence of the field.[93]

2.4 Conclusions

For the investigated donor–acceptor systems, vibrational frequencies of the reporter modes show a linear correlation to changes in the electric field strength along the mode, with the calculated STRs of 0.673 and 0.768 cm^{-1}/(MV/cm) showing good agreement with the typical range for carbonyls of about 0.7–1.0 cm^{-1}/(MV/cm).[92] For the case of PCBM–DMA, CT led to relatively small changes in the electric field at the carbonyl, and thus fairly small frequency shifts as well (less than 4 cm^{-1}). This relatively small difference compared to C_{60}CO–DMA is a consequence of the greater distance of the carbonyl from the fullerene, on which the negative charge is delocalized in the CT state. While the frequencies experience shifts due to CT, the direction of the shift depends on the configuration. It is therefore unclear whether CT might contribute to the experimentally observed frequency shifts,[16] and would require further investigation.

It would be beneficial to explore similar systems, for example by incorporating different electron donors, in order to examine the impact on the VSEs and perhaps further justify these results. Additionally, the surrounding environment would be expected to have a significant effect on the electric field, and thus the frequency, of the probe. Given the relatively large size of these systems, however, explicit solvation is not feasible for quantum mechanical calculations. One approach to mitigate this problem would be to determine the electric field using molecular mechanics calculations that incorporate the surrounding molecular environment, while still relying on DFT to calculate the vibrational frequencies. In fact, we utilize such an approach in the next chapter for the investigation of a molecular triad.

CHAPTER III

A Computational Study of Charge Transfer Dynamics in the Carotenoid–Porphyrin–C_{60} Molecular Triad Solvated in Explicit Tetrahydrofuran and its Spectroscopic Signature

Contributions: Conception and design of study; acquisition, analysis, and interpretation of electronic structure, vibrational frequency, and electric field data; drafting and revision of final version to be published.

Reproduced with permission from Sun, X.; Zhang, P.; Lai, Y.; Williams, K. L.; Cheung, M.; Dunietz, B. D.; Geva, E. *J. Phys. Chem. C* **2018**, *122*, 11288–11299.

3.1 Introduction

The interplay between CT dynamics and molecular structure is key for processes that are fundamental to life, such as cellular respiration[94] and photosynthesis,[95] as well as for processes that lie at the heart of important technologies, such as energy storage, photovoltaics and thermoelectrics.[96–101] CT rates are often calculated by and rationalized within the framework of Marcus theory.[102–105] The popularity of Marcus theory can be attributed to the fact that the Marcus CT rate constant can be expressed in terms of three parameters – the electronic coupling coefficient, reorganization energy and reaction free energy. As such it offers a straightforward pathway for fitting and interpreting experimentally measured CT rate constants. However, the restrictive nature of the assumptions underlying Marcus theory also makes it highly desirable to develop more comprehensive methods for calculating CT rates.[106] In particular, it is highly desirable to develop strategies for calculating CT rates for a system whose Hamiltonian is given in terms of anharmonic force fields in a direct manner and without resorting to mapping it onto an effective harmonic model Hamiltonian.[107–110]

Such a general and direct strategy for calculating CT rate constants in complex molecular systems described by general anharmonic force fields has recently been proposed.[106] Our approach starts out by applying the linearized semiclassical (LSC) approximation to the equilibrium FGR expression for the CT rate constant.[111] The classical-like nature of the LSC-based FGR expression implies that it can be applied to complex molecular systems governed by anharmonic force fields of one's choice. At the same time, the LSC-based FGR expression has been shown to reproduce the quantum-mechanically exact rate constant when the donor and acceptor PESs are parabolic and identical except for shifts in equilibrium geometry and equilibrium energy. It was also shown in Ref. 106 that obtaining a Marcus-like expression from the LSC-based FGR expression requires three major approximations:[106]

1. assuming that the initial sampling of nuclear degrees of freedom (DOF) is based on the *classical* Boltzmann distribution, instead of the corresponding Wigner distribution called for by the LSC-based FGR expression
2. assuming that the lifetime of the correlation function underlying FGR is shorter than the timescale of nuclear DOF motion
3. assuming that the cumulant expansion of the correlation function underlying FGR can be truncated at second order.

The Marcus-like approximation that results from those three approximations is given in terms of the first and second moments of the donor–acceptor energy gap, which can be calculated in a straightforward manner from a classical equilibrium molecular dynamics (MD) simulation on the donor PES. Those first and second moments of the donor–acceptor energy gap can be related to the reaction free energy and reorganization energy of Marcus theory (see Ref. 106, as well as Sec. 3.2).

Ref. 106 provides a comprehensive analysis of the aforementioned LSC-based strategy, starting at the FGR level and going through the progression of approximations that lead to the Marcus-like level. This analysis was done within the framework of a benchmark model, where the donor and acceptor PESs correspond to identical multidimensional parabolas that differ only with respect to their equilibrium geometries and energies, and for which the *quantum-mechanically exact* FGR rate constant is known. It should be emphasized that while such a model provided a useful platform for developing and testing the methodology, the actual LSC-based methodology is not limited to systems with harmonic PESs. In fact, the main advantage of the LSC-based methodology is its applicability to molecular models, which would typically be governed by anharmonic force fields of one's choice.

In this chapter, this is demonstrated by applying the aforementioned strategy to a molecular model of the carotenoid–porphyrin–C_{60} triad in explicit tetrahydrofuran (THF) solvent.[112] It should be noted that CT rate constants for this system were recently calculated via another method at the Marcus level of theory.[112] It was also found in Ref. 112 that CT dynamics in this system is strongly dependent on the conformation of the triad and is much faster in the linear conformation than in the more thermodynamically favorable bent conformation. In this chapter, we go beyond that by testing the validity of the Marcus-like level of theory and showing that CT in this system is dominated by the DOF of the solvent (THF), rather than those of the solute (triad).

CT dynamics in the solvated triad starts out with photoexcitation of the triad from the ground electronic state to the excited bright $\pi\pi^*$ state, which is followed by radiationless transitions into electronically excited CT states. The fact that the latter are dark makes it difficult to follow them via UV–vis/UV–vis pump–probe spectroscopy. At the same time, the fact that the frequencies of local vibrational spectator modes can be very sensitive to charge redistribution in their vicinity turns them into potential probes of the CT process. Thus, monitoring the time-resolved IR spectra of those modes following photoexcitation can provide a uniquely direct real-time probe of the dynamics of such photoinduced CT processes. Recent applications of such time-resolved UV–vis/IR pump–probe spectroscopy include the investigation of photoinduced CT,[11–22,113–115] the dynamics of H-bonds in the condensed phase,[116] the structural rearrangement and cooling following *cis–trans* photoisomerization,[117,118] and the conformational dynamics of photoswitchable peptides.[119] In the context of the system under consideration here, we envision following an electronic photoexcitation of the triad with a pulse in the UV–vis range, by one or more time-delayed IR probe pulses tuned to excite the triad's amide I stretch, which would allow one to monitor, in real time, changes in electronic and molecular structure triggered by photoexcitation.[113,120] Thus, another goal of this chapter is to investigate the prospect of using the triad's single amide I stretch as a real-time IR spectroscopic probe of the photoinduced CT dynamics. To this end, we calculated the amide I stretch frequency distributions at different electronic and conformational states. Our results show that the amide I stretch frequency is indeed very sensitive to the conformational and electronic states of the triad. We hope that these results will motivate the use of UV–vis/IR pump–probe spectroscopy to study CT and conformational dynamics in such systems.

The remainder of this chapter is organized as follows. The LSC-based methodology for calculating CT rate constants is described in Sec. 3.2. The molecular model and computational techniques are described in Sec. 3.3. Results are reported in Sec. 3.4. The main conclusions and outlook are provided in Sec. 3.5.

3.2 Theory

Consider the fully quantum-mechanical Hamiltonian operator of a two-state donor–acceptor system (in what follows, "$\hat{O}$" implies that the quantity corresponds to a quantum-mechanical operator and boldfaced font means that the quantity is a vector):

$$\hat{H} = \hat{H}_{\mathrm{D}}|\mathrm{D}\rangle\langle\mathrm{D}| + \hat{H}_{\mathrm{A}}|\mathrm{A}\rangle\langle\mathrm{A}| + \Gamma_{\mathrm{DA}}\left[|\mathrm{D}\rangle\langle\mathrm{A}| + |\mathrm{A}\rangle\langle\mathrm{D}|\right] \tag{3.1}$$

Here, $|\mathrm{A}\rangle$ and $|\mathrm{D}\rangle$ represent the *diabatic* acceptor and donor electronic states, respectively, $\hat{H}_{\mathrm{A}} = \hat{\mathbf{P}}^2/2 + V_{\mathrm{A}}(\hat{\mathbf{R}})$ and $\hat{H}_{\mathrm{D}} = \hat{\mathbf{P}}^2/2 + V_{\mathrm{D}}(\hat{\mathbf{R}})$ are the corresponding nuclear Hamiltonians, $V_{\mathrm{A}}(\hat{\mathbf{R}})$ and $V_{\mathrm{D}}(\hat{\mathbf{R}})$ are the PESs, $\hat{\mathbf{R}} = \left(\hat{\mathbf{R}}_1, ..., \hat{\mathbf{R}}_N\right)$ and $\hat{\mathbf{P}} = \left(\hat{\mathbf{P}}_1, ..., \hat{\mathbf{P}}_N\right)$ are the mass-weighted coordinates and momenta of all nuclear DOFs (triad + solvent for the system under consideration in this paper), and Γ_{DA} is the electronic coupling coefficient. Importantly, $V_{\mathrm{A}}(\mathbf{R})$ and $V_{\mathrm{D}}(\mathbf{R})$ are assumed to be given in terms of anharmonic force fields (see Sec. 3.3).

Assuming that the system starts out in the donor state, with the initial state of the nuclear DOFs at thermal equilibrium on the donor PES, the initial state of the overall system is given by the density operator ($\beta = 1/k_BT$ and Tr_n stands for tracing over the nuclear DOF):

$$\begin{aligned} \hat{\rho}(0) &= \hat{\rho}_{\mathrm{D}}^{\mathrm{eq}}|\mathrm{D}\rangle\langle\mathrm{D}|; \\ \hat{\rho}_{\mathrm{D}}^{\mathrm{eq}} &= \exp\left[-\beta\hat{H}_{\mathrm{D}}\right]/\mathrm{Tr}_n\left(\exp\left[-\beta\hat{H}_{\mathrm{D}}\right]\right) \end{aligned} \tag{3.2}$$

Further assuming that the electronic coupling term in Eq. 3.1, $\Gamma_{\mathrm{DA}}\left[|\mathrm{D}\rangle\langle\mathrm{A}| + |\mathrm{A}\rangle\langle\mathrm{D}|\right]$, can be treated as a small perturbation relative to the zero Hamiltonian, defined by $\hat{H}_0 = |\mathrm{D}\rangle\hat{H}_{\mathrm{D}}\langle\mathrm{D}| + |\mathrm{A}\rangle\hat{H}_{\mathrm{A}}\langle\mathrm{A}|$, the fully quantum-mechanical FGR donor-to-acceptor

CT rate constant can be shown to be given by[111,121–123]

$$k_{\mathrm{A}\leftarrow\mathrm{D}} = \frac{1}{\hbar^2}\Gamma_{\mathrm{DA}}^2 \int\limits_{-\infty}^{\infty} \mathrm{d}\tau \mathrm{Tr}_n \left[\hat{\rho}_{\mathrm{D}}^{\mathrm{eq}} e^{-i\hat{H}_{\mathrm{A}}\tau/\hbar} e^{i\hat{H}_{\mathrm{D}}\tau/\hbar}\right] \tag{3.3}$$

A fully quantum mechanical expression for $k_{\mathrm{A}\leftarrow\mathrm{D}}$ can only be derived in closed form when the diabatic PESs are assumed to be harmonic.[107,123–129] The LSC approximation for $k_{\mathrm{A}\leftarrow\mathrm{D}}$ is obtained by rewriting the integrand in Eq. 3.3 in terms of a, still *quantum-mechanically exact*, real-time Feynman path integral[130–132] and expanding the forward–backward action to first order with respect to the difference between the forward and backward trajectories.[111,133,134] The resulting LSC approximation for $k_{\mathrm{A}\leftarrow\mathrm{D}}$ is given by

$$\begin{aligned} k_{\mathrm{A}\leftarrow\mathrm{D}}^{\mathrm{W-AV}} &= \frac{1}{\hbar^2}\Gamma_{\mathrm{DA}}^2 \int\limits_{-\infty}^{\infty} \mathrm{d}\tau \int \mathrm{d}\mathbf{R_0} \int \mathrm{d}\mathbf{P_0} [\hat{\rho}_{\mathrm{D}}^{\mathrm{eq}}]_{\mathrm{W}}(\mathbf{R}_0, \mathbf{P}_0) \exp\left(i \int\limits_0^{\tau} \mathrm{d}\tau' U(\mathbf{R}_{\tau'})/\hbar\right) \\ &\equiv \frac{1}{\hbar^2}\Gamma_{\mathrm{DA}}^2 \int\limits_{-\infty}^{\infty} \mathrm{d}\tau \left\langle \exp\left(i \int\limits_0^{\tau} \mathrm{d}\tau' U(\mathbf{R}_{\tau'})/\hbar\right)\right\rangle_{\mathrm{D}}^{\mathrm{W,eq}} \end{aligned} \tag{3.4}$$

Here, $U(\mathbf{R}) = V_{\mathrm{D}}(\mathbf{R}) - V_{\mathrm{A}}(\mathbf{R})$ is the donor–acceptor energy gap, $[\hat{\rho}_{\mathrm{D}}^{\mathrm{eq}}]_{\mathrm{W}}(\mathbf{R}_0, \mathbf{P}_0)$ is the Wigner transform[135] of $\hat{\rho}_{\mathrm{D}}^{\mathrm{eq}}$ and $\mathbf{R}_\tau$ is obtained by classical dynamics, starting with $\{\mathbf{R}_0, \mathbf{P}_0\}$ as the initial conditions and propagating on the average PES, $V_{\mathrm{av}}(\mathbf{R}) = [V_{\mathrm{D}}(\mathbf{R}) + V_{\mathrm{A}}(\mathbf{R})]/2$. We label this approximation "W-AV" [Wigner (W) initial sampling with dynamics on average (AV) PES]. We also note that despite its classical-like nature, the W-AV approximation yields the *exact* quantum mechanical equilibrium FGR CT rate constant when the donor and acceptor PESs are parabolic and identical except for a shift in equilibrium energy and equilibrium geometry.[106]

The classical Marcus expression[102–104] can be obtained from Eq. 3.4 by making a number of approximations. First, the Wignerized phase space density, $[\hat{\rho}_{\mathrm{D}}^{\mathrm{eq}}]_{\mathrm{W}}(\mathbf{R}_0, \mathbf{P}_0)$, needs to be replaced by the corresponding classical phase space density, $\rho^{\text{eq}}_{\text{D,Cl}}\left(\mathbf{R}_0, \mathbf{P}_0\right)$

$$\begin{aligned}
k^{\text{C}-\text{AV}}_{\text{A}\leftarrow\text{D}} &= \frac{1}{\hbar^2}\Gamma^2_{\text{DA}} \int\limits_{-\infty}^{\infty} \mathrm{d}\tau \int \mathrm{d}\mathbf{R_0} \int \mathrm{d}\mathbf{P_0} \hat{\rho}^{\text{eq}}_{\text{D,Cl}}\left(\mathbf{R}_0, \mathbf{P}_0\right) \exp\left(i \int\limits_{0}^{\tau} \mathrm{d}\tau' U(\mathbf{R}_{\tau'})/\hbar \right) \\
&\equiv \frac{1}{\hbar^2}\Gamma^2_{\text{DA}} \int\limits_{-\infty}^{\infty} \mathrm{d}\tau \left\langle \exp\left(i \int\limits_{0}^{\tau} \mathrm{d}\tau' U(\mathbf{R}_{\tau'})/\hbar \right) \right\rangle^{\text{Cl,eq}}_{\text{D}}
\end{aligned} \tag{3.5}$$

We label this approximation “C–AV” [classical (C) sampling with dynamics on average (AV) PES].

Second, one needs to assume that $\langle \exp\left(i \int_0^\tau \mathrm{d}\tau' U(\mathbf{R}_{\tau'})/\hbar \right) \rangle^{\text{eq}}_{\text{D,Cl}}$ decays faster than the nuclear dynamics timescale on which $U(\mathbf{R}_{\tau'})$ changes, which leads to the following approximation

$$\begin{aligned}
k^{\text{C}-0}_{\text{A}\leftarrow\text{D}} &= \frac{1}{\hbar^2}\Gamma^2_{\text{DA}} \int\limits_{-\infty}^{\infty} \mathrm{d}\tau \int \mathrm{d}\mathbf{R_0} \int \mathrm{d}\mathbf{P_0} [\hat{\rho}^{\text{eq}}_{\text{D}}]_{\text{Cl}}\left(\mathbf{R}_0, \mathbf{P}_0\right) \exp\left(iU(\mathbf{R}_0)\tau/\hbar \right) \\
&\equiv \frac{1}{\hbar^2}\Gamma^2_{\text{DA}} \int\limits_{-\infty}^{\infty} \mathrm{d}\tau \left\langle \exp\left(iU(\mathbf{R}_0)\tau/\hbar \right) \right\rangle^{\text{eq}}_{\text{D,Cl}} \\
&= \frac{2\pi}{\hbar}\Gamma^2_{\text{DA}} \langle \delta(U) \rangle^{\text{eq}}_{\text{D,Cl}}
\end{aligned} \tag{3.6}$$

We label this approximation “C–0” [classical (C) sampling and independent of which PES the dynamics takes place on (0)].

It should be noted that $k^{\text{C}-0}_{\text{A}\leftarrow\text{D}}$ is proportional to the probability density of U, $\rho(U)$, at $U = 0$, $\rho(U = 0) = \langle \delta(U) \rangle^{\text{eq}}_{\text{D,Cl}}$ (see last equality in Eq. 3.6). Because the absolute value of the average of U, $\left| \langle U \rangle^{\text{eq}}_{\text{D,Cl}} \right|$, is typically significantly larger than zero, calculating $k^{\text{C}-0}_{\text{A}\leftarrow\text{D}}$ requires being able to obtain an accurate estimate of the tail of the probability density. This becomes computationally more costly with increasing $\left| \langle U \rangle^{\text{eq}}_{\text{D,Cl}}/\hbar \right|$ because more sampling will be required in order to obtain a converged result.

It should also be noted that $U(\mathbf{R})$ can be written as $U(\mathbf{R}) = \langle U\rangle^{\text{eq}}_{\text{D,Cl}} + \delta U(\mathbf{R})$, where $\delta U(\mathbf{R}) = U(\mathbf{R}) - \langle U\rangle^{\text{eq}}_{\text{D,Cl}}$ is the fluctuation of $U(\mathbf{R})$ relative to its equilibrium averaged value ($\langle U\rangle^{\text{eq}}_{\text{D,Cl}}$ is the equilibrium average of U on the donor PES). Substituting this decomposition into Eq. 3.6 yields

$$k^{\text{C}-0}_{\text{A}\leftarrow\text{D}} = \frac{1}{\hbar^2}\Gamma^2_{\text{DA}} \int\limits_{-\infty}^{\infty} d\tau \exp\left(i\langle U\rangle^{\text{eq}}_{\text{D,Cl}}\tau/\hbar\right) \langle \exp\left(i\delta U(\mathbf{R}_0)\tau/\hbar\right)\rangle^{\text{eq}}_{\text{D,Cl}} \tag{3.7}$$

Thus, calculating $k^{\text{C}-0}_{\text{A}\leftarrow\text{D}}$ translates into calculating the Fourier transform of $\langle \exp\left(i\delta U(\mathbf{R}_0)\tau/\hbar\right)\rangle^{\text{eq}}_{\text{D,Cl}}$ at the frequency $\langle U\rangle^{\text{eq}}_{\text{D,Cl}}/\hbar$. It should be noted that $\langle \exp\left(i\delta U(\mathbf{R}_0)\tau/\hbar\right)\rangle^{\text{eq}}_{\text{D,Cl}}$ tends to be a smoothly decaying function compared to $\langle \exp\left(iU(\mathbf{R}_0)\tau/\hbar\right)\rangle^{\text{eq}}_{\text{D,Cl}}$, which tends to be a rapidly oscillating function (when $|\delta U(\mathbf{R})| \ll |\langle U\rangle^{\text{eq}}_{\text{D,Cl}}|$). Hence, Eq. 3.7 allows one to efficiently calculate $k^{\text{C}-0}_{\text{A}\leftarrow\text{D}}$ by using the fast Fourier transform (FFT) method.[136]

The fact that $k^{\text{C}-0}_{\text{A}\leftarrow\text{D}}$ is given in terms of the Fourier transform of $\langle \exp\left(i\delta U(\mathbf{R}_0)\tau/\hbar\right)\rangle^{\text{eq}}_{\text{D,Cl}}$ at the frequency $\langle U\rangle^{\text{eq}}_{\text{D,Cl}}/\hbar$, also implies that calculating it is expected to become computationally more costly with increasing $\left|\langle U\rangle^{\text{eq}}_{\text{D,Cl}}/\hbar\right|$. This is because, asymptotically, the Fourier transform is expected to become increasingly small with increasing frequency, which means that more sampling will be required in order to obtain a converged result (also see discussion below Eq. 3.6).

Obtaining the Marcus-like expression requires replacing $\langle \exp\left(i\delta U(\mathbf{R}_0)\tau/\hbar\right)\rangle^{\text{Cl,eq}}_{\text{D}}$ in Eq. 3.7 by the corresponding second-order cumulant approximation, $\exp\left(-\left(\sigma^{\text{eq}}_{\text{D,Cl}}\right)^2 t^2/2\hbar^2\right)$, where $\sigma^{\text{eq}}_{\text{D,Cl}} = \sqrt{\langle(\delta U)^2\rangle^{\text{eq}}_{\text{D,Cl}}} = \sqrt{\langle U^2\rangle^{\text{eq}}_{\text{D,Cl}} - \left(\langle U\rangle^{\text{eq}}_{\text{D,Cl}}\right)^2}$ is the standard deviation of the donor–acceptor energy gap (at equilibrium on the donor PES). Approximating $\langle \exp\left(i\delta U(\mathbf{R}_0)\tau/\hbar\right)\rangle^{\text{Cl,eq}}_{\text{D}}$ as a Gaussian function of time also implies that the probability density of U is assumed to be Gaussian (at least around $U = 0$). Furthermore, in this case, the Fourier transform in Eq. 3.7 can be calculated analytically and is also a Gaussian function. Thus, $k^{\text{C}-0}_{\text{A}\leftarrow\text{D}}$ in Eq. 3.7 reduces into the following expression

$$k_{\mathrm{A}\leftarrow\mathrm{D}}^{\mathrm{M}} = \frac{1}{\hbar}\Gamma_{\mathrm{DA}}^{2}\sqrt{\frac{2\pi}{\left(\sigma_{\mathrm{D,Cl}}^{\mathrm{eq}}\right)^{2}}}\exp\left[-\frac{\left(\langle U\rangle_{\mathrm{D,Cl}}^{\mathrm{eq}}\right)^{2}}{2\left(\sigma_{\mathrm{D,Cl}}^{\mathrm{eq}}\right)^{2}}\right] \tag{3.8}$$

It should be noted that Eq. 3.8 can be obtained from Eq. 3.6 by assuming that the probability density of U is Gaussian: $\rho(U) \approx \exp\left[-\left(U - \langle U\rangle_{\mathrm{D,Cl}}^{\mathrm{eq}}\right)^{2}/2\left(\sigma_{\mathrm{D,Cl}}^{\mathrm{eq}}\right)^{2}\right] / \sqrt{2\pi\left(\sigma_{\mathrm{D,Cl}}^{\mathrm{eq}}\right)^{2}}$. Because $k_{\mathrm{A}\leftarrow\mathrm{D}}^{\mathrm{M}}$ is proportional to this Gaussian probability density at $U = 0$, its value decreases when the average value of U, $\langle U\rangle_{\mathrm{D,Cl}}^{\mathrm{eq}}$, increases and the corresponding standard deviation, $\sigma_{\mathrm{D,Cl}}^{\mathrm{eq}}$, decreases. However, unlike $k_{\mathrm{A}\leftarrow\mathrm{D}}^{\mathrm{C-0}}$, calculating $k_{\mathrm{A}\leftarrow\mathrm{D}}^{\mathrm{M}}$ does not become computationally more costly when $U = 0$ is shifted further and further away from $\langle U\rangle_{\mathrm{D,Cl}}^{\mathrm{eq}}$. This is because assuming that the probability density is Gaussian implies that it is completely determined by the first and second moments of U (the computational cost of calculating the first and second moments is independent of the shift between $U = 0$ and $\langle U\rangle_{\mathrm{D,Cl}}^{\mathrm{eq}}$).

Equating the r.h.s. of Eq. 3.8 to the traditional Marcus expression

$$k_{\mathrm{A}\leftarrow\mathrm{D}}^{\mathrm{Marcus}} = \frac{1}{\hbar}\Gamma_{\mathrm{DA}}^{2}\sqrt{\frac{\pi}{k_{\mathrm{B}}TE_{r}}}\exp\left[-\frac{\left(\Delta E + E_{r}\right)^{2}}{4k_{\mathrm{B}}TE_{r}}\right] \tag{3.9}$$

leads to the following expressions for the reorganization energy, reaction free energy and activation energy in terms of $\langle U\rangle_{\mathrm{D,Cl}}^{\mathrm{eq}}$ and $\sigma_{\mathrm{D,Cl}}^{\mathrm{eq}}$

$$\begin{aligned} E_{r} &= \left(\sigma_{\mathrm{D}}^{\mathrm{Cl,eq}}\right)^{2}/2k_{\mathrm{B}}T \\ \Delta E &= -E_{r} - \langle U\rangle_{\mathrm{D}}^{\mathrm{Cl,eq}} \\ E_{\mathrm{A}} &= k_{\mathrm{B}}T\frac{\left(\langle U\rangle_{\mathrm{D,Cl}}^{\mathrm{eq}}\right)^{2}}{2\left(\sigma_{\mathrm{D,Cl}}^{\mathrm{eq}}\right)^{2}} \end{aligned} \tag{3.10}$$

It should be noted that the normal ($|\Delta E| < E_{r}$) and inverted ($|\Delta E| > E_{r}$) Marcus regimes correspond to $\langle U\rangle_{\mathrm{D}}^{\mathrm{Cl,eq}} < 0$ and $\langle U\rangle_{\mathrm{D}}^{\mathrm{Cl,eq}} > 0$, respectively (see Figure 3.1).

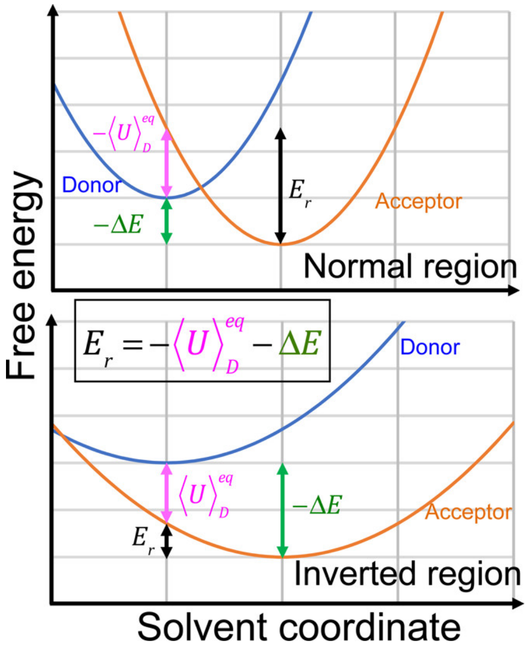

Figure 3.1: A schematic view of the relationship between the average donor–acceptor energy gap, $\langle U \rangle_{\mathrm{D}}^{\mathrm{Cl,eq}}$, the reorganization energy, E_r, and the reaction free energy, ΔE, in the normal (upper panel) and inverted (lower panel) regions (see Equation 3.10).

The identities in Equation 3.10 can be shown to hold in the case where the donor and acceptor PESs are given in terms of identical parabolas which are shifted with respect to their equilibrium geometry and equilibrium energy. However, one advantage of Equation 3.8 over Equation 3.9 is that Equation 3.8 can be used without explicitly expressing the donor and acceptor PESs in this form. Furthermore, expressing the CT rate constant in terms of $\langle U \rangle_{\mathrm{D}}^{\mathrm{Cl,eq}}$ and $\sigma_{\mathrm{D}}^{\mathrm{Cl,eq}}$ is arguably more convenient because unlike E_r and ΔE, they are straightforward to obtain from an equilibrium MD simulation on the donor PES, when the latter is expressed in terms of anharmonic force fields of one's choice.

3.3 Molecular Model and Computational Techniques

3.3.1 Molecular Model

We consider a triad consisting of covalently linked carotenoid polyene (C), diaryl porphyrin (P), and fullerene (C_{60}),[112,137–142] solvated in explicit THF solvent (see Figure 3.2). The molecular model, which is adopted from Reference 112, includes four electronic states: (1) the ground-state, CPC_{60}; (2) the P-localized photoexcited $\pi\pi^*$ state, CP^*C_{60}; (3) the excited P-to-C_{60} CT state, $CP^+C_{60}^-$, which we will refer to as CT1; and (4) the excited C-to-C_{60} charge-separated state, $C^+PC_{60}^-$, which we will refer to as CT2. Starting in the ground-state, this system is believed to go through the following multi-step process, which converts the light energy into electric energy (in the form of charge separation)[112]

$$[CPC_{60}] \overset{h\nu}{\to} [CP^*C_{60}] \to \left[CP^+C_{60}^-\right] \to \left[C^+PC_{60}^-\right] \tag{3.11}$$

The PESs that dictate the dynamics of the nuclear DOF (triad + solvent) differ from one electronic state to another and are given in terms of atom–atom pair potentials that include intermolecular nonbonding Lennard-Jones and Coulomb interactions, as well as the usual intramolecular bonding interactions (bond length, bond angle, and dihedral angle). The force fields differ from one electronic state to another with respect to the Coulomb terms because the partial charges on the triad atoms differ from one electronic state to another. The model also includes electronic coupling coefficients between the excited electronic states (assumed constant within the Condon approximation and calculated via the fragment charge difference (FCD) method[143]). The partial atomic charges for THF were adopted from Reference 144, where they were generated via AM1-BCC.[145] The electronic excitation energies, partial charges, and electronic coupling coefficients for the triad were adopted from Reference 112, where they were obtained via TDDFT using a RSH functional designed

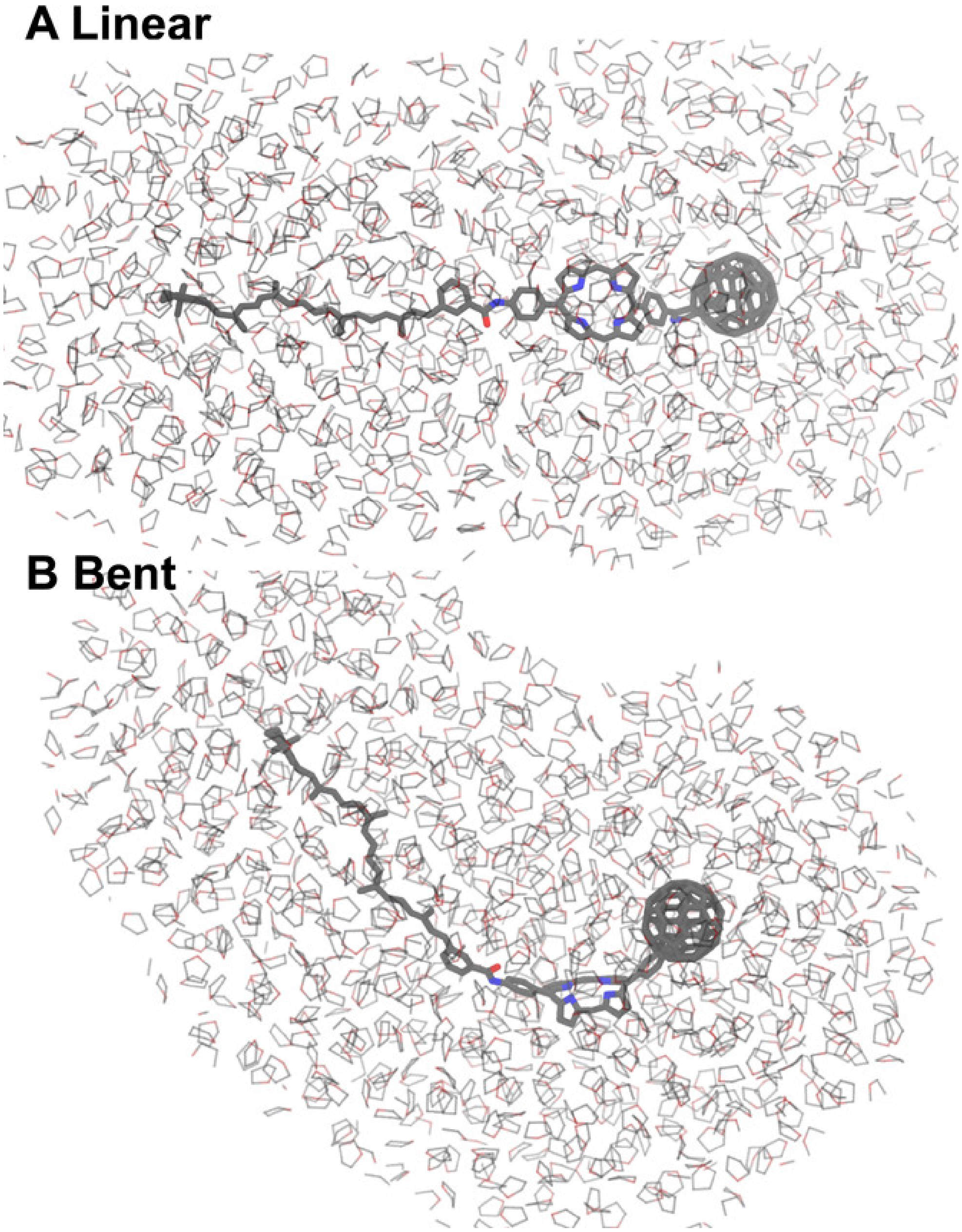

Figure 3.2: The molecular structure of the linear (A) and bent (B) conformations of the carotenoid-porphyrin-C_{60} molecular triad solvated in liquid THF. The triad is in ball-and-stick representation; the carbon, oxygen, and nitrogen atoms are in gray, red, and blue, respectively. For visibility, the hydrogen atoms are not shown and solvent THF molecules within 20 Åof the triad are shown. The figure was generated using Visual Molecular Dynamics (VMD).

to yield accurate energetics for the CT states.

The rate constants between the initial donor (D) state and final acceptor (A) state, D → A, were calculated for the following choices of donor and acceptor states: $\pi\pi^* \rightarrow$ CT1, $\pi\pi^* \rightarrow$ CT2, and CT1 → CT2. To this end, we define $V_{\mathrm{D}}(\mathbf{R},\mathbf{r})$ and $V_{\mathrm{A}}(\mathbf{R},\mathbf{r})$ to be the PESs that correspond to the D and A states, respectively. Here, $\mathbf{R} = (\mathbf{R}_1, ..., \mathbf{R}_N)$ represents the coordinates of the N solvent atoms and $\mathbf{r} = (\mathbf{r}_1, ..., \mathbf{r}_n)$ represents the coordinates of the n triad atoms. Thus, the energy gap between the D and A states is given by $U(\mathbf{R},\mathbf{r}) = V_{\mathrm{D}}(\mathbf{R},\mathbf{r}) - V_{\mathrm{A}}(\mathbf{R},\mathbf{r})$.

The force fields used in the MD simulations are electronic-state-dependent and consist of contributions from solvent–solvent (SS), triad–triad (TT) and solvent–triad (ST) potential energy terms:

$$\begin{aligned}
V_{\alpha,\mathrm{SS}}(\mathbf{R},\mathbf{r}) &= V_{\mathrm{SS}}^{\mathrm{NE}}(\mathbf{R}) + \sum_{J=1}^{N-1}\sum_{J'=J+1}^{N} \frac{1}{4\pi\epsilon_0}\frac{Q_J Q_{J'}}{|\mathbf{R}_J - \mathbf{R}_{J'}|}, \\
V_{\alpha,\mathrm{TT}}(\mathbf{R},\mathbf{r}) &= V_{\mathrm{TT}}^{\mathrm{NE}}(\mathbf{r}) + \sum_{j=1}^{n-1}\sum_{j'=j+1}^{n} \frac{1}{4\pi\epsilon_0}\frac{q_j^{\alpha} q_{j'}^{\alpha}}{|\mathbf{r}_j - \mathbf{r}_{j'}|}, \\
V_{\alpha,\mathrm{ST}}(\mathbf{R},\mathbf{r}) &= V_{\mathrm{ST}}^{\mathrm{NE}}(\mathbf{R},\mathbf{r}) + \sum_{J=1}^{N}\sum_{j=1}^{n} \frac{1}{4\pi\epsilon_0}\frac{Q_j q_j^{\alpha}}{|\mathbf{R}_J - \mathbf{r}_j|}
\end{aligned} \tag{3.12}$$

Here, $\alpha = \{\pi\pi^*, \text{CT1}, \text{CT2}\}$, $V_{\mathrm{SS}}^{\mathrm{NE}}(\mathbf{R})$, $V_{\mathrm{TT}}^{\mathrm{NE}}(\mathbf{r})$, and $V_{\mathrm{ST}}^{\mathrm{NE}}(\mathbf{R},\mathbf{r})$ include the nonelectrostatic bonding and nonbonding interactions (assumed to be independent of the triad's electronic state), $\{Q_J\}$ represents the partial charges assigned to the solvent atoms (assumed to be independent of the triad's electronic state), $\{q_j\}$ represents the partial charges assigned to the triad atoms (assumed to be dependent of the triad's electronic state).

Let the gas-phase energies of the ground, $\pi\pi^*$, CT1, and CT2 electronic states, at the ground state equilibrium geometry, $\mathbf{r}^{\mathrm{G,eq}}$, be given by $E_{\mathrm{G}}, E_{\pi\pi^*}, E_{\mathrm{CT1}}, E_{\mathrm{CT2}}$, respectively. It should be noted that those energies already include the triad–triad interactions in the ground state equilibrium geometry. Thus, we need to subtract that interaction energy in order to avoid double counting. It is also convenient to set the energy origin to $E_{\rm G}$ (so that $E_{\rm G} \to 0$). The overall PES in different electronic states is therefore given by

$$V_\alpha(\mathbf{R}, \mathbf{r}) = E_\alpha - E_{\rm G} - V_{\alpha,{\rm TT}}(\mathbf{r}^{\rm G,eq}) + V_{\alpha,{\rm SS}}(\mathbf{R}, \mathbf{r}) + V_{\alpha,{\rm TT}}(\mathbf{R}, \mathbf{r}) + V_{\alpha,{\rm ST}}(\mathbf{R}, \mathbf{r}) \quad (3.13)$$

It should be noted that for the force fields used here, $U(\mathbf{R}, \mathbf{r})$ only depends on electrostatic interactions. This is because the nonelectrostatic component of $V_{\rm D}(\mathbf{R}, \mathbf{r})$ and $V_{\rm A}(\mathbf{R}, \mathbf{r})$ are identical and cancel out when one is subtracted from the other. It should also be noted that $V_{\rm D}(\mathbf{R}, \mathbf{r})$, $V_{\rm A}(\mathbf{R}, \mathbf{r})$, and $U(\mathbf{R}, \mathbf{r})$ can be written as sums of an intramolecular (triad–triad) and an intermolecular (triad–solvent and solvent–solvent) contribution. Because the solvent–solvent contribution is the same for $V_{\rm D}(\mathbf{R}, \mathbf{r})$ and $V_{\rm A}(\mathbf{R}, \mathbf{r})$, the solvent–solvent contribution to $U(\mathbf{R}, \mathbf{r})$ vanishes.

As shown in Reference 112, the triad can exist in two different conformations – *linear* and *bent* (see Figure 3.2). Although the bent conformation was found to be thermodynamically more favorable, the rate of the CT process CT1 → CT2 is found to be faster in the linear conformation.[112] Hence, the CT rate constants need to be calculated separately for each conformation.

3.3.2 MD Simulations

MD simulations were performed within AMBER14[146] using a 100 Å×100 Å×100 Å periodic cubic simulation box containing one triad molecule and 6741 THF molecules, as described in References 144 and 147. The general AMBER force field was employed,[148–150] with customized partial atomic charges as described above. After energy minimization using a steepest descent and conjugate gradient method, the system was gradually heated to 300 K. During this process, the triad conformation was maintained by using a harmonic potential of force constant of 100 kcal mol^{-1}Å^{-2} to constrain the distance between the two carbon atoms nearest to the two termini to its characteristic value in the corresponding conformation.

The SHAKE algorithm[151] was used to constrain the covalent bonds involving hydrogen atoms. The integration time step was 1.0 fs. For equilibration, we employed Langevin dynamics with a collision frequency of 1.0 ps^{-1}. A cutoff of 12 Åwas employed for the van der Waals interactions. Particle mesh Ewald summation was used to calculate the electrostatic interactions.[152] Next, we released the constraints on the triad molecule and equilibrated the system at 300 K in an NPT ensemble to reach a desired density of THF and an NVT ensemble for 100 ps.

In order to investigate the impact of intermolecular vs. intramolecular DOF on the CT rates, we repeated the calculations with a rigid triad molecule. All the atoms of the triad molecule were subjected to a stiff restraint by applying a harmonic force with force constant of 100 kcal $\mathrm{mol}^{-1}\mathrm{Å}^{-2}$. In total, we performed four different simulations for each of the three CT processes ($\pi\pi^* \to$ CT1, $\pi\pi^* \to$ CT2 and CT1 $\to$ CT2): (1) rigid triad in linear conformation; (2) rigid triad in bent conformation; (3) flexible triad in linear conformation; (4) flexible triad in bent conformation. For each of the conditions, we adopted the following procedures. First, starting with a ground-state equilibrium configuration, we carried out MD simulations on the initial excited-state PES, for 2.0 ns, in the NVT ensemble, to reach equilibrium on the initial excited-state PES. Second, we performed an 8.0 ns long production simulation, where we recorded the donor–acceptor energy gap, $U(\mathbf{R}, \mathbf{r})$, along the trajectories at 5 fs intervals. Error bars were calculated by splitting the 8.0 ns long production trajectory into four 2.0 ns long segments, calculating the rate constants separately for each segment, and equating the error bar to the corresponding standard deviation (uncorrected for sample size).

3.3.3 Amide I Stretch Frequency Distributions

The signature of the different CT states and conformations on the IR spectrum of the amide I stretch were evaluated via the following procedure. Forty configurations were randomly picked from the equilibrium MD trajectories of the flexible triad in the $\pi\pi^*$, CT1, and CT2 states, in both linear and bent conformations (i.e., 240 configurations overall). Within each configuration, the carbon and oxygen of the amide I stretch were shifted along the bond axis while keeping the center of mass fixed. Thirteen equally spaced grid points were chosen within a range of 0.7 Å. Single-point energy calculations were performed at each of the 13 grid points, via Q-Chem 4.4 and using the ωB97X–D long-range corrected hybrid density functional and the 6-31G* basis set. For the CT1 and CT2 states, constrained DFT was used to constrain charges to the donor/acceptor regions (porphyrin/C_{60} in the case of CT1 and carotene/C_{60} in the case of CT2). The amide I C–O stretch was excluded from the constrained fragments in each case. The calculated energies were then fitted to a Morse potential, followed by the evaluation of the corresponding fundamental frequency and first overtone (using the reduced mass of carbon monoxide, 6.857 amu). The spectral signature of the different conformations and excited electronic states was obtained by comparing the corresponding amide I fundamental frequency (ω_{10}) and anharmonicity ($\omega_{10} - \omega_{21}$) distributions.

3.4 Results

The $\pi\pi^* \rightarrow$ CT1, $\pi\pi^* \rightarrow$ CT2 and CT1 $\rightarrow$ CT2 rate constants, calculated via Equations 3.7 and 3.8, in the bent and linear conformations, are presented in Tables 3.1 and 3.2, respectively. Results are shown for the flexible and rigid triad cases. It should be noted that we were unable to obtain a converged value of $k^{\mathrm{C-0}}_{\mathrm{A\leftarrow D}}$ for CT1 $\rightarrow$ CT2 in the bent/rigid case, which is attributed to the exceedingly small value of the Fourier transform in this case (see Equation 3.7).

	bent/flexible		bent/rigid	
	$k^{\mathrm{M}}_{\mathrm{A\leftarrow D}}$ [s^{-1}]	$k^{\mathrm{C-0}}_{\mathrm{A\leftarrow D}}$ [s^{-1}]	$k^{\mathrm{M}}_{\mathrm{A\leftarrow D}}$ [s^{-1}]	$k^{\mathrm{C-0}}_{\mathrm{A\leftarrow D}}$ [s^{-1}]
$\pi\pi^* \rightarrow$ CT1	$(3.0 \pm 0.2) \times 10^{11}$	$(2.9 \pm 0.2) \times 10^{11}$	$(3.6 \pm 0.7) \times 10^{11}$	$(3.9 \pm 0.6) \times 10^{11}$
$\pi\pi^* \rightarrow$ CT2	$(8.0 \pm 2.0) \times 10^{6}$	$(8.0 \pm 2.0) \times 10^{6}$	$(9.2 \pm 0.2) \times 10^{6}$	$(9.7 \pm 0.4) \times 10^{6}$
CT1 $\rightarrow$ CT2	$(2.3 \pm 0.6) \times 10^{2}$	$(2.2 \pm 0.2) \times 10^{2}$	$(3.2 \pm 0.2) \times 10^{2}$	——

Table 3.1: Donor-to-acceptor rate constants for the triad in the bent conformation.

	linear/flexible		linear/rigid	
	$k^{\mathrm{M}}_{\mathrm{A\leftarrow D}}$ [s^{-1}]	$k^{\mathrm{C-0}}_{\mathrm{A\leftarrow D}}$ [s^{-1}]	$k^{\mathrm{M}}_{\mathrm{A\leftarrow D}}$ [s^{-1}]	$k^{\mathrm{C-0}}_{\mathrm{A\leftarrow D}}$ [s^{-1}]
$\pi\pi^* \rightarrow$ CT1	$(1.12 \pm 0.04) \times 10^{12}$	$(1.17 \pm 0.02) \times 10^{12}$	$(1.1 \pm 0.1) \times 10^{12}$	$(1.0 \pm 0.1) \times 10^{12}$
$\pi\pi^* \rightarrow$ CT2	$(1.9 \pm 0.2) \times 10^{8}$	$(1.86 \pm 0.02) \times 10^{8}$	$(1.90 \pm 0.04) \times 10^{8}$	$(2.0 \pm 0.1) \times 10^{8}$
CT1 $\rightarrow$ CT2	$(1.0 \pm 0.2) \times 10^{9}$	$(1.1 \pm 0.3) \times 10^{9}$	$(5.8 \pm 0.9) \times 10^{8}$	$(6.0 \pm 1.0) \times 10^{8}$

Table 3.2: Donor-to-acceptor rate constants for the triad in the linear conformation.

The results in Tables 3.1 and 3.2 follow the same trends reported in Reference 112. More specifically, photoinduced CT in this system is observed to occur through a two-step process: $\pi\pi^* \rightarrow \mathrm{CT1} \rightarrow \mathrm{CT2}$, rather than through a direct one-step process, $\pi\pi^* \rightarrow \mathrm{CT2}$. This is because the first step, $\pi\pi^* \rightarrow \mathrm{CT1}$, is much faster than the direct one-step process, $\pi\pi^* \rightarrow \mathrm{CT2}$. Furthermore, the rate of the second step, CT1 → CT2, is observed to be faster in the linear conformation, by a factor of $10^6 - 10^7$, than in the bent conformation. This implies that although the bent conformation is thermodynamically more favorable than the linear conformation, the CT1 → CT2 process is far more likely to occur in the linear conformation. On the basis of those observations, the bent → linear conformational reaction is the rate-determining step for CT in this system. This observation highlights the potentially strong correlation between molecular structure and CT dynamics, and thereby the possibility of controlling the latter by modifying the former. It should be noted that, similar to the rate constants reported in Reference 112, the rate constants in Tables 3.1 and 3.2 are also in reasonable agreement with the reported experimental estimates for the $\pi\pi^*$ → CT1 rate constant, 3.3×10^{11} s^{-1}, and CT1 → CT2 rate constant, 1.5×10^{10} s^{-1}.[153]

With one exception (CT1 → CT2 in bent/flexible case), the $k^{\mathrm{M}}_{\mathrm{A}\leftarrow\mathrm{D}}$ values for the bent/flexible and linear/flexible cases were found to agree rather well with the corresponding values reported in Reference 112. It should be noted that the values of $k_{\mathrm{A}\leftarrow\mathrm{D}}$ reported in Reference 112 were obtained by using the standard Marcus expression, Equation 3.9, with ΔE and E_r given by[94,154,155]

$$\begin{aligned}\Delta E &= \frac{1}{2}\left[\langle V_{\mathrm{A}} - V_{\mathrm{D}}\rangle^{\mathrm{eq}}_{\mathrm{D,Cl}} + \langle V_{\mathrm{A}} - V_{\mathrm{D}}\rangle^{\mathrm{eq}}_{\mathrm{A,Cl}}\right] \\ E_r &= \frac{1}{2}\left[\langle V_{\mathrm{A}} - V_{\mathrm{D}}\rangle^{\mathrm{eq}}_{\mathrm{D,Cl}} - \langle V_{\mathrm{A}} - V_{\mathrm{D}}\rangle^{\mathrm{eq}}_{\mathrm{A,Cl}}\right] \end{aligned} \qquad (3.14)$$

It can be shown that the expressions for ΔE and E_r in Equation 3.14 would give the same values as the expressions in Equation 3.10 in the case where the donor and acceptor PESs are given in terms of identical parabolas which are shifted with respect to their equilibrium geometry and equilibrium energy. However, it should also be noted that Equations 3.14 and 3.10 need not agree when one deviates from the shifted identical parabolas model. Thus, the agreement between the predictions obtained via Equations 3.14 and 3.10 provides further support to the self-consistency of the linear-response-based picture based on which the donor and acceptor PESs can be mapped onto shifted, but otherwise identical, effective parabolas[107–110] (although in practice one obviously does not need to explicitly cast the Hamiltonian in this form).

The one exception is observed for the CT1 → CT2 rate constant in the bent/flexible case. In this case, our prediction $k^{\mathrm{M}}_{\mathrm{A}\leftarrow\mathrm{D}} = (2.3 \pm 0.6) \times 10^2 \mathrm{s}^{-1}$, is significantly smaller than that reported in Reference 112, $k_{\mathrm{A}\leftarrow\mathrm{D}} = 6.6 \times 10^3 \mathrm{s}^{-1}$. The difference may be either due to deviations from the shifted but otherwise identical parabolas picture or the fact that this rate constant is particularly small and thereby more difficult to converge (no error bars were reported in Reference 112).

We next consider the validity of the second-order cumulant approximation by comparing the values of $k^{\mathrm{M}}_{\mathrm{A}\leftarrow\mathrm{D}}$ and $k^{\mathrm{C-0}}_{\mathrm{A}\leftarrow\mathrm{D}}$. Within error bars, $k^{\mathrm{M}}_{\mathrm{A}\leftarrow\mathrm{D}}$ and $k^{\mathrm{C-0}}_{\mathrm{A}\leftarrow\mathrm{D}}$ are observed to have the same value in all cases. Furthermore, comparison of the probability densities of the donor–acceptor energy gaps, U, with the corresponding Gaussian approximations reveals excellent agreement across the entire range of U values and not just at the vicinity of $U = 0$ (see Figures 3.3 and 3.4). These observations serve as strong validation of the accuracy of the second order-cumulant approximation for this system, and the Marcus-like expression for the rate constant derived based on it (see Equation 3.8). It should be noted that the ability of the second-order cumulant approximation to produce predictions that are *quantitatively* indistinguishable from those obtained without making this approximation is not self-evident for a molecular system of the level of complexity of the triad + solvent. Furthermore, the fact that the Marcus-like expression in Equation 3.8 is consistent with experiment cannot be taken as proof for the validity of the second-order cumulant approximation. However, comparing the effect on the CT rate constants of removing this approximation, as we have done here, can provide such a proof. Thus, following the procedure outlined here provides a practical way of testing the assumptions underlying Marcus theory and avoiding them when they are observed not to be valid.[91]

The validity of the second-order cumulant approximation suggests that the rate constants can be rationalized within the framework of Marcus theory. To this end, we calculated the reorganization energies, reaction free energies, and activation energies from the first and second moments of the donor–acceptor energy gap, Equation 3.10 (see Tables 3.3–3.6). It should be noted that with the exception of $\pi\pi^* \to$ CT1 in the bent conformation, all cases correspond to the Marcus normal regime ($|\Delta E| < E_r$). The fact that $\pi\pi^* \to$ CT1 in the bent conformation correspond to the inverted regime is also manifested by the fact that this is the only case where $\langle U \rangle^{\mathrm{Cl,eq}}_{\mathrm{D}}$ is positive (see

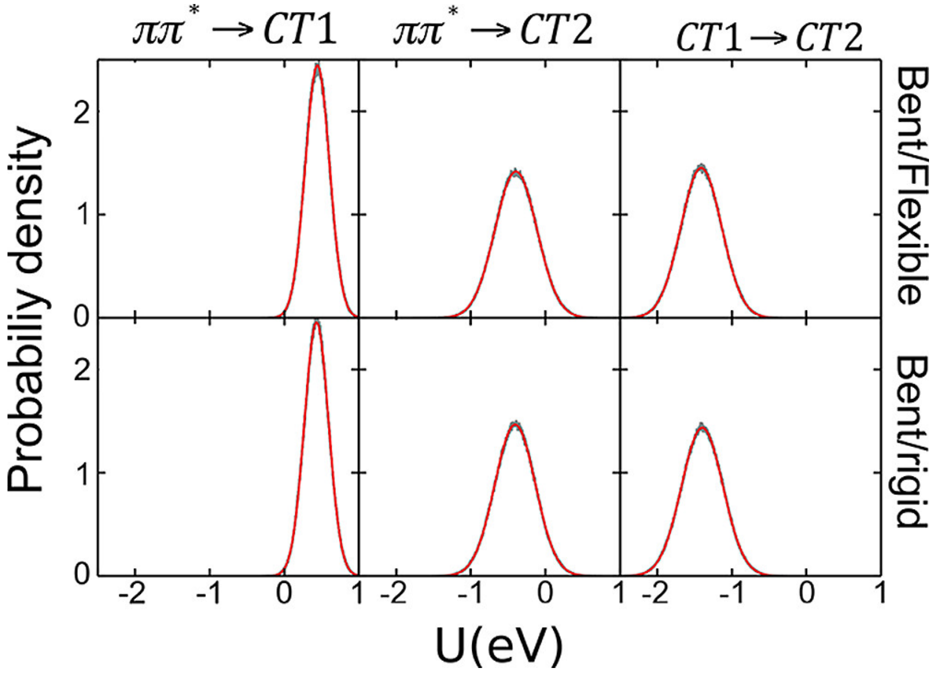

Figure 3.3: A comparison between the probability densities (black) of the donor-acceptor energy gaps, U, and the corresponding Gaussian approximations (red), for the flexible (upper panels) and rigid (lower panels) bent conformation.

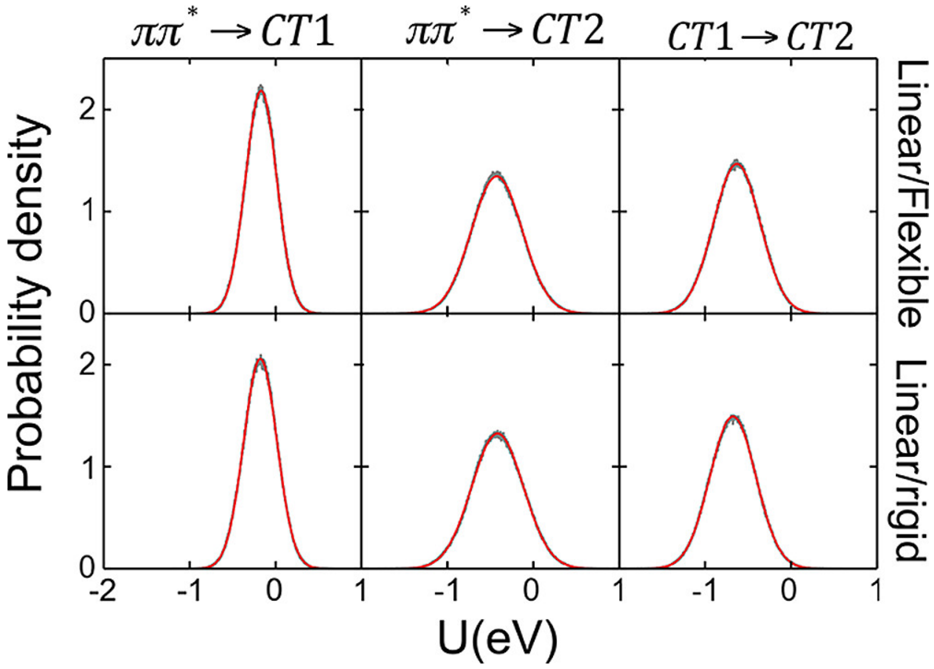

Figure 3.4: A comparison between the probability densities (black) of the donor-acceptor energy gaps, U, and the corresponding Gaussian approximations (red), for the flexible (upper panels) and rigid (lower panels) linear conformation.

comment below Equation 3.10).

	Γ^2_{DA} [eV^2]	$\langle U\rangle^{\mathrm{Cl,eq}}_{\mathrm{D}}$ [eV]	$\left(\sigma^{\mathrm{Cl,eq}}_{\mathrm{D}}\right)^2$ [eV^2]	E_r [eV)]	ΔE [eV)]	E_{A} [eV)]
$\pi\pi^* \rightarrow$ CT1	5.8×10^{-4}	0.444	0.027	0.515	–0.959	0.096
$\pi\pi^* \rightarrow$ CT2	2.0×10^{-9}	–0.394	0.079	1.531	–1.137	0.025
CT1 $\rightarrow$ CT2	7.4×10^{-9}	–1.410	0.076	1.460	–0.050	0.340

Table 3.3: Squared electronic coupling coefficients (Γ^2_{DA}), average ($\langle U\rangle^{\mathrm{Cl,eq}}_{\mathrm{D}}$) and variance ($\left(\sigma^{\mathrm{Cl,eq}}_{\mathrm{D}}\right)^2$) of donor–acceptor energy gap, reorganization energy (E_r), reaction free energy (ΔE), and activation energy (E_{A}) for a flexible triad in the bent conformation.

	Γ^2_{DA} [eV^2]	$\langle U\rangle^{\mathrm{Cl,eq}}_{\mathrm{D}}$ [eV]	$\left(\sigma^{\mathrm{Cl,eq}}_{\mathrm{D}}\right)^2$ [eV^2]	E_r [eV]	ΔE [eV]	E_{A} [eV]
$\pi\pi^* \rightarrow$ CT1	5.8×10^{-4}	0.432	0.026	0.511	–0.943	0.091
$\pi\pi^* \rightarrow$ CT2	2.0×10^{-9}	–0.406	0.074	1.431	–1.025	0.026
CT1 $\rightarrow$ CT2	7.4×10^{-9}	–1.397	0.077	1.493	–0.096	0.327

Table 3.4: Squared electronic coupling coefficients (Γ^2_{DA}), average ($\langle U\rangle^{\mathrm{Cl,eq}}_{\mathrm{D}}$) and variance ($\left(\sigma^{\mathrm{Cl,eq}}_{\mathrm{D}}\right)^2$) of donor–acceptor energy gap, reorganization energy (E_r), reaction free energy (ΔE), and activation energy (E_{A}) for a rigid triad in the bent conformation.

Both $\pi\pi^* \rightarrow$ CT1 and $\pi\pi^* \rightarrow$ CT2 are seen to have relatively small activation energies. The activation energy for $\pi\pi^* \rightarrow$ CT2 is seen to be larger/smaller than that for $\pi\pi^* \rightarrow$ CT1 in the linear/bent conformations. Thus, the fact that $\pi\pi^* \rightarrow$ CT1 is much faster than $\pi\pi^* \rightarrow$ CT2 in both conformations is mostly due to the larger electronic coupling.

The much faster rate of CT1 $\rightarrow$ CT2 in the linear conformation compared to the bent conformation can also be traced back to both effects (the activation energy in the linear conformation is lower by a factor of five and the squared electronic coupling coefficient in the linear conformation is larger by a factor of 135). However, the fact that the CT1 $\rightarrow$ CT2 rate constant in the linear conformation is larger by a factor of $10^6 - 10^7$ suggests that lowering the activation barrier plays the decisive role in this

	Γ^2_{DA} [eV^2]	$\langle U\rangle_{\mathrm{D}}^{\mathrm{Cl,eq}}$ [eV]	$\left(\sigma_{\mathrm{D}}^{\mathrm{Cl,eq}}\right)^2$ [eV^2]	E_r [eV]	ΔE [eV]	E_{A} [eV]
$\pi\pi^* \to$ CT1	8.1×10^{-5}	–0.169	0.033	0.645	–0.477	0.011
$\pi\pi^* \to$ CT2	4.0×10^{-8}	–0.425	0.088	1.703	–1.278	0.026
CT1 $\to$ CT2	1.0×10^{-6}	–0.631	0.074	1.431	–0.799	0.070

Table 3.5: Squared electronic coupling coefficients (Γ^2_{DA}), average ($\langle U\rangle_{\mathrm{D}}^{\mathrm{Cl,eq}}$) and variance ($\left(\sigma_{\mathrm{D}}^{\mathrm{Cl,eq}}\right)^2$) of donor–acceptor energy gap, reorganization energy (E_r), reaction free energy (ΔE), and activation energy (E_{A}) for a flexible triad in the linear conformation.

	Γ^2_{DA} [eV^2]	$\langle U\rangle_{\mathrm{D}}^{\mathrm{Cl,eq}}$ [eV]	$\left(\sigma_{\mathrm{D}}^{\mathrm{Cl,eq}}\right)^2$ [eV^2]	E_r [eV]	ΔE [eV)]	E_{A} [eV]
$\pi\pi^* \to$ CT1	8.1×10^{-5}	–0.177	0.038	0.728	–0.551	0.011
$\pi\pi^* \to$ CT2	4.0×10^{-8}	–0.417	0.091	1.757	–1.340	0.025
CT1 $\to$ CT2	1.0×10^{-6}	–0.677	0.072	1.385	–0.708	0.083

Table 3.6: Squared electronic coupling coefficients (Γ^2_{DA}), average ($\langle U\rangle_{\mathrm{D}}^{\mathrm{Cl,eq}}$), and variance ($\left(\sigma_{\mathrm{D}}^{\mathrm{Cl,eq}}\right)^2$) of donor–acceptor energy gap, reorganization energy (E_r), reaction free energy (ΔE), and activation energy (E_{A}) for a rigid triad in the linear conformation.

case. Because the reorganization energies for CT1 → CT2 in the bent and linear conformations are similar, the lowered activation energy in the linear conformation can be traced back to the corresponding more negative value of ΔE. Alternatively, the same effect can also be rationalized by noting that while the width of the U distribution, $\sigma_{\mathrm{D}}^{\mathrm{Cl,eq}}$, is similar for both conformations, the average of U squared, $\left(\langle U\rangle_{\mathrm{D}}^{\mathrm{Cl,eq}}\right)^2$, is larger by a factor of five in the bent conformation.

The values of $\left(\sigma_{\mathrm{D}}^{\mathrm{Cl,eq}}\right)^2$ in Tables 3.3–3.6 can also be used to test the validity of the assumption that $\langle \exp\left(i\int_0^\tau d\tau'\delta U(\mathbf{R}_{\tau'})/\hbar\right)\rangle_{\mathrm{D,Cl}}^{\mathrm{eq}}$ decays faster than the nuclear dynamics timescale on which $U(\mathbf{R}_{\tau'})$ changes, which was employed to obtain Equation 3.6) from Equation 3.5. To this end, we note that $\langle \exp\left(i\delta U(\mathbf{R}_0)\tau/\hbar\right)\rangle_{\mathrm{D}}^{\mathrm{Cl,eq}} \approx \exp\left(-\left(\sigma_{\mathrm{D,Cl}}^{\mathrm{eq}}\right)^2\tau^2/2\hbar^2\right)$. Thus, the time scale of the decay of $\langle \exp\left(i\delta U(\mathbf{R}_0)\tau/\hbar\right)\rangle_{\mathrm{D}}^{\mathrm{Cl,eq}}$ can be estimated by $\sqrt{2\hbar^2/\left(\sigma_{\mathrm{D}}^{\mathrm{Cl,eq}}\right)^2}$. For the system under consideration here, those time scales are in the range of 3–6 fs, which are indeed faster than the nuclear dynamics time scale.

Another interesting comparison is between the values of $k^{\mathrm{M}}_{\mathrm{A}\leftarrow\mathrm{D}}$ and $k^{\mathrm{C-0}}_{\mathrm{A}\leftarrow\mathrm{D}}$ obtained in the rigid and flexible cases. The results in Tables 3.1 and 3.2 show that freezing the triad's intramolecular DOF either has no effect (linear conformation) or a rather minor effect (bent conformation) on the values of $k^{\mathrm{M}}_{\mathrm{A}\leftarrow\mathrm{D}}$ and $k^{\mathrm{C-0}}_{\mathrm{A}\leftarrow\mathrm{D}}$. This suggests that CT in this system is driven by the intermolecular (solvent) DOF, rather than by the intramolecular (triad) DOF. Here too, it is not self-evident that this would be the case, in light of the triad's size and flexibility.

It should be noted that strictly speaking, treating the intramolecular vibrations as classical is an approximation, which may break down in the case of high frequency modes, particularly in the inverted region. However, as pointed up above, the only case that corresponds to the inverted region is $\pi\pi^* \rightarrow$ CT1 in the bent conformation. Thus, even if the $\pi\pi^* \rightarrow$ CT1 rate could have been made faster by accounting for the quantum nature of intramolecular vibrations, our conclusions would still hold. This is because the CT1 → CT2 rate in the bent conformation is significantly slower than that in the linear conformation. It should also be noted that the triad molecule is rather large and flexible. Thus, intramolecular reorganization is expected to be dominated by collective low-frequency modes for which one expects the classical treatment to be a reasonable approximation.

Next, we consider the triad's amide I stretch frequency distributions and their dependence on the electronic and conformational states of the triad. The triad's amide I stretch fundamental frequency (ω_{10}) and anharmonicity ($\omega_{10} - \omega_{21}$) distributions are shown in Figures 3.5 and 3.6, respectively. It should be noted that the range of the fundamental frequency distributions in Figure 3.5, 1,800–2,000 cm^{-1}, is higher by ∼5% relative to the gas-phase amide I stretch frequency in N-methyl acetamide (1,717 cm^{-1}).[156] Such a discrepancy is common in *ab initio* calculations of vibrational frequencies, and following the common practice, we will treat it as systematic.[157]

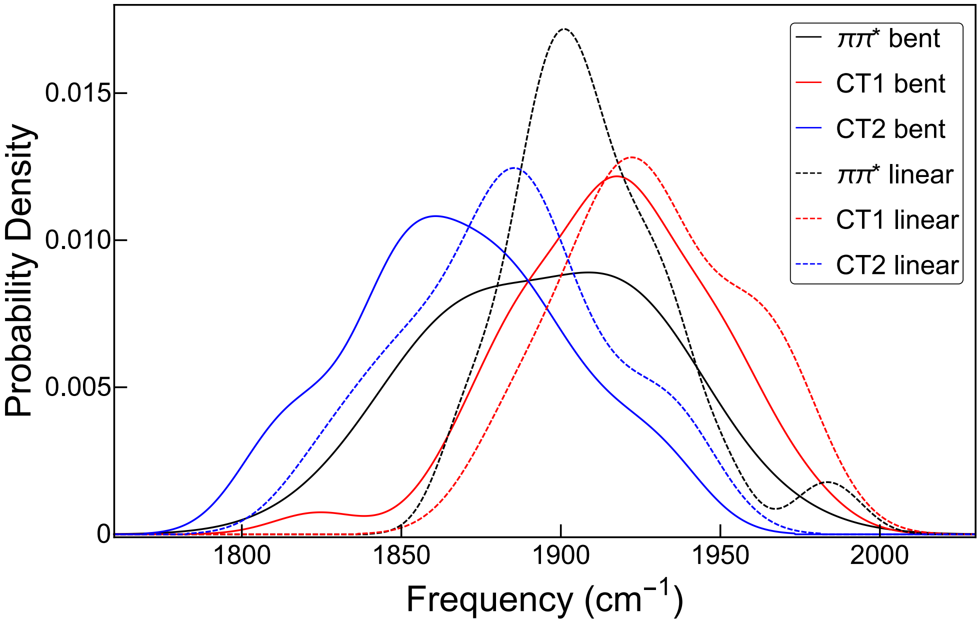

Figure 3.5: The amide I fundamental frequency distributions for the $\pi\pi^*$ (black), CT1 (red), and CT2 (blue) electronic states, in the bent (solid line) and linear (dashed line) conformations.

It should be noted that the fact that the anharmonicity range is 10–13 cm^{-1} (see Figure 3.6), which is in agreement with the gas-phase value for N-methyl acetamide, 12.38 cm^{-1},[156] provides some validation to this assumption. It should also be noted that the widths of the amide I stretch frequency distributions in Figure 3.5 are on the order of ∼100 cm^{-1}, which is comparable to previously reported values for the amide I stretch in polar media.[156,158,159] Thus, we will assume that the trends seen with respect to the dependence of the amide I stretch frequency on the conformational and CT state are reliable.

Figure 3.5 shows that the amide I stretch fundamental frequency distributions are very sensitive to the electronic state. More specifically, the frequency distribution in the CT1 state is seen to be blue-shifted relative to the CT2 state by as much as ∼60 cm^{-1} and ∼40 cm^{-1} in the bent and linear conformations, respectively. The frequency distribution in the $\pi\pi^*$ state lies in between the frequency distributions in the CT1 and CT2 states. Thus, within a time-resolved UV–vis/IR pump–probe experiment,

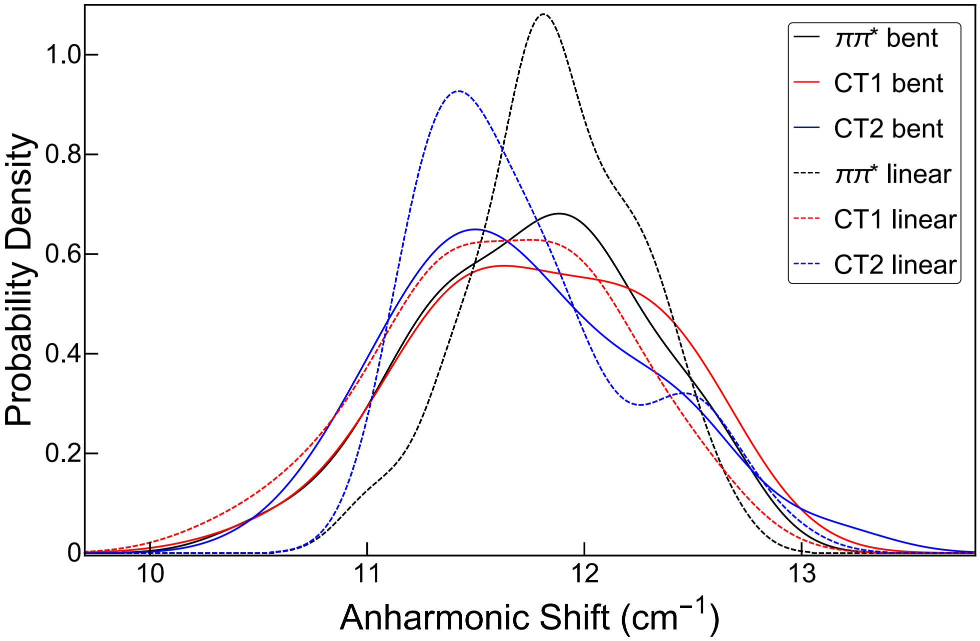

Figure 3.6: The amide I anharmonicity distributions for the $\pi\pi^*$ (black), CT1 (red), and CT2 (blue) electronic states, in the bent (solid line) and linear (dashed line) conformations.

one would expect the two-step CT process $\pi\pi^* \rightarrow$ CT1 $\rightarrow$ CT2 to manifest itself by a red shift at short delays between the UV–vis photoexcitation and the IR probe, due to the first step ($\pi\pi^* \rightarrow$ CT1), followed by an even larger red shift at longer delays, due to the second step (CT1 $\rightarrow$ CT2).

Figure 3.5 also shows that the amide I stretch fundamental frequency distributions are sensitive to the triad's conformation, although to a lesser extent than to the electronic state. Most noticeably, the frequency distribution in the $\pi\pi^*$ state is seen to be significantly narrower in the linear conformation in comparison to the bent conformation. This can be attributed to the larger entropy of the bent conformation, which implies a larger number of microstates and thereby a wider frequency distribution. The frequency distributions also narrow down when going from the bent to the linear conformations in the case of the CT1 and CT2 states, although to a lesser extent, which can be attributed to electrostriction.

Although it is evident that the amide I frequency shifts are sensitive to the charge

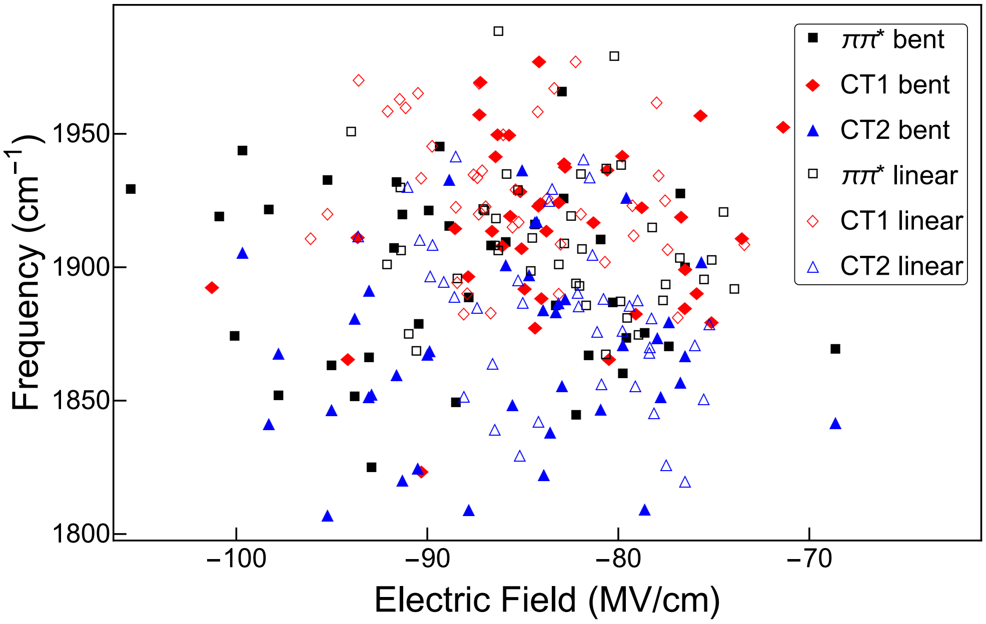

Figure 3.7: Correlation plot between the triad's amide I stretch frequency and the electric field along the C-O bond for the $\pi\pi^*$ (black), CT1 (red), and CT2 (blue) electronic states, in the bent (filled symbols) and linear (unfilled symbols) conformations.

redistribution in its vicinity, we have also attempted to correlate the frequency shifts with an order parameter that can capture the effect of charge distribution. To this end and following previous works,[157–159] we examined the correlation between the frequency shift and the electric field and electric field gradient along the amide I C–O bond. The correlation plot between the amide I fundamental frequency and the electric field along the C–O bond is shown in Figure 3.7. The results reveal a somewhat surprising lack of correlation between the frequency and the electric field along the C–O bond. A similar lack of correlation was observed between the amide I frequency and the electric field gradient. The lack of correlation seems to suggest that the frequency shift is a through-bond quantum-chemical effect, mediated by the large degree of conjugation within the triad molecule, rather than a through-space Stark shift effect.

Finally Figure 3.6 shows that the anharmonicity is significantly less sensitive to both conformational and CT state. The fact that the anharmonicity is significantly smaller than the width of the fundamental frequency distributions suggests that they will be masked by the signal from the fundamental transition. Furthermore, the fact that the shifts are on the order of $\sim$1.0 cm^{-1} would make them hard to resolve experimentally.

3.5 Conclusions

In this chapter, we demonstrate the applicability of the recently proposed LSC-based methodology for calculating CT rate constants in complex molecular systems described by general anharmonic force fields on a molecular model of the carotenoid–porphyrin–C_{60} triad solvated in a THF explicit liquid solvent. Starting with the LSC approximation of the equilibrium FGR expression for the CT rate constant, we derived a hierarchy of progressively more approximate expressions for the CT rate constant. The classical-like nature of the LSC-based FGR expression and approximations derived from it implies that they can be applied to complex molecular systems governed by anharmonic force fields of one's choice. As a result, it becomes possible to test the validity of the various approximations by comparing the CT rate constants obtained with and without making them.

Here, we used this methodology to test the validity of the second-order cumulant approximation, which leads to a Marcus-like expression for the CT rate constant. We did so by calculating the CT rate constants between the three excited states of the triad ($\pi\pi^*$, CT1, CT2) in its two conformations (bent and linear) with and without making the second-order cumulant approximation. The comparison confirmed that the second-order cumulant approximation is quantitatively accurate. The Marcus-like expression based on the second-order cumulant approximation was also found to be in agreement with previously reported Marcus theory rate constants[112] obtained for this system via a different scheme.[94,154,155] We also confirmed the strong dependence of CT dynamics on the triad's conformation reported in Reference 112, which suggests that the bent → linear conformational reaction is the rate-determining step for CT in this system.

One of the advantages of being able to calculate CT rate constants within the framework of a molecular model is that it makes it possible to address questions of a truly molecular nature in a direct manner. This was demonstrated here by investigating the roles of intramolecular versus intermolecular DOF on the CT rate constant. We did so by comparing the calculated CT rate constants obtained with a flexible triad molecule to those obtained with a rigid triad molecule. The results of this comparison showed that CT in this system is driven by the intermolecular (solvent) DOF, rather than by the intramolecular (triad) DOF. This highlights the potentially important impact that interactions with the host can have on CT rates and thereby of the importance of calculating CT rates based on molecular models that includes an explicit host as well as an accurate description of its interactions with the solute.

It should also be noted that functionalization of the triad may enhance the role played by intramolecular DOF in driving CT. At this point, whether or not and to what extent such modifications can be used to control CT rates remain an open question. The methodology outlined in this paper can be used to shed light on such questions. It should also be noted that at least for the system under consideration here, our results suggest that gas-phase simulations of CT would be of limited value when it comes to capturing the true nature of the CT process when it takes place in a moderately polar condensed-phase medium.

One way for experimentally monitoring the CT processes in real time is via time-resolved UV–vis/IR pump–probe spectroscopy. To this end, we examined the sensitivity of the triad's amide I stretch fundamental frequency and anharmonicity to the triad's electronic state and conformational state. Our results show that the amide I fundamental frequency could be a very sensitive probe of CT dynamics in the triad system under consideration, with distinct spectral shifts of ∼40-60 cm^{-1} as one moves from one excited electronic state to another. At the same time, we also showed that the amide I fundamental frequency is not as sensitive to the triad's conformation.

The work presented herein can be extended in many directions, including accounting for nonequilibrium initial states by using the recently introduced LSC-based methodology for calculating nonequilibrium FGR rates,[160] using polarizable force fields,[147] applying the methodology to interfacial CT in organic photovoltaic systems,[161–163] and exploring other vibrational modes as IR probes of CT. Work on such extensions is underway and will be reported in future publications.

CHAPTER IV

Pulse Shape Discrimination in Organic Scintillator Materials: The Role of Intersystem Crossing

Contributions: Design of study; acquisition, analysis, and interpretation of data; drafting and revision of final version to be published.

4.1 Introduction

Organic materials have been used in the detection of ionizing radiation for more than 70 years,[40] as they possess properties that are desirable in a scintillator. Namely, they have a high light yield from the conversion of radiation, they undergo fast fluorescence (∼ns), and they are able to discriminate between types of ionizing radiation.[40] The ability of organic scintillators to discriminate between types of incident particles is based on differences that occur in the proportions of prompt and delayed fluorescence. This arises from the fact that the Compton scattering of gamma radiation and the proton recoil induced by neutron radiation have different excitation and ionization characteristics. When ions and electrons recombine there is a 75% chance they will produce a triplet excitation, which contributes to the delayed fluorescence via TTA. Thus, the different ionization characteristics are reflected in a greater proportion of delayed fluorescence observed in the case of neutron radiation.[40,41] This gives rise to characteristic pulse shapes based on the exponential decay

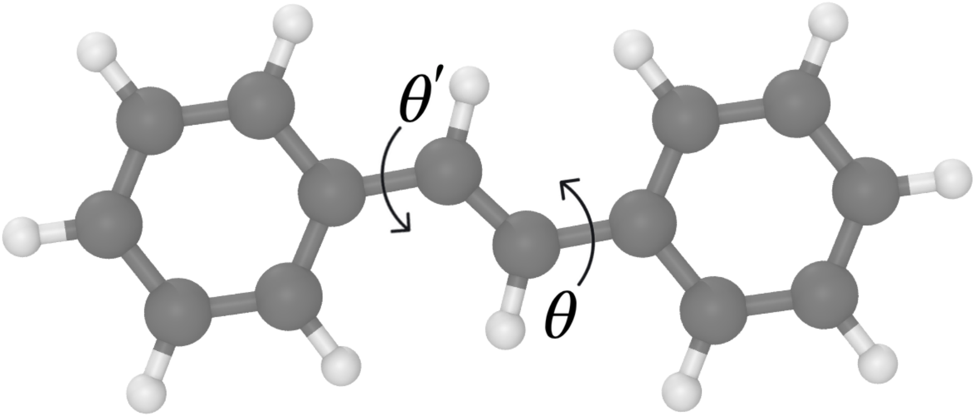

Figure 4.1: A *trans*–stilbene molecule. In the deuterated case all 12 hydrogens are replaced by deuterium (*trans*–stilbene–d_{12}).

of the fast (prompt) component and the non-exponential decay of the slow (delayed) component.[42] Deuteration has been shown to improve PSD in liquid organic scintillators[164–166] and more recently in single crystal *trans*–stilbene (shown in Figure 4.1),[44] one of the most common materials for PSD. This is illustrated in Figure 4.2, which compares the PSD figure of merit (FOM), a measure of the quality of PSD,[42,167] for protonated *trans*–stilbene, deuterated *trans*–stilbene, and p-terphenyl for reference. The observed improvement in PSD raises the question of what impact deuteration has on the underlying processes.

Luminescence in organic scintillators arises from a series of intra- and intermolecular processes, illustrated schematically in Figure 4.3:

1. Electronic excitation to S_n or T_n states via radiation, collision, or recombination
2. Internal conversion (IC) to S_1 or T_1 excited states (∼ps)
3. Prompt fluorescence from S_1 excited states (∼ns)
4. Delayed fluorescence via triplet migration and subsequent TTA (∼ns)

Any process that impacts the fraction of delayed to prompt fluorescence, and thereby the characteristic pulse shapes, will affect the ability of PSD. There are three such processes: ISC from the singlet S_1 state to a triplet T_n state, triplet migration through

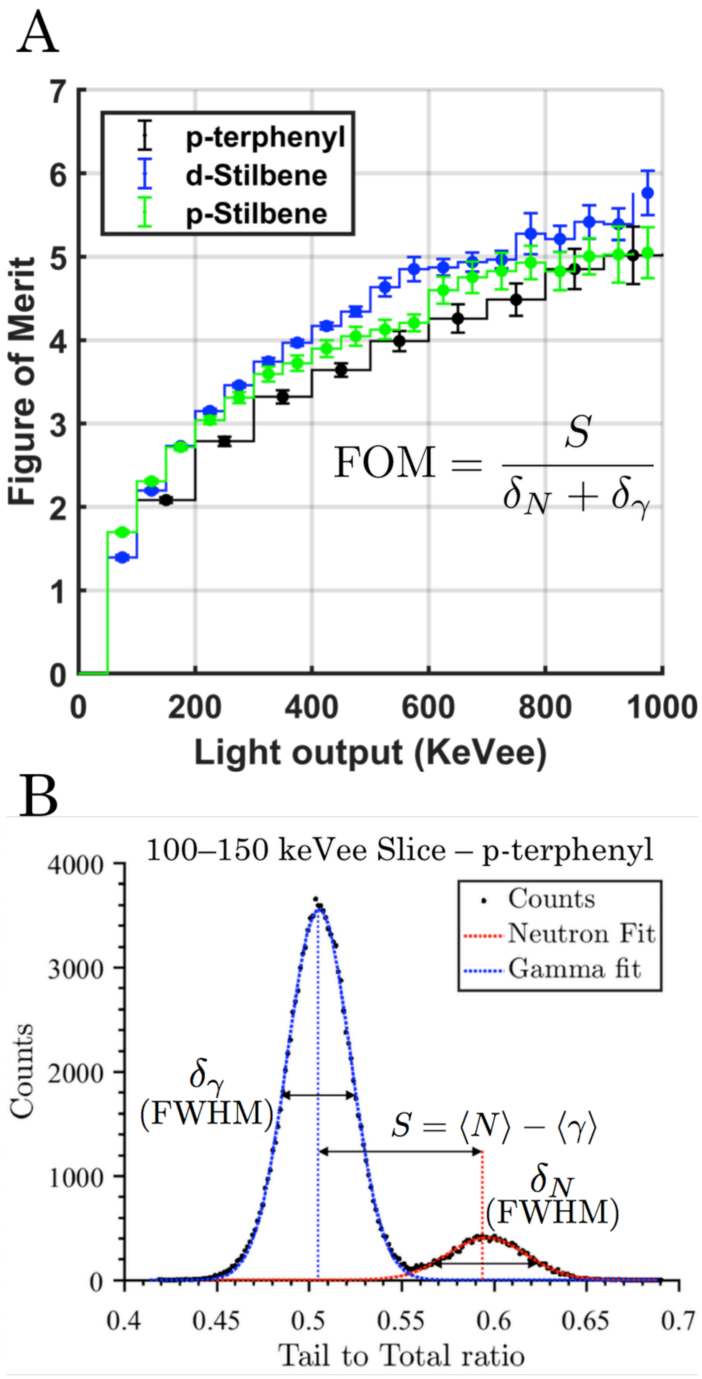

Figure 4.2: The PSD FOM as a function of light output (A) for p-terphenyl (black), deuterated *trans*–stilbene (blue), and protonated *trans*–stilbene (green). FOM is calculated according to the equation FOM= $S/(\delta_N+\delta_\gamma)$, in which δ_N and δ_γ are the full widths at half maximum (FWHM) for the neutron and gamma bands at a given light output (in keV$_{ee}$), respectively, and S is the separation between the bands. These parameters are illustrated in a sample slice of a PSD scatter plot (B) for p-terphenyl. Adapted from Reference 43.

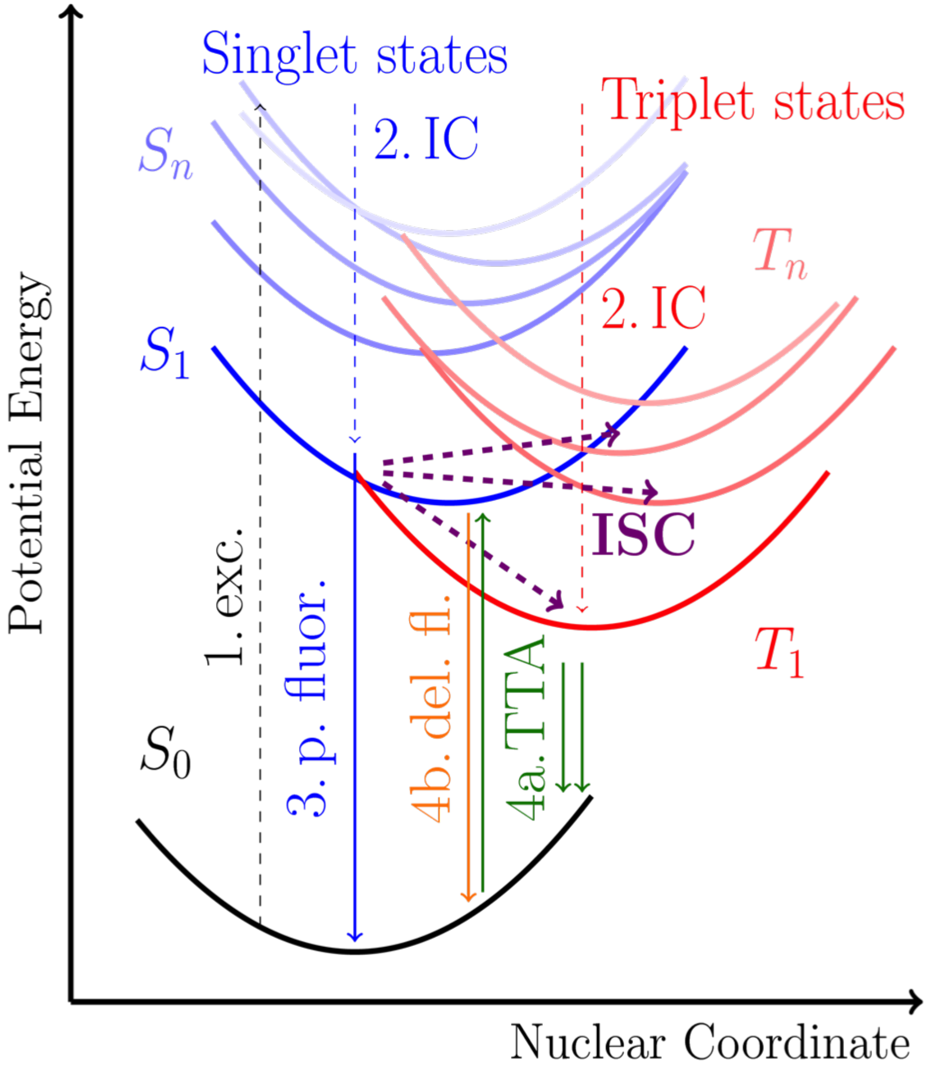

Figure 4.3: A schematic illustration of the series of intra- and intermolecular processes that give rise to light emission in organic scintillators. These include: (1) electronic excitation to S_n or T_n, (2) ultrafast internal conversion down to S_1 or T_1, (3) prompt fluorescence from S_1 to S_0, and (4) delayed fluorescence via triplet migration and subsequent triplet–triplet annihilation (TTA). Intersystem crossing from singlet to triplet states can impede pulse-shape discrimination, which is based on the temporal luminescence pattern of prompt fluorescence (from initially excited S_n states) and delayed fluorescence (from initially excited T_n states).

the material, and subsequent TTA between adjacent triplet states.[168] In this chapter we consider the case of ISC, which can increase (and thus distort) the fraction of delayed fluorescence if the ISC occurs on a timescale similar to the prompt fluorescence. We investigated the role of ISC in *trans*–stilbene by calculating rate constants for the singlet-to-triplet transitions ($\mathrm{S}_1 \rightarrow \mathrm{T}_n$). This was done using a fully quantum-mechanical equilibrium FGR approach.[101,105,124,169–175] In contrast to the more commonly used semi-classical Marcus theory,[102–104] the equilibrium FGR approach, detailed in Section 4.2.1, includes nuclear dynamics through the use of normal modes and HRFs, and thus is sensitive to isotope effects on the ISC rates. Marcus theory, however, relies entirely on electronic structure information and can not account for nuclear isotope effects. Thus, we were able to calculate the ISC rates of deuterated *trans*–stilbene–d_{12} ($\mathrm{C}_{14}\mathrm{D}_{12}$) and compare them to those of standard *trans*–stilbene ($\mathrm{C}_{14}\mathrm{H}_{12}$).

This chapter is organized as follows. The equilibrium FGR methodology for calculating ISC rate constants and the electronic structure calculations that were performed are described in Section 4.2. The results of these calculations are reported in Section 4.3. The conclusions are presented in Section 4.4.

4.2 Theory and Numerical Methods

4.2.1 Fermi's Golden Rule Transition Rates

We consider a system with an overall Hamiltonian described as follows

$$\hat{H} = \sum_{n=1}^{N} \Big[|\mathrm{T}_n\rangle(\hbar\tilde{\omega}_n + \hat{H}_{\mathrm{T}_n})\langle \mathrm{T}_n| + |\mathrm{T}_n\rangle V_{\mathrm{T}_n\mathrm{S}_1}\langle \mathrm{S}_1| + |\mathrm{S}_1\rangle V_{\mathrm{S}_1\mathrm{T}_n}\langle \mathrm{T}_n| \Big] + |\mathrm{S}_1\rangle \hat{H}_{\mathrm{S}_1}\langle \mathrm{S}_1| \tag{4.1}$$

Here, S_1 and T_n are the corresponding first excited singlet and first n excited triplet electronic states, $\tilde{\omega}_n$ is the energy of state T_n relative to that of state S_1 (with each in its respective equilibrium geometry), $V_{\mathrm{T}_n\mathrm{S}_1} = V_{\mathrm{S}_1\mathrm{T}_n} \in \Re$ is the electronic coupling coefficient for the S_1 and T_n states (assumed to be constant within the Condon approximation), and $\hat{H}_{\mathrm{S}_1}$ and $\hat{H}_{\mathrm{T}_n}$ are the nuclear Hamiltonians that correspond to each of the diabatic electronic states. The nuclear degrees of freedom can be described in terms of M independent normal modes

$$\hat{H}_{\mathrm{S}_1} = \sum_{\alpha=1}^{M} \left[\frac{\hat{p}_\alpha^2}{2} + \frac{\omega_\alpha^2}{2}(\hat{x}_\alpha - x_{\alpha,\mathrm{eq}}^{\mathrm{S}_1}) \right], \qquad \hat{H}_{\mathrm{T}_n} = \sum_{\alpha=1}^{M} \left[\frac{\hat{p}_\alpha^2}{2} + \frac{\omega_\alpha^2}{2}(\hat{x}_\alpha - x_{\alpha,\mathrm{eq}}^{\mathrm{T}_n}) \right] \tag{4.2}$$

in which $\hat{x}_\alpha$, $\hat{p}_\alpha$, and ω_α are the mass-weighted coordinates, momenta, and frequencies, respectively, of the corresponding modes, and $x_{\alpha,\mathrm{eq}}^{\mathrm{S}_1}$ and $x_{\alpha,\mathrm{eq}}^{\mathrm{T}_n}$ are the equilibrium geometries.

A fully quantum-mechanical equilibrium FGR rate constant for the electronic transition from $\mathrm{S}_1 \rightarrow \mathrm{T}_n$ can be obtained by making two assumptions: (1) that the system starts out in the S_1 state with the nuclear DOF at thermal equilibrium on the corresponding potential energy surface (PES), and (2) that the electronic coupling values, $|\mathrm{T}\rangle V_{\mathrm{T}_n\mathrm{S}_1} \langle \mathrm{S}|$ and $|\mathrm{S}\rangle V_{\mathrm{S}_1\mathrm{T}_n} \langle \mathrm{T}|$, are weak and can be treated as a small perturbation to H_{S_1} and H_{T_n}, respectively. The resulting equilibrium FGR rate constant is given by[91]

$$k_{\mathrm{FGR}}^{\mathrm{S}_1 \rightarrow \mathrm{T}_n} = \frac{|V_{\mathrm{S}_1\mathrm{T}_n}|^2}{\hbar^2} \int_{-\infty}^{\infty} \mathrm{d}t \, \mathrm{e}^{i\tilde{\omega}_n t} F_{\mathrm{intra}}(t) \tag{4.3}$$

If we assume that the PESs are harmonic and that the normal modes are independent of the electronic state, then the expression for $F_{\mathrm{intra}}(t)$ is[107,123,125–127]

$$F_{\mathrm{intra}}(t) = \exp\left[\sum_{\alpha=1}^{M} \left\{ -S_{\alpha,n}(2q_\alpha + 1) + S_{\alpha,n} \left[(q_\alpha + 1)\mathrm{e}^{-i\omega_\alpha t} + q_\alpha \mathrm{e}^{i\omega_\alpha t} \right] \right\} \right] \tag{4.4}$$

where $q_\alpha = \left[\mathrm{e}^{(\hbar\omega_\alpha / k_\mathrm{B} T)} - 1 \right]^{-1}$ is the normal mode occupancy at thermal equilibrium and $S_{\alpha,n}$ is the corresponding HRF,[176] given by

$$S_{\alpha,n} = \frac{\omega_\alpha}{2\hbar}(x^{\mathrm{S}_1}_{\alpha,\mathrm{eq}} - x^{\mathrm{T}_n}_{\alpha,\mathrm{eq}})^2 \tag{4.5}$$

This method is more general than the more common semi-classical Marcus theory, which can be obtained by combining the high-temperature limit, where $k_\mathrm{B}T \gg \hbar\omega_\alpha$ is assumed, and the short-time limit, where $F_\mathrm{intra}(t)$ is assumed to be short-lived.[91] Applying these approximations yields

$$k^{\mathrm{S}_1\to\mathrm{T}_n}_{\mathrm{Marcus}} = \frac{|V_{\mathrm{S}_1\mathrm{T}_n}|^2}{\hbar}\sqrt{\frac{\pi}{k_\mathrm{B}TE_\mathrm{r}}}\exp\left[-\frac{(\hbar\tilde{\omega}_n - E_\mathrm{r})^2}{4k_\mathrm{B}TE_\mathrm{r}}\right] \tag{4.6}$$

where E_r represents the reorganization energy and $(\hbar\tilde{\omega}_\alpha - E_\mathrm{r})^2/4E_r$ represents the activation energy. The underlying assumptions can be questionable, particularly in the inverted region where increased overlap of nuclear wavefunctions occurs,[105,177,178] so we examine whether they are justified for the case of ISC in *trans*–stilbene. Regardless of its validity, Marcus theory does not account for nuclear dynamics and thus cannot be used to examine isotope effects.

4.2.2 Electronic Structure Calculations

Geometry optimization was performed using DFT in the 6-311G(d,p) basis set[84] with the ωB97X–D RSH functional[82,83] on a single *trans*–stilbene molecule (monomer), with the conductor-like polarizable continuum model (C–PCM)[179–181] used to account for the surrounding crystal environment. Unless explicitly stated otherwise, excited state calculations were performed using TDDFT in the 6-311++G(d,p) basis set[182] with the ωPBE functional,[183] which was optimally tuned using the OT–SRSH–PCM method (refer to Section 1.2.2).[62,65,70] A dielectric constant of 2.4034 was calculated for *trans*-stilbene using the Clausius–Mossotti equation.[35,66] Spin–orbit coupling (SOC) constants between the S_1 and T_n states were calculated via the one-electron Breit Pauli spin–orbit Hamiltonian method.[184] Vibrational normal modes were calculated using the ωB97X–D functional for both the ground state, S_0, and the S_1 excited state. All electronic structure calculations were performed with the Q-Chem 4.4 software package.[85]

4.3 Results and Discussion

ISC rate constants were calculated using the equilibrium FGR approach for transitions from the S_1 state to the four lowest-energy triplet states, T_1–T_4, in *trans*–stilbene, as higher-level triplet states yield prohibitively large energy gaps. TDDFT calculations were performed with the ωPBE functional tuned using the OT–SRSH–PCM method, hereafter referred to as the ωPBE–SRSH functional, as well as the ωB97X–D RSH and B3LYP hybrid functionals[33,34,82,83] for comparison. We describe the FGR method in greater detail in the next section (4.3.1) and discuss the performance of the different functionals. The FGR rates were also calculated in the high-temperature and short-time limits in order to assess the validity of Marcus theory for this system, with Marcus rates discussed in Section 4.3.2. We additionally investigated the impact that the dihedral angle θ displayed in Figure 4.1, for which gas-phase calculations have previously shown a fairly shallow PES,[185–188] has on ISC rates (Section 4.3.3). Finally, in Section 4.3.4, we examine isotope effects for the case of deuterated *trans*–stilbene–d_{12}.

4.3.1 Comparison of Hybrid Functionals

The results obtained using the three different functionals (ωPBE–SRSH, ωB97X–D, and B3LYP) are displayed in Table 4.1, which include the FGR rate constants (k_{FGR}), the SOCs (V_{SOC}), the energy gaps between S_1 and T_n ($\Delta E_{S_1T_n}$), the reorganization energies calculated directly from the difference between the S_1 energy at the S_1 and T_n geometries (E_r^{direct}), and the reorganization energies calculated from the HRFs (E_r^{HRF}) according to $E_r^{\text{HRF}} = \sum_{\alpha}^{M} \hbar\omega_\alpha S_{\alpha,n}$. The two RSH functionals yield good agreement between SOCs and energies, with the only notable difference being a nearly twofold increase in the S_1–T_2 energy gap with ωB97X–D (0.0824 eV compared to 0.0456 eV). The B3LYP SOCs also agree fairly well with the RSH functionals, but there are some notable differences in the energies. The S_1–T_2 energy gap is significantly larger at 0.1591 eV, and we also see significant differences in the reorganization energies for the T_2 and T_3 cases. Given the good agreement between ωPBE–SRSH and the well-established ωB97X–D, all further discussion will refer to values obtained using the ωPBE–SRSH functional, unless otherwise noted.

ωPBE–SRSH Functional

	k_{FGR} [s^{-1}]	V_{SOC} [cm^{-1}]	$\Delta E_{\text{S}_1\text{T}_n}$ [eV]	E_r^{direct} [eV]
$\text{S}_1 \rightarrow \text{T}_1$	1.2×10^4	0.0977	-1.5787	0.0478
$\text{S}_1 \rightarrow \text{T}_2$	7.2×10^3	0.0074	0.0456	0.2284
$\text{S}_1 \rightarrow \text{T}_3$	7.7×10^6	1.3496	0.4454	0.5060
$\text{S}_1 \rightarrow \text{T}_4$	1.1×10^0	0.0005	0.6449	0.2963

ωB97X–D Functional

	k_{FGR} [s^{-1}]	V_{SOC} [cm^{-1}]	$\Delta E_{\text{S}_1\text{T}_n}$ [eV]	E_r^{direct} [eV]	E_r^{HRF} [eV]
$\text{S}_1 \rightarrow \text{T}_1$	1.0×10^4	0.0858	-1.5284	0.0362	0.0413
$\text{S}_1 \rightarrow \text{T}_2$	3.4×10^3	0.0064	0.0824	0.2507	0.2534
$\text{S}_1 \rightarrow \text{T}_3$	6.2×10^6	1.2899	0.4942	0.5300	0.5535
$\text{S}_1 \rightarrow \text{T}_4$	1.3×10^0	0.0006	0.7005	0.3165	0.3283

B3LYP Functional

	k_{FGR} [s^{-1}]	V_{SOC} [cm^{-1}]	$\Delta E_{\text{S}_1\text{T}_n}$ [eV]	E_r^{direct} [eV]	E_r^{HRF} [eV]
$\text{S}_1 \rightarrow \text{T}_1$	2.0×10^4	0.1086	-1.4291	0.0438	0.0620
$\text{S}_1 \rightarrow \text{T}_2$	2.1×10^3	0.0063	0.1591	0.1540	0.1690
$\text{S}_1 \rightarrow \text{T}_3$	2.5×10^7	1.3696	0.3937	0.1284	0.1276
$\text{S}_1 \rightarrow \text{T}_4$	9.1×10^{-1}	0.0005	0.7416	0.2518	0.2777

Table 4.1: FGR rate constants (k_{FGR}), spin-orbit couplings (V_{SOC}), energy gaps ($\Delta E_{\text{S}_1 T_n}$), directly-calculated reorganization energies (E_r^{dir}), and HRF-calculated reorganization energies (E_r^{HRF}) for the $\text{S}_1 \rightarrow \text{T}_n$ transitions in *trans*–stilbene, calculated using the ωPBE–SRSH, ωB97X–D, and B3LYP functionals.

$F_{\text{intra}}(t)$ and the corresponding HRFs for the $\text{S}_1 \rightarrow \text{T}_3$ transition are shown in Figure 4.4. This illustrates the need to apply an exponential damping factor in order to eliminate recurrences in the integrand. While the harmonic approximation is known to perform poorly for calculating IR spectra,[189] it can be justified in rate calculations by the close agreement of the reorganization energies. The reorganization energies calculated directly from the TDDFT energies in Table 4.1 agree very well with those obtained via the HRFs within the harmonic approximation, differing by at most only about 15%. Equilibrium FGR yields ISC rates that agree reasonably when using the three different functionals, with the differences largely explained by the energetics. The $S_1 \rightarrow T_3$ transition clearly occurs at the fastest rate, with a rate constant of 7.7×10^6 s^{-1} in the case of ωPBE–SRSH. This corresponds to a time constant of 130 ns, whereas prompt fluorescence in *trans*–stilbene occurs on a timescale of about 3.4 ns,[190] indicating that ISC is too slow to significantly affect PSD in *trans*–stilbene.

4.3.2 Equilibrium FGR versus Marcus Theory

	k_{FGR} [s^{-1}]	k_{Marcus} [s^{-1}]
$S_1 \rightarrow T_1$	1.2×10^4	~ 0
$S_1 \rightarrow T_2$	7.2×10^3	8.9×10^2
$S_1 \rightarrow T_3$	7.7×10^6	1.4×10^1
$S_1 \rightarrow T_4$	1.1×10^0	6.7×10^{-11}

Table 4.2: Comparison of rate constants calculated using equilibrium FGR (k_{FGR}) and Marcus theory (k_{Marcus}) with the ωPBE–SRSH functional.

FGR rate constants were calculated in the high-temperature and short-time limits to obtain the equivalent Marcus rates, which are shown in Table 4.2. Marcus theory is clearly invalid for *trans*–stilbene, yielding rate constants that are significantly smaller than those calculated the FGR approach. In the best case, $S_1 \rightarrow T_2$, k_{Marcus} is an order of magnitude smaller. Looking at Figure 4.4, we can see that the correlation function $F_{\mathrm{intra}}(t)$ is short-lived, and therefore the short-time approximation seems to be reasonable. However, the HRFs plot clearly shows that the greatest contribution occurs from a high frequency mode ($\sim$1700 cm^{-1}), and therefore the high-temperature

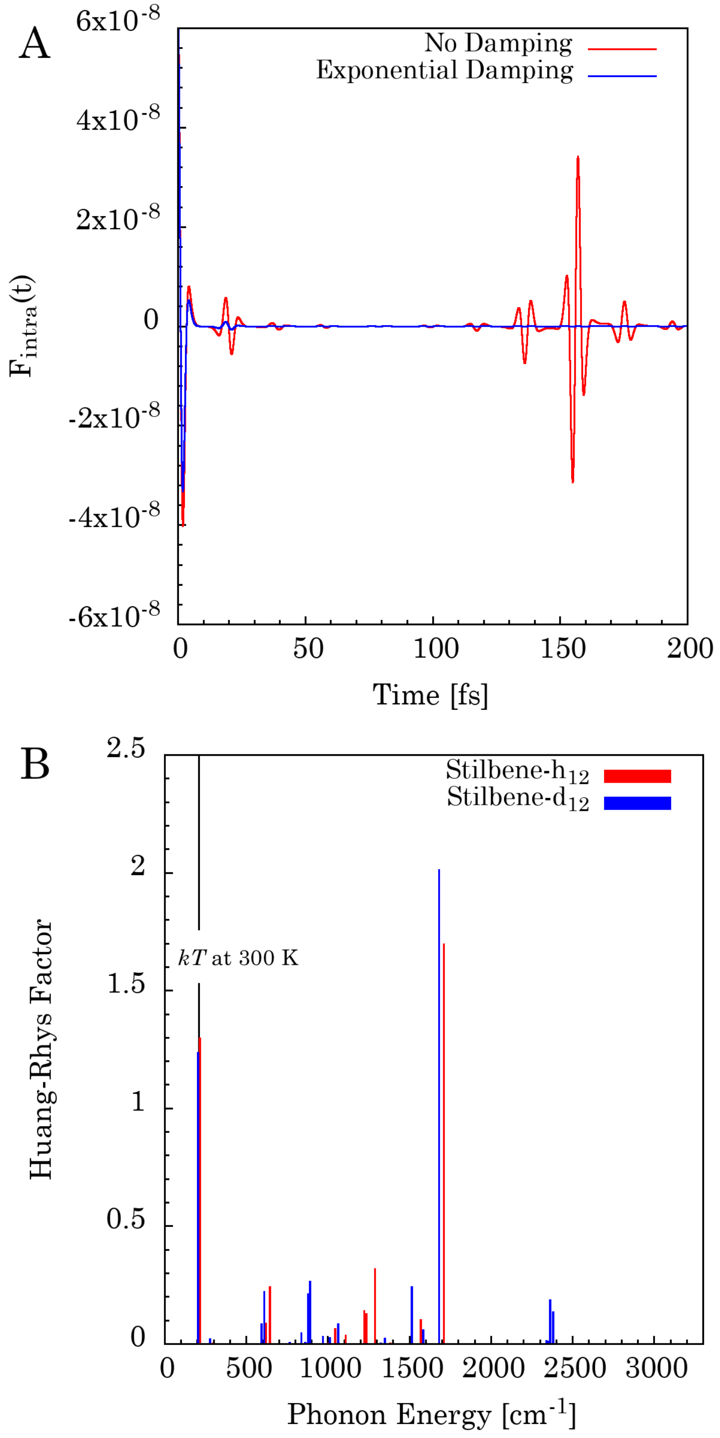

Figure 4.4: Analysis of the equilibrium FGR approach for the $S_1 \rightarrow T_3$ transition showcasing (A) $F_{\text{intra}}(t)$ with (red) and without (blue) exponential damping applied (10 fs decay constant), and (B) the HRFs for protonated *trans*–stilbene-h_{12} (red) and deuterated *trans*–stilbene–d_{12} (blue).

approximation, $k_{\mathrm{B}}T \gg \hbar\omega_\alpha$, is violated. In the case of $\mathrm{S}_1 \to \mathrm{T}_1$, where k^{Marcus} is essentially zero, T_1 is significantly lower in energy than S_1 and we can therefore expect it to be far into the inverted region, where Marcus is known to perform poorly. In a case where ISC is indeed fast enough to compete with PSD, relying on Marcus theory might lead one to conclude otherwise.

4.3.3 Structural Effects

While all of the excited state energies were found to be minimized in planar conformations, in most cases we also found local minima for geometries with distorted dihedral angles (θ in Figure 4.1), indicating double-well PESs. The optimized nonplanar dihedral angles for each state are shown in Table 4.3, along with the energies and SOCs relative those of the optimized planar cases. Most of the angles range from about 17–21°, with the exceptions being S_1, 9.2°, and T1, which did not have a nonplanar minimum, while the energies for the nonplanar geometries only differ from those of the planar geometries by about 0.02–0.03 eV. The SOCs, however, are significantly stronger for the $\mathrm{S}_1 \to \mathrm{T}_2$ and $\mathrm{S}_1 \to \mathrm{T}_4$ transitions, which would have a significant impact on the transition rates. While this is notable, experimental evidence suggests that the dihedral angle in crystalline *trans*–stilbene is sterically hindered to a range of about 0–7°,[191–195] so we limit further consideration to that range.

	Optimized Nonplanar			Fixed 7° Dihedral		
	θ [°]	δE [eV]	$\delta V_{\mathrm{SOC}}^{\mathrm{S}_1\to\mathrm{T}_n}$ [cm^{-1}]	δE [eV]	$\delta V_{\mathrm{SOC}}^{\mathrm{S}_1\to\mathrm{T}_n}$ [cm^{-1}]	$k_{\mathrm{FGR}}^{\mathrm{S}_1\to\mathrm{T}_n}$ [s^{-1}]
S_0	20.8	0.0018	—	11.842	—	—
S_1	9.2	0.0310	—	8.286	—	—
T_1	0	—	0.0756	10.060	0.0098	1.5×10^4
T_2	17.9	0.0209	0.5066	8.143	0.2914	1.4×10^7
T_3	17.2	0.0201	-0.0897	7.750	0.0084	8.0×10^6
T_4	17.8	0.0243	1.4687	7.653	0.3276	4.3×10^5

Table 4.3: Dihedral angles (θ), relative energies (δE), relative SOCs ($\delta V_{\mathrm{SOC}}^{\mathrm{S}_1\to\mathrm{T}_n}$), and FGR rate constants ($k_{\mathrm{FGR}}^{\mathrm{S}_1\to\mathrm{T}_n}$) for the optimized nonplanar and fixed 7° dihedral *trans*–stilbene geometries. Energies and SOCs are relative to those of the optimized planar geometries.

The relative energies and SOCs for a fixed 7° dihedral angle are also shown in Table 4.3, as well as the FGR rate constants calculated for this case. The energies are significantly higher than in the planar case, by about 8 eV for the excited states, suggesting that *trans*–stilbene likely remains close to planar. This is in contrast to previous gas-phase calculations suggesting a relatively flat PES.[185–188] Nevertheless, the SOCs for the case of a 7° dihedral angle are also significantly stronger for the $S_1 \rightarrow T_2$ and $S_1 \rightarrow T_4$ transitions, though less than with the larger dihedral angles of the optimized nonplanar case. We calculated the transition rate constants for the 7° dihedral geometries using the planar S_1 normal modes, and as expected they increase significantly for the $S_1 \rightarrow T_2$ and $S_1 \rightarrow T_4$ transitions (1.4×10^7 s^{-1} and 4.3×10^5 s^{-1}, respectively). However, even under these extreme conditions, the fastest rate constant of 1.4×10^7 s^{-1}, with a corresponding time constant of 70 ns, is still too slow to compete with prompt fluorescence (3.4 ns).[190]

4.3.4 Isotope Effects

The observed PSD improvement through deuteration initially led to the hypothesis that the expected isotope effect on ISC rates could be a major contributing factor to this enhancement. However, the analysis in Sections 4.3.1 and 4.3.3 has already shown that, overall, ISC seems to play a negligible role for the PSD efficiency of *trans*–stilbene. Yet, for the sake of completeness, we calculated FGR rate constants for each transition in the deuterated system and compare them to those of standard hydrogenated stilbene. Results are shown in Table 4.4, along with the reorganization energies calculated from the HRFs. The rate constants are about 20–30% smaller in the deuterated case for all of the transitions except $S_1 \rightarrow T_1$, which is about 8% larger. This indicates that ISC is slower in stilbene–d_{12}, and thus even less likely to interfere with PSD. The impact of deuteration on the HRFs for the $S_1 \rightarrow T_3$ transition is shown in Figure 4.4. Deuteration leads to increased reorganization energies calculated from the HRFs, which should ideally be unaffected by deuterium. This likely contributes in part to the differences observed in the rate constants.

	Stilbene–h_{12}		Stilbene–d_{12}	
	k_{FGR} [s^{-1}]	E_r^{HRF} [eV]	k_{FGR} [s^{-1}]	E_r^{HRF} [eV]
$S_1 \rightarrow T_1$	1.2×10^4	0.0413	1.3×10^4	0.0541
$S_1 \rightarrow T_2$	7.2×10^3	0.2534	5.1×10^3	0.3399
$S_1 \rightarrow T_3$	7.7×10^6	0.5535	5.8×10^6	0.7214
$S_1 \rightarrow T_4$	1.1×10^0	0.3283	0.9×10^0	0.4222

Table 4.4: Comparison of FGR rate constants (k_{FGR}) and HRF-calculated reorganization energies (E_r^{HRF}) for hydrogenated and deuterated *trans*–stilbene.

4.4 Conclusions

Based on the calculated rate constants, ISC does not seem to compete with prompt fluorescence in *trans*–stilbene. The ISC rates depend on the structure, significantly increasing in most cases with larger dihedral angles. In fact, double-well potentials are found, with local minima at larger angles (17–21° in most cases) that are only 0.02–0.03 eV higher than in the planar geometries. However, given steric restrictions in the crystal structure and a relatively large energy barrier, *trans*–stilbene likely remains in a near-planar conformation. At a dihedral angle of 7°, the greatest distortion reported in the crystal,[191–195] the fastest ISC rates are still one to two orders of magnitude slower than the prompt fluorescence and are therefore expected to play a negligible role in PSD. Even so, deuteration can reduce the ISC rate constants by as much as 30%, and therefore further suppresses the threat to prompt fluorescence.

Further investigation into the other two processes that play a role in PSD, triplet migration and TTA, will be based on a dimer model. The monomer-based model presented in this chapter indicates a retarding effect on ISC by deuteration. If this effect persists in the cases of triplet migration and TTA, it would lead to deceleration of delayed fluorescence and thereby increase PSD ability. This would explain the improved PSD observed experimentally in *trans*–stilbene–d_{12}. Calculations are currently underway, but are not included as part of this study and will be published elsewhere.

CHAPTER V

Compute-to-Learn: Authentic Learning via Development of Interactive Computer Demonstrations within a Peer-Led Studio Environment

Contributions: Conception and design of study; acquisition, analysis, and interpretation of data; drafting and revision of final version to be published.

Reproduced with permission from Jafari, M.; Welden, A. R.; Williams, K. L.; Winograd, B.; Mulvihill, E.; Hendrickson, H. P.; Lenard, M.; Gottfried, A.; Geva, E. *J. Chem. Educ.* **2017**, *94*, 1896-1903. Copyright 2017 American Chemical Society.

5.1 Introduction

Learning is widely acknowledged as being situational,[196–200] meaning it is inherently dependent upon the environment in which it occurs. “Where” and “how” something is learned is just as important as “what” is learned, because knowledge is dependent on the context in which it was developed and applied. Within this framework of situated cognition, instructors can provide students with opportunities to reconstruct a concept for themselves through engagement in activities that are typical of the discipline’s practices,[201] thus providing a more meaningful and authentic learning environment.[202,203] This can be accomplished via the use of real-world problems that are investigated in a collaborative environment over a sustained period of time.[204] It can be difficult to incorporate such authentic learning activities into the traditional lecture-based undergraduate classroom, which is often explanatory in nature and relies on activities structured around established knowledge, generally in an environment that is not conducive to collaboration. In an effort to address these issues in the physical sciences we have developed a compute-to-learn pedagogy, which incorporates important features of scholarly research into a collaborative studio environment for undergraduate students.

The compute-to-learn pedagogy was developed as an extension and expansion of the writing-to-teach pedagogy of Vázquez et al.,[205] which focused on utilizing explanatory writing and peer learning activities to engage students in authentic and meaningful learning, and on creation of textbook-like sections that could be utilized by future students in the course as learning resources. While writing-to-teach effectively enhanced students' ability to generate explanations of scientific concepts, incorporating the textbook-like sections written by the students was not straightforward due to the likelihood of misstatements and misinformation. Furthermore, reviewing the documents written by students for accuracy, providing feedback, and repeating this cycle to achieve a correct description of the physical concept was a time-consuming and cumbersome process. Due to the time commitment of reviewing said documents, the writing-to-teach pedagogy could only be applied to small groups of students.

The compute-to-learn pedagogy follows a guided inquiry approach,[206,207] in which students design and develop an interactive, computer-based demonstration that illustrates a physical chemistry concept of their choice. Students work on this semester-long project in a studio environment that borrows elements from the arts, where students work in a studio and receive feedback from one another regarding their artistic creations.[205,208,209] The pedagogy focuses on active learning strategies and encourages cooperation and collaboration among peers,[210,211] with undergraduate peer leaders and graduate student instructors (GSIs) serving as mentors. Students investigate a challenging, open-ended physical chemistry concept rather than a well-defined problem, similar to a researcher in a scientific discipline. After they have completed a computer-programming tutorial and studied their topic, students design an interactive, visual representation that they present to their peers for review in a storyboard process. The students proceed to develop their demonstrations using the programming skills obtained during the tutorial. Utilizing feedback from several cycles of development and peer review, students continue to program and refine their demonstrations. Finally, students submit their work to the Wolfram Demonstrations Project,[212] an open source library of interactive demonstrations from a variety of fields, for external review and publication. Thus students incorporate physical chemistry concepts into teaching tools that could be utilized by others.

This framework preserves the advantageous components of writing-to-teach, such as enhancing the ability of students to generate explanations of scientific concepts, and overcomes the cumbersome review process of writing-to-teach. The introduction of computer programming into the pedagogy of compute-to-learn corresponds to an additional benefit for students who are interested in acquiring that skill. The compute-to-learn pedagogy immerses students in a research environment that closely simulates the real-world scientific research process, and thus helps to apprentice students as members of the scientific community.[198,201] Through the process of creating the demonstration, students learn new concepts in physical chemistry, mathematics, writing, and programming and are given the opportunity to hone various skills, such as communication, collaboration, and task management.

This chapter is organized as follows. In the next (second) section, we present our first implementation of the compute-to-learn pedagogy and reflect on the shortcomings that we found. In the third section, we provide an overview of why we utilized Wolfram Mathematica[87] to develop the demonstrations and provide an example of a demonstration developed in the studio. In the fourth section, we detail the modifications we made in subsequent iterations of the compute-to-learn studio and the motivations behind these improvements. In the fifth section, we discuss assessment of the compute-to-learn pedagogy on student learning utilizing interviews of participants from the Fall 2016 and Winter 2017 semesters.

5.2 Initial Implementation of Compute-to-Learn

Compute-to-learn[213] was first implemented at the University of Michigan in the 13-week-long Fall semester of 2015 as the Honors option affiliated with the "Chemical Principles" (CHEM 260) course. CHEM 260 provides a survey of quantum mechanics, thermodynamics, and kinetics. It serves as an introductory physical chemistry course in place of a second-semester general chemistry course for those students majoring in chemistry or biochemistry. Students could take the course for honors credit (CHEM 260H) by participating in the compute-to-learn studio, which included additional weekly two-hour meetings. This option was available to all students enrolled in the primary course. Of the sixty students that were enrolled in CHEM 260 during the Fall 2015 semester, six students chose to participate in the compute-to-learn studio. This subset of six students met for twelve weekly two-hour studio sessions. During those sessions the students learned to program in Mathematica, design and create an interactive visualization of a physical chemistry concept, and prepare their work for publication.

A team consisting of faculty members, graduate students, and a pair of undergraduate peer leaders met regularly throughout the semester to develop course materials, review progress of students, and prepare for studio sessions. The undergraduate peer leaders served as advisors during the studio sessions and were the primary source of guidance for the students, while two GSIs were also present during the sessions to assist the peer leaders when necessary. The weekly meeting schedule for the Fall 2015 studio is shown in Table 5.1.

Compute-to-learn was designed with the expectation that students would have no prior experience with Wolfram Mathematica or computer programming in general. To this end, we designed a four-week tutorial to introduce students to the Wolfram Language. The tutorial focuses on core Wolfram syntax, with an emphasis on components of the language that are necessary for developing interactive Mathematica demonstrations. A detailed description of Mathematica demonstrations is provided in the next section. Scaffolding was incorporated into the tutorial to provide initial support to students, and is systematically removed as they progress through it.[214,215] While the peer leaders guided students through the tutorial in the studio, the tutorial itself is entirely self-contained and was designed to make it possible for one to complete it with minimal supervision. To keep students engaged in the tutorial, they were given short homework assignments after each session and were encouraged to collaborate with peers on these programming exercises as they completed the tutorial.

Along with small, practical coding assignments, students were provided with a number of what we refer to as "prompts", which were meant to serve as open-ended introductions to scientific concepts that they could potentially use in their visualizations. This is similar to how a research mentor would pitch a research idea to an incoming graduate student. Each prompt included the following: background information about a physical chemistry concept, resources to find more information about that topic, and a few open-ended questions to help the students think about how they might want to design their demonstration. The prompts were based on concepts from thermodynamics, such as heat flow, heat capacities, heat engines, ideal solutions, and redox reactions. Students were asked to read the prompts or brainstorm other physical chemistry concepts of interest and then select and research a topic for

Week	Agenda	Review	Assignment
1-3	Engage in an interactive tutorial to learn essential Mathematica programming skills; Choose and research a scientific concept for demonstration	No	Research prompt topic; Implement new features into existing demonstration; Prepare storyboard
4	Complete tutorial; Present "storyboard" depiction of demonstration	Peer Review	Start programming demonstration
5	Fall Break – No Classes	No	Continue programming
6-8	Program demonstration in Mathematica	No	Continue programming
9	Informally present progress; Receive feedback from peers	Peer Review	Continue programming; Complete Wolfram Demonstration page's publication checklist
10	Modify demonstration to incorporate peer input; Write succinct one paragraph description	No	Continue programming; Complete final edits
11	Submit to Wolfram Demonstration Project for further review and publication	External Review by Wolfram	Write one-page reflection on peer review process
12	Incorporate edits offered by the Wolfram Mathematica reviewers	External Review by Wolfram	Incorporate external review edits into demonstrations

Table 5.1: Schedule of studio activities and assignments.

their project. Each student was tasked with creating a storyboard visualization of his or her Mathematica demonstration, to be used as a guide for completing the project. These storyboards were presented to the class as part of a peer review process, during which the other students, peer leaders, and GSIs were free to ask questions and make suggestions.

Following the storyboarding process, students began a three-week period of programming their demonstrations. They were encouraged to work collaboratively to solve any programming or design problems, with the peer leaders and graduate students available to provide guidance and advice as necessary. After completing the first three weeks of programming, students presented drafts of their Mathematica demonstrations to the rest of the class in a second peer review session. During this second peer review, students were required to discuss how the input from the previous peer review session impacted the development of their demonstrations. Following this session, students had an additional one to two weeks to implement any changes deemed necessary from the review session and to finish programming their demonstrations. At the end of the semester, students were asked to submit a brief paragraph describing their Mathematica demonstration. After the descriptive paragraph was reviewed by peer leaders and edited by students, the demonstrations were submitted to the Wolfram Demonstration Project to undergo official review. Finally, students were asked to submit a one-page reflection describing how they dealt with the comments given in each peer review process.

By the final week of the inaugural semester of the compute-to-learn studio, every student submitted their individually coded Mathematica demonstration to the Wolfram Demonstrations website for a total of six submitted demonstrations; however, only one of the six demonstrations was published. Students received official review from the Wolfram Demonstrations Project at or after the end of the semester. This made it difficult to continue working with the students to address reviewer comments and incorporate requested changes to complete the publication process. This was clearly a problem that we needed to address in future iterations of the compute-to-learn studio, in order to provide a more complete research experience. We discuss the implementation of these and other changes made in two subsequent iterations of the studio later in this article.

5.3 Mathematica Demonstrations

Wolfram Mathematica is a powerful computing environment commonly used in academia, industry, and education.[216] It was chosen as the development tool for the compute-to-learn studio primarily based on its fairly straightforward syntax, availability of tools for creating interactive demonstrations, and the existence of the Wolfram Demonstrations Project, which is a peer-reviewed, open-source web catalog of interactive demonstrations that provides students with a platform for publishing their newly created demonstrations. Students can also take advantage of the existing catalog of 10,000+ demonstrations to survey the capabilities of Mathematica and adopt ideas for their own visualizations, similar to how researchers can review and be inspired by the scientific literature.

The user does not need to have any knowledge of programming in order to interact with the dynamic output of Mathematica, which generally consists of graphics, sliders, and simple button presses. Creating an original demonstration from the ground up, however, requires a basic understanding of the Wolfram Language used in Mathematica, so this is taught in the first few weeks of the studio using the tutorial developed by our team. The code for many published demonstrations is short and concise, making construction of a demonstration an achievable goal in a single semester. Additionally, the external review process of the Wolfram Demonstrations Project serves to simulate the real-world peer review process involved in publishing a paper in a peer-reviewed scientific journal, thus contributing to an authentic research

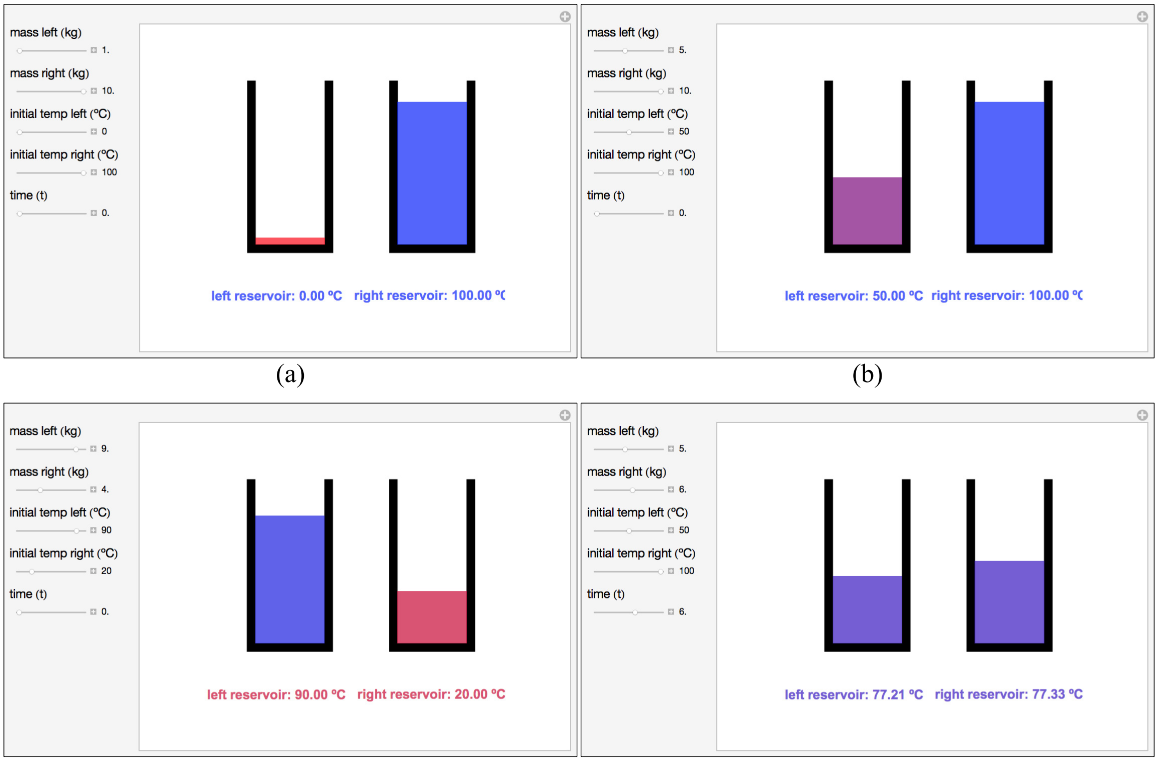
mass left (kg) 1.
mass right (kg) 10.
initial temp left (°C) 0
initial temp right (°C) 100
time (t) 0.
left reservoir: 0.00 °C right reservoir: 100.00 °

(a)

mass left (kg) 5.
mass right (kg) 10.
initial temp left (°C) 50
initial temp right (°C) 100
time (t) 0.
left reservoir: 50.00 °C right reservoir: 100.00 °

(b)

mass left (kg) 9.
mass right (kg) 4.
initial temp left (°C) 90
initial temp right (°C) 20
time (t) 0.
left reservoir: 90.00 °C right reservoir: 20.00 °C

(c)

mass left (kg) 5.
mass right (kg) 6.
initial temp left (°C) 50
initial temp right (°C) 100
time (t) 6.
left reservoir: 77.21 °C right reservoir: 77.33 °C

(d)

Figure 5.1: Snapshots of a Mathematica demonstration illustrating heat flow between two reservoirs of water. There are two sets of sliders for mass and temperature of each reservoir, which are varied between snapshots (a), (b), and (c). Adjusting the slider for time will update the temperatures of the reservoirs until equilibrium has been reached, as has nearly been achieved in snapshot (d). This demonstration is available on the Wolfram Demonstrations Project webpage.[217]

experience for the students.

An example of a Mathematica demonstration and the corresponding code are shown in Figure 5.1 and Figure 5.2, respectively, and can be found on the Wolfram Demonstration Project webpage.[217] This particular example was developed by a student who participated in CHEM 260H in the Fall of 2015. It demonstrates heat flow between a hot and a cold vessel, each containing water. The user is able to interact with the sliders to vary the mass and temperature of both the hot and cold reservoirs, while the visual demonstration calculates the equilibrium temperature in real time. Additionally, there is a slider to show how the system approaches equilibrium with

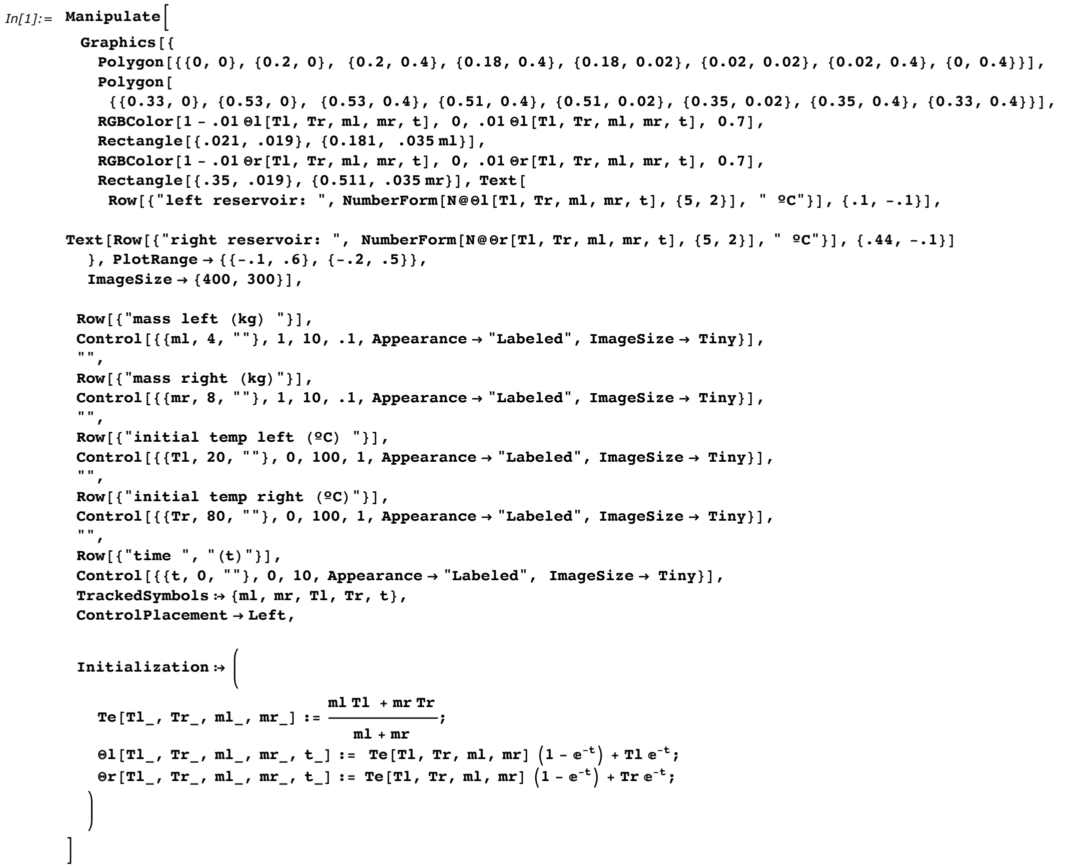

```
In[1]:= Manipulate[
         Graphics[{
           Polygon[{{0, 0}, {0.2, 0}, {0.2, 0.4}, {0.18, 0.4}, {0.18, 0.02}, {0.02, 0.02}, {0.02, 0.4}, {0, 0.4}}],
           Polygon[
            {{0.33, 0}, {0.53, 0}, {0.53, 0.4}, {0.51, 0.4}, {0.51, 0.02}, {0.35, 0.02}, {0.35, 0.4}, {0.33, 0.4}}],
           RGBColor[1 - .01 Θl[Tl, Tr, ml, mr, t], 0, .01 Θl[Tl, Tr, ml, mr, t], 0.7],
           Rectangle[{.021, .019}, {0.181, .035 ml}],
           RGBColor[1 - .01 Θr[Tl, Tr, ml, mr, t], 0, .01 Θr[Tl, Tr, ml, mr, t], 0.7],
           Rectangle[{.35, .019}, {0.511, .035 mr}], Text[
            Row[{"left reservoir: ", NumberForm[N@Θl[Tl, Tr, ml, mr, t], {5, 2}], " ºC"}], {.1, -.1}],

        Text[Row[{"right reservoir: ", NumberForm[N@Θr[Tl, Tr, ml, mr, t], {5, 2}], " ºC"}], {.44, -.1}]
          }, PlotRange → {{-.1, .6}, {-.2, .5}},
          ImageSize → {400, 300}],

         Row[{"mass left (kg) "}],
         Control[{{ml, 4, ""}, 1, 10, .1, Appearance → "Labeled", ImageSize → Tiny}],
         "",
         Row[{"mass right (kg)"}],
         Control[{{mr, 8, ""}, 1, 10, .1, Appearance → "Labeled", ImageSize → Tiny}],
         "",
         Row[{"initial temp left (ºC) "}],
         Control[{{Tl, 20, ""}, 0, 100, 1, Appearance → "Labeled", ImageSize → Tiny}],
         "",
         Row[{"initial temp right (ºC)"}],
         Control[{{Tr, 80, ""}, 0, 100, 1, Appearance → "Labeled", ImageSize → Tiny}],
         "",
         Row[{"time ", "(t)"}],
         Control[{{t, 0, ""}, 0, 10, Appearance → "Labeled", ImageSize → Tiny}],
         TrackedSymbols :→ {ml, mr, Tl, Tr, t},
         ControlPlacement → Left,

         Initialization :→ (

                                       ml Tl  + mr Tr
           Te[Tl_, Tr_, ml_, mr_] := ───────────────;
                                          ml + mr
           Θl[Tl_, Tr_, ml_, mr_, t_] :=  Te[Tl, Tr, ml, mr] (1 - ⅇ^-t) + Tl ⅇ^-t;
           Θr[Tl_, Tr_, ml_, mr_, t_] := Te[Tl, Tr, ml, mr] (1 - ⅇ^-t) + Tr ⅇ^-t;
          )
        ]
```

Figure 5.2: The code used for creating the heat flow demonstration shown in Figure 5.1.

exponential time dependence. The heat capacity is chosen to be a constant. The code in Figure 5.2 contains several lines (ca. 20) of Mathematica's built-in functions, which produce all of the visual and interactive components of the demonstration.

5.4 Subsequent Implementations of Compute-to-Learn

Since the initial pilot run, the compute-to-learn honors studio has been offered two additional times in the Fall 2016 and Winter 2017 semesters. These subsequent iterations presented opportunities to ameliorate problems that became evident after the first semester (Fall 2015). At the end of the first iteration of compute-to-learn, the students, peer leaders, and GSIs had an informal discussion about the studio in order to generate a set of modifications for improving on the studio experience and execution. For the following iterations, we developed and conducted formal interviews with individual students, which are discussed in more detail in the next section. We sought Institutional Review Board (IRB) approval for these interviews and surveys involving students, which were determined to be exempt from IRB oversight. Most of the concerns that students mentioned were centered on time management and project management, as well as misleading visualizations stemming from misunderstandings of physical chemistry concepts. Common concerns from students revolved around not knowing where to start with their code or experiencing frustration during extended time periods where it was felt that little progress was being made. As a way to help address these issues, as well as further promote collaboration, we encouraged students to work in groups of two or three in the Fall 2016 and Winter 2017 semesters.

Similar to the issues found in the writing-to-teach implementation, we found that students were prone to creating confusing visualizations of concepts. For example, a student who was showing the difference between temperature and heat chose to show heat change on a thermometer. For this reason, we decided to increase the level of GSI involvement to a role similar to that of a research advisor, with the purpose of addressing misconceptions and ensuring physically accurate representations earlier in the semester. Additionally, the GSIs began holding weekly office hours during the Winter 2017 semester so that students had a forum between studio sessions to ask questions and discuss problems they were having.

In the first iteration of the studio, many students indicated that they would have liked to have additional time in the studio allocated to programming their projects, and would rather have spent less time on the Mathematica tutorial. To accommodate this, we reduced the length of the tutorial from four weeks to three weeks for both the Fall 2016 and Winter 2017 iterations of the studio. While this presented the students with less formal training in programming with Mathematica, most students expressed their appreciation for having more time to program. With an extra week available for programming, we instituted an additional peer review session the week prior to submission of the demonstrations, as we found the peer review sessions and the discussions that took place during them to be very beneficial during the first iteration. This provided the students, peer leaders, and GSIs with another chance to identify mistakes. With this additional peer review session, students were able to discuss and compare challenges they were facing with their projects, and to provide suggestions or solutions to their peers. Because most of the students in the first iteration did not follow through with publication once the semester had ended, in subsequent iterations we asked all students to submit their demonstrations for publication three weeks prior to the end of the semester. This allowed time to receive official review from the Wolfram Demonstrations Project and implement any changes that were required before the end of the semester.

In addition to format changes, we have expanded the studio to include students from the second semester general chemistry/physical chemistry course for non-chemistry majors (CHEM 230), in order to enhance diversity and increase communication between the two groups of students. CHEM 230 covers many of the same topics as the CHEM 260 course, including thermodynamics, kinetics, electrochemistry, and nuclear chemistry. It excludes calculus-based formulations and quantum mechanics. The CHEM 230H and CHEM 260H students met together within the same studio environment as a single class, enabling collaboration between students with different levels of physical chemistry and mathematics knowledge. Opening the honors studio to CHEM 230 students increased enrollment, and had the benefit of allowing for more collaboration and a greater diversity of projects among students.

Many of the students enrolled in CHEM 230 are interested in health professions and medicine. To tailor the honors studio experience to better fit their needs, we invited a guest speaker from the University of Michigan Medical School during the Winter 2017 iteration of the studio. The invited speaker was a medical student who uses programming with his own medical studies to help promote understanding of some medical topics that are not easy for students or patients to understand. The speaker presented computer programming in a context that many of the students could relate to. As one student put it:

> He used programming a lot using medical concepts and I thought that was really cool, and right now I'm trying to choose between one or the other and it just gave me the idea, "Why not do both?"

The students were extremely interested in his talk; it further motivated them to learn more about programming and complete their projects.

A comparison of the three iterations of the compute-to-learn honors studio is shown in Table 5.2. With the modifications made in each successive iteration, the number of publications increased significantly. In the first semester, one of six students published, while in the second iteration of the studio three of four groups published. In the most recent semester, where we had the most students and strictly enforced the submission deadline, all nine groups submitted and published their demonstrations. We also retained the most students in the Winter 2017 semester, with only about 20% deciding to drop out of the studio compared to 50% in the prior semesters.

5.5 Student Outcomes from the Compute-to-Learn Studio

We conducted formal interviews at the end of the Fall 2016 and Winter 2017 iterations of the compute-to-learn studio to assess student experiences and outcomes. Our hypothesis was that the students enrolled in the honors studio would gain meaningful experience and familiarity with the scientific research process, as well as new skills in programming and problem solving. The interviews were voluntary for the students and were comprised of ten general questions about their experience in the

Parameters	Fall 2015	Fall 2016	Winter 2017
Courses Involved	CHEM 260	CHEM 260 CHEM 230	CHEM 260 CHEM 230
Students Initially Enrolled in Studio	12	16	24
Students Enrolled at End of Studio	6	8	19
Tutorial Length	4 weeks	3 weeks	3 weeks
Individual/Group	Individual	Groups 1-3	Groups 2-3
Guest Speaker	No	No	Yes
GSI Involvement	Minimal	Biweekly meetings with groups	1 GSI per 3 groups; biweekly meetings
Office Hours	No	No	Yes
Submission Deadline	Last week of semester	3 weeks before end of semester (loosely enforced)	3 weeks before end of semester (strictly enforced)
Number of Published Demos	1 of 6	3 of 4	9 of 9

Table 5.2: Comparing three iterations of Compute-to-Learn studios.

studio (see Appendix A). The interviews were conducted by studio peer leaders from the previous semester. The students were not acquainted with their interviewer so that they could speak more freely about their experiences. Eight students were interviewed in the Fall 2016 semester, and nine students were interviewed in the Winter 2017 semester. Audio recordings of the interviews were transcribed and then coded to identify commonalities and overarching themes. While many of the themes that we identified fit well with our hypothesis, others came as a surprise.

The themes most commonly mentioned by five or more students can be placed into the following seven categories:

1. Desire to learn programming (mentioned by all 17 students)
2. Appreciation for peer review
3. Independent learning
4. Learning to ask questions
5. Benefits of group work
6. Appreciation for hands-on activities
7. Need for patience and practice when faced with a new challenge

The most universal theme we discovered was that every student was either motivated to join the studio because of the opportunity to learn to code or finished the studio with a sense of accomplishment having gained programming skills. As one student described the reason they joined the compute-to-learn studio, "I thought it would be really interesting because I don't have any coding experience, and I don't think I would have had the opportunity to take any classes on coding." After working closely with the students and analyzing the interviews, we found that many of the students shared this sentiment of not having the opportunity or the ability to learn computer programming within the confines of their curricula. The compute-to-learn studio provided students in CHEM 230 and 260 with an environment in which they could learn how to code within the context of a required chemistry course. Many students felt that the greatest skill they learned in the studio was how to code; as one student put it, “Just learning what code really is, and I guess how it works, because I had no interaction with that before.”

The remaining six categories fit well into the main purpose of the studio: to apprentice students into a scientific community via an authentic research experience. To identify this, we looked for an impact on the following student abilities:

1. The ability to learn independently while collaborating with a broader community
2. The ability to ask substantive, pertinent questions and to expediently ask a colleague or mentor for assistance when necessary
3. The ability to manipulate or analyze data or information into a presentable form

Many of the students commented on the sense of accomplishment associated with being able to independently learn complex topics or navigate various resources to resolve programming issues, without relying on formal instruction from a teacher. In one student’s words, “I think I learned how to teach myself how to use the online guides and play with them, and kind of just figure it out without much official lecture,” while another student described it as, “Alright, this is an individual project and you’re going to have to figure it out on your own.” Other students even mentioned that they found it more “fun” and fulfilling to research their problems independently and come to a solution without help.

Many students also mentioned that they learned the benefits of knowing when and how to seek help, rather than spend an exorbitant amount of time trying to solve problems on their own. Additionally, they found the peer-review process generally helpful, both from the perspective of the reviewer and as the presenter. As a researcher, the process of official peer review prior to publication in a journal is integral to the scientific process. While we expected students to underappreciate the importance of this part of their project, a sizeable number mentioned how important peer review was to submitting a high-quality demonstration. For example, one student offered the following observations:

> It was really useful when we would present our storyboard and then everyone else would tell us what they thought about it, because we already have our own opinions on it. I was like, "Oh, I think it's perfect already, the way it is," and the audience members, our peers, were like "Oh, I think you should add that and then you'll clarify this one point for other people," and I was like "Oh, I didn't know that's another way to view my demo." So, be open to other comments that people might have.

In addition to the benefit of peer review, many students discovered the interdisciplinary aspect of research through their participation in the studio. Students learned that they could utilize computer skills, which they originally did not relate with chemistry, to help guide their chemistry research. As one student phrased it, "I definitely think that's a skill, to be able to analyze something and then be able to use your intuition to translate that to another field. Chemistry into computer science, I thought that was a good skill to pick up." Overall, the feedback from the interviews was positive. In addition, their comments were consistent with our original hypothesis that the compute-to-learn studio constitutes an experience for the students that resembles that of scientific research.

5.6 Future Directions

After completion of three full semesters of the compute-to-learn studio, it is clear that the studio provides a suitable environment for students interested in scientific programming to learn how to write code in Mathematica and to utilize this skill to explain physical chemistry concepts. While we recognize that the low ratio of students to peer leaders and GSIs would make scaling up the studio to a traditional large lecture setting challenging, we would like to emphasize the fact that the Wolfram Mathematica software is incredibly versatile, as the Wolfram Demonstration Project includes demonstrations from a wide variety of fields. As such, the compute-to-learn pedagogy that we implemented within the CHEM 260H and CHEM 230H studio can easily be generalized and extended to many other courses and disciplines. For example, the studio could be easily extended to quantitative courses in Physics, Statistics, Economics, Math, and Engineering. The software and pedagogy is also suitable for more qualitative topics, such as those found in Biology, Medicine, Art, and Architecture.

Going forward, several ways of expanding and strengthening the pedagogy will be investigated. For example, we intend for the peer leaders to take stronger leadership roles in the forthcoming Fall 2017 iteration. We are also considering shortening the tutorial to two weeks as we have seen the students' confidence in self-guided learning of programming increase semester to semester. This will give the students more time to research their chosen prompts before presenting their storyboards and beginning to code. Overall, we wish to make note of the positive impact the studio had on the students' ability to problem solve, develop an appreciation for research, and acquire confidence in learning new and useful skills such as programming.

We also plan on expanding our assessment efforts. In the Fall 2016 and Winter 2017, we collected some preliminary data regarding student attitudes about chemistry using the "Colorado Learning Attitudes about Science Survey" (CLASS survey).[218] The survey was given to all students enrolled in CHEM 230 and CHEM 260, including the students enrolled in CHEM 230H and CHEM 260H, at the beginning and end of the semester. The CLASS survey is meant to model the distinctive differences between novice and expert learners' beliefs about learning science and science as a discipline. Ideally, a person who takes part in research would be defined as a more expert learner while a non-researcher would be a novice learner. At the end of each semester, the surveys showed neither a positive nor a negative relationship for the students enrolled in either the normal CHEM 230/260 course or the CHEM 230H/260H compute-to-learn studio. We will continue to expand and improve the compute-to-learn pedagogy by expanding our assessment and continuing to improve the studio, which we hope will benefit anyone in the scientific community who will consider adopting this pedagogy.

CHAPTER VI

Conclusions and Outlook

6.1 Summary

The work presented in this dissertation has focused on understanding the processes of energy transfer in organic materials and investigating the spectroscopic signatures of these processes. Advancement in the design of photovoltaic and luminescent organic materials is facilitated by molecular level insights gained through both experimental observations and theoretical and computational modeling. Thus, these studies have utilized computational techniques to investigate excited states in molecular systems that are experimentally relevant for organic photovoltaics and scintillators.

Vibrational frequency shifts in OPVs were explored using a model C_{60}CO–DMA system, as well as the more experimentally relevant PCBM–DMA. Frequencies of carbonyl reporter modes in both systems show a linear correlation to changes in the electric field strength along the modes, with STRs of 0.673 and 0.768 cm^{-1}/(MV/cm) for C_{60}CO–DMA and PCBM–DMA, respectively. While C_{60}CO–DMA showed significant red shifts of 10–20 cm^{-1} upon CT due to the proximity of the C=O to the charged fullerene, frequency shifts in PCBM–DMA were much smaller at less than 4 cm^{-1}. Also of note in PCBM–DMA, the direction of the shifts depend on the orientation of the reporter mode relative to the CT coordinate. Given these results, it is not clear whether the VSEs induced by CT would contribute significantly to the frequency shifts observed experimentally in similar PCBM materials.[16]

CT was also studied for a carotenoid–porphyrin–C_{60} molecular triad. CT rate constants were calculated between the excited $\pi\pi^*$ state, the porphyrin-to-C_{60} CT state, and the carotenoid-to-C_{60} charge-separated state for the two primary conformations of the triad, bent and linear. Charge-separation was found to occur via a two-step mechanism, with the rate-determining bent-to-linear conformation change mediating the second step. The CT process was also determined to be driven by the THF solvent. Vibrational frequency distributions were calculated for the amide I stretch using conformations from MD simulations, and the frequency was found to be very sensitive to the electronic state, with shifts as large as $\sim$60 cm^{-1}. The electric field, however, showed a lack of correlation to the frequency shifts, suggesting that the observed shift is due to a through-bond quantum-chemical effect rather than through-space Stark effects.

The process of ISC and its role in the PSD ability of the organic scintillator material *trans*–stilbene was also examined in this dissertation, using the recently developed OT–SRSH–PCM method.[70] ISC rate constants between the S_1 and first four T_n excited states were calculated using an equilibrium FGR approach. The rates were found to be significantly slower than that of prompt fluorescence (3.4 ns),[190] and thus have a negligible impact on PSD. The rates were also found to increase with increasing torsion of the *trans*–stilbene dihedral angle, but still remain about an order of magnitude slower than prompt fluorescence within the range of angles expected in crystalline *trans*–stilbene. Deuteration of *trans*–stilbene led to a decrease in the ISC rate constants by as much as 30%, although this effect is due in part to increases in the reorganization energies calculated using the HRFs.

6.2 Outlook

This work supports the use of vibrational reporter modes as means of studying CT in OPV materials, though there is much room for further investigation. For the case of the PCBM system, the effect of different electron donor species on the observed frequency shifts and Stark effects may be significant and should be explored. The surrounding environment would also be expected to have a significant impact on the electric field. As in Chapter III, MD simulations incorporating the solvent environment could be performed for PCBM-based systems, and representative conformations could be analyzed to investigate the impact of the surrounding environment.

This approach showed a clear dependence of the amide I vibrational frequencies in the CPC$_{60}$ triad on the electronic state of the system, and the widths of the frequency distributions were in good agreement with previously reported values.[156,158,159] Experimental investigation using ultrafast 2DIR, similar to those performed with other OPV materials,[11–22] can take advantage of this dependence to study charge transfer and subsequent charge separation in this system. This work can also be extended by accounting for nonequilibrium initial states[160] and using polarizable force fields.[147]

ISC has been shown to not significantly impact in the PSD ability of *trans*–stilbene, due to the fact that the rate is significantly slower than that of prompt fluorescence. However, there are two other processes that play a role, triplet migration and TTA. A dimer model can be utilized along with CDFT to constrain the spins and effectively model these intermolecular processes. If deuteration exhibits a similar effect on triplet migration and TTA as experienced with ISC, i.e. significantly decreased rates, this would lead to slower delayed fluorescence. This in turn would increase PSD, and explain the improved PSD observed experimentally in *trans*–stilbene–d$_{12}$.[44]

APPENDIX

APPENDIX A

Supporting Information – Compute-to-Learn: Authentic Learning via Development of Interactive Computer Demonstrations within a Peer-Led Studio Environment

A.1 Interview Questions

1. What were the reasons that made you want to join the honors studio?
2. What was the biggest challenge that you encountered through your participation in the honors studio, and how did you overcome it?
3. What was your biggest accomplishment in the honors studio?
4. What are the most important skills that you learned through your participation in the honors studio?
5. What are the most important lessons that you learned through your participation in the honors studio?
6. What advice would you give to future participants regarding how to be successful at producing a publishable demo?
7. Did participation in the studio have an impact on your view of scientific research, and if so in what way?

8. Did participation in the studio change in any way your view of your own strengths and weaknesses as a scientist, and if so how?
9. Did participation in the studio have an impact on your future professional plans, and if so in what way?
10. In your opinion, how did your participation in the studio impact your performance in CHEM 230/260?

BIBLIOGRAPHY

BIBLIOGRAPHY

[1] Coropceanu, V.; Cornil, J.; da Silva Filho, D. A.; Olivier, Y.; Silbey, R.; Brédas, J.-L. Charge Transport in Organic Semiconductors. *Chemical Reviews* **2007**, *107*, 926–952, PMID: 17378615.

[2] Dennler, G.; Scharber, M. C.; Brabec, C. J. Polymer-Fullerene Bulk-Heterojunction Solar Cells. *Advanced Materials* **2009**, *21*, 1323–1338.

[3] Dou, L.; You, J.; Hong, Z.; Xu, Z.; Li, G.; Street, R. A.; Yang, Y. 25th Anniversary Article: A Decade of Organic/Polymeric Photovoltaic Research. *Advanced Materials* **2013**, *25*, 6642–6671.

[4] Yu, J.; Zheng, Y.; Huang, J. Towards High Performance Organic Photovoltaic Cells: A Review of Recent Development in Organic Photovoltaics. *Polymers* **2014**, *6*, 2473–2509.

[5] Burroughes, J.; Bradley, D.; Brown, A.; Marks, R.; Mackay, K.; Friend, R.; Burns, P.; Holmes, A. Light-emitting diodes based on conjugated polymers. *nature* **1990**, *347*, 539.

[6] Grimsdale, A. C.; Leok Chan, K.; Martin, R. E.; Jokisz, P. G.; Holmes, A. B. Synthesis of Light-Emitting Conjugated Polymers for Applications in Electroluminescent Devices. *Chemical Reviews* **2009**, *109*, 897–1091, PMID: 19228015.

[7] McCulloch, I.; Heeney, M.; Bailey, C.; Genevicius, K.; MacDonald, I.; Shkunov, M.; Sparrowe, D.; Tierney, S.; Wagner, R.; Zhang, W.; Chabinyc, M.; Kline, R.; McGehee, M.; Toney, M. Liquid-crystalline semiconducting polymers with high charge-carrier mobility. *Nature materials* **2006**, *5*, 328.

[8] Zaumseil, J.; Sirringhaus, H. Electron and Ambipolar Transport in Organic Field-Effect Transistors. *Chemical Reviews* **2007**, *107*, 1296–1323, PMID: 17378616.

[9] Pelzer, K. M.; Darling, S. B. Charge generation in organic photovoltaics: a review of theory and computation. *Mol. Syst. Des. Eng.* **2016**, *1*, 10–24.

[10] Zhao, W.; Li, S.; Yao, H.; Zhang, S.; Zhang, Y.; Yang, B.; Hou, J. Molecular Optimization Enables over 13% Efficiency in Organic Solar Cells. *Journal of the American Chemical Society* **2017**, *139*, 7148–7151, PMID: 28513158.

[11] Barbour, L. W.; Hegadorn, M.; Asbury, J. B. Microscopic Inhomogeneity and Ultrafast Orientational Motion in an Organic Photovoltaic Bulk Heterojunction Thin Film Studied with 2D IR Vibrational Spectroscopy. *J. Phys. Chem. B* **2006**, *110*, 24281.

[12] Barbour, L. W.; Hegadorn, M.; Asbury, J. B. Watching Electrons Move in Real Time: Ultrafast Infrared Spectroscopy of a Polymer Blend Photovoltaic Material. *J. Am. Chem. Soc.* **2007**, *129*, 15884.

[13] Barbour, L. W.; Pensack, R. D.; Hegadorn, M.; Arzhantsev, S.; Asbury, J. B. Excitation Transport and Charge Separation in an Organic Photovoltaic Material: Watching Excitations Diffuse to Interfaces. *J. Phys. Chem. C* **2008**, *112*, 3926.

[14] Pensack, R. D.; Banyas, K. M.; Barbour, L. W.; Hegadorn, M.; Asbury, J. B. Ultrafast Vibrational Spectroscopy of Charge-carrier Dynamics in Organic Photovoltaic Materials. *Phys. Chem. Chem. Phys.* **2009**, *11*, 2575.

[15] Pensack, R. D.; Asbury, J. B. Barrierless Free Carrier Formation in an Organic Photovoltaic Material Measured with Ultrafast Vibrational Spectroscopy. *J. Am. Chem. Soc.* **2009**, *131*, 15986.

[16] Pensack, R. D.; Banyas, K. M.; Asbury, J. B. Vibrational Solvatochromism in Organic Photovoltaic Materials: Method to Distinguish Molecules at Donor/Acceptor Interfaces. *Phys. Chem. Chem. Phys.* **2010**, *12*, 14144.

[17] Pensack, R. D.; Banyas, K. M.; Asbury, J. B. Charge Trapping in Organic Photovoltaic Materials Examined with Time-Resolved Vibrational Spectroscopy. *J. Phys. Chem. C* **2010**, *114*, 5344.

[18] Pensack, R. D.; Asbury, J. B. Beyond the Adiabatic Limit: Charge Photogeneration in Organic Photovoltaic Materials. *J. Phys. Chem. Lett.* **2010**, *1*, 2255.

[19] Pensack, R. D.; Banyas, K. M.; Asbury, J. B. Temperature-Independent Vibrational Dynamics in an Organic Photovoltaic Material. *J. Phys. Chem. B* **2010**, *114*, 12242.

[20] Pensack, R. D.; Asbury, J. B. Ultrafast Probes of Charge Transfer States in Organic Photovoltaic Materials. *Chem. Phys. Lett.* **2011**, *515*, 197.

[21] Pensack, R. D.; Guo, C.; Vakhshouri, K.; Gomez, E. D.; Asbury, J. B. Influence of Acceptor Structure on Barriers to Charge Separation in Organic Photovoltaic Materials. *J. Phys. Chem. C* **2012**, *116*, 4824.

[22] Jeong, K. S.; Pensack, R. F.; Asbury, J. B. Vibrational Spectroscopy of Electronic Processes in Emerging Photovoltaic Materials. *Acc. Chem. Res.* **2013**, *46*, 1538.

[23] Park, E. S.; Boxer, S. G. Origins of the Sensitivity of Molecular Vibrations to Electric Fields: Carbonyl and Nitrosyl Stretches in Model Compounds and Proteins. *The Journal of Physical Chemistry B* **2002**, *106*, 5800–5806.

[24] Boxer, S. G. Stark Realities. *The Journal of Physical Chemistry B* **2009**, *113*, 2972–2983, PMID: 19708160.

[25] Park, E. S.; Andrews, S. S.; Hu, R. B.; Boxer, S. G. Vibrational Stark Spectroscopy in Proteins: A Probe and Calibration for Electrostatic Fields. *The Journal of Physical Chemistry B* **1999**, *103*, 9813–9817.

[26] Park, E. S.; Thomas, M. R.; Boxer, S. G. Vibrational Stark Spectroscopy of NO Bound to Heme: Effects of Protein Electrostatic Fields on the NO Stretch Frequency. *Journal of the American Chemical Society* **2000**, *122*, 12297–12303.

[27] Suydam, I. T.; Boxer, S. G. Vibrational Stark Effects Calibrate the Sensitivity of Vibrational Probes for Electric Fields in Proteins. *Biochemistry* **2003**, *42*, 12050–12055, PMID: 14556636.

[28] Hohenberg, P.; Kohn, W. Inhomogeneous Electron Gas. *Phys. Rev.* **1964**, *136*, B864–B871.

[29] Cramer, C. J. *Essentials of Computational Chemistry: Theories and Models*, 2nd ed.; John Wiley and Sons: West Sussex, England, 2004.

[30] Kohn, W.; Sham, L. J. Self-Consistent Equations Including Exchange and Correlation Effects. *Phys. Rev.* **1965**, *140*, A1133–A1138.

[31] Parr, R. G.; Yang, W. Density-Functional Theory of the Electronic Structure of Molecules. *Annual Review of Physical Chemistry* **1995**, *46*, 701–728, PMID: 24341393.

[32] Perdew, J. P.; Schmidt, K. In *Density functional theory and its application to materials*; Van Doren, V., Van Alsenoy, K., Geerlings, P., Eds.; American Institute of Physics: Melville, NY, 2001; pp 1–20.

[33] Becke, A. D. Densityfunctional thermochemistry. III. The role of exact exchange. *The Journal of Chemical Physics* **1993**, *98*, 5648–5652.

[34] Stephens, P. J.; Devlin, F. J.; Chabalowski, C. F.; Frisch, M. J. Ab Initio Calculation of Vibrational Absorption and Circular Dichroism Spectra Using Density Functional Force Fields. *The Journal of Physical Chemistry* **1994**, *98*, 11623–11627.

[35] Phillips, H.; Zheng, Z.; Geva, E.; Dunietz, B. D. Orbital gap predictions for rational design of organic photovoltaic materials. *Organic Electronics* **2014**, *15*, 1509 – 1520.

[36] Dederichs, P. H.; Blügel, S.; Zeller, R.; Akai, H. Ground States of Constrained Systems: Application to Cerium Impurities. *Phys. Rev. Lett.* **1984**, *53*, 2512–2515.

[37] Becke, A. D. A multicenter numerical integration scheme for polyatomic molecules. *The Journal of Chemical Physics* **1988**, *88*, 2547–2553.

[38] Kaduk, B.; Kowalczyk, T.; Van Voorhis, T. Constrained Density Functional Theory. *Chemical Reviews* **2012**, *112*, 321–370, PMID: 22077560.

[39] Kouzes, R. T. *The 3He Supply Problem*; 2009.

[40] Brooks, F. Development of organic scintillators. *Nuclear Instruments and Methods* **1979**, *162*, 477 – 505.

[41] Laustriat, G. The luminescence decay of organic scintillators. *Molecular Crystals* **1968**, *4*, 127–145.

[42] King, T. A.; Voltz, R. The time dependence of scintillation intensity in aromatic materials. *Proceedings of the Royal Society of London A: Mathematical, Physical and Engineering Sciences* **1966**, *289*, 424–439.

[43] Fulvio, A. D.; Schubert, A.; Basley, A. T.; Williams, K.; Geva, E.; Dunietz, B. D.; Pozzi, S. A. Pulse Shape Discrimination in Organic Scintillator Materials The Role of Intersystem Crossing. Poster presented at the Symposium on Radiation Measurements and Applications (SORMA XVII), University of Michigan, 2018.

[44] Carman, M.; Glenn, A.; Mabe, A.; Becchetti, F.; Payne, S.; Zaitseva, N. Solution growth of a deuterated trans-stilbene crystal for fast neutron detection. *Journal of Crystal Growth* **2018**, *498*, 51 – 55.

[45] Runge, E.; Gross, E. K. U. Density-Functional Theory for Time-Dependent Systems. *Phys. Rev. Lett.* **1984**, *52*, 997–1000.

[46] Marques, M.; Gross, E. Time-Dependent Density Functional Theory. *Annual Review of Physical Chemistry* **2004**, *55*, 427–455, PMID: 15117259.

[47] Casida, M. E. Time-dependent density-functional theory for molecules and molecular solids. *Journal of Molecular Structure: THEOCHEM* **2009**, *914*, 3 – 18, Time-dependent density-functional theory for molecules and molecular solids.

[48] Casida, M. E. Time-Dependent Density Functional Response Theory for Molecules. In *Recent Advances in Density Functional Methods*; World Scientific: Singapore, 1995; pp 155–192.

[49] Dreuw, A.; Weisman, J. L.; Head-Gordon, M. Long-range charge-transfer excited states in time-dependent density functional theory require non-local exchange. *The Journal of Chemical Physics* **2003**, *119*, 2943–2946.

[50] Dreuw, A.; Head-Gordon, M. Failure of Time-Dependent Density Functional Theory for Long-Range Charge-Transfer Excited States: The ZincbacteriochlorinBacteriochlorin and BacteriochlorophyllSpheroidene Complexes. *Journal of the American Chemical Society* **2004**, *126*, 4007–4016, PMID: 15038755.

[51] Tirado-Rives, J.; Jorgensen, W. L. Performance of B3LYP Density Functional Methods for a Large Set of Organic Molecules. *Journal of Chemical Theory and Computation* **2008**, *4*, 297–306, PMID: 26620661.

[52] Savin, A.; Flad, H.-J. Density functionals for the Yukawa electron-electron interaction. *International Journal of Quantum Chemistry* **1995**, *56*, 327–332.

[53] Leininger, T.; Stoll, H.; Werner, H.-J.; Savin, A. Combining long-range configuration interaction with short-range density functionals. *Chemical Physics Letters* **1997**, *275*, 151 – 160.

[54] Yanai, T.; Tew, D. P.; Handy, N. C. A new hybrid exchange–correlation functional using the Coulomb-attenuating method (CAM-B3LYP). *Chemical Physics Letters* **2004**, *393*, 51 – 57.

[55] Stein, T.; Kronik, L.; Baer, R. Reliable Prediction of Charge Transfer Excitations in Molecular Complexes Using Time-Dependent Density Functional Theory. *Journal of the American Chemical Society* **2009**, *131*, 2818–2820, PMID: 19239266.

[56] Stein, T.; Eisenberg, H.; Kronik, L.; Baer, R. Fundamental Gaps in Finite Systems from Eigenvalues of a Generalized Kohn-Sham Method. *Phys. Rev. Lett.* **2010**, *105*, 266802.

[57] Perdew, J. P.; Parr, R. G.; Levy, M.; Balduz, J. L. Density-Functional Theory for Fractional Particle Number: Derivative Discontinuities of the Energy. *Phys. Rev. Lett.* **1982**, *49*, 1691–1694.

[58] Levy, M.; Perdew, J. P.; Sahni, V. Exact differential equation for the density and ionization energy of a many-particle system. *Phys. Rev. A* **1984**, *30*, 2745–2748.

[59] Almbladh, C.-O.; von Barth, U. Exact results for the charge and spin densities, exchange-correlation potentials, and density-functional eigenvalues. *Phys. Rev. B* **1985**, *31*, 3231–3244.

[60] Perdew, J. P.; Levy, M. Comment on “Significance of the highest occupied Kohn-Sham eigenvalue”. *Phys. Rev. B* **1997**, *56*, 16021–16028.

[61] Salzner, U.; Baer, R. Koopmans’ springs to life. *The Journal of Chemical Physics* **2009**, *131*, 231101.

[62] Kronik, L.; Kümmel, S. Dielectric Screening Meets Optimally Tuned Density Functionals. *Advanced Materials* **2018**, 1706560.

[63] Stein, T.; Kronik, L.; Baer, R. Prediction of charge-transfer excitations in coumarin-based dyes using a range-separated functional tuned from first principles. *The Journal of Chemical Physics* **2009**, *131*, 244119.

[64] Karolewski, A.; Stein, T.; Baer, R.; Kümmel, S. Communication: Tailoring the optical gap in light-harvesting molecules. *The Journal of Chemical Physics* **2011**, *134*, 151101.

[65] Refaely-Abramson, S.; Sharifzadeh, S.; Jain, M.; Baer, R.; Neaton, J. B.; Kronik, L. Gap renormalization of molecular crystals from density-functional theory. *Phys. Rev. B* **2013**, *88*, 081204.

[66] Sivasubramanian, S.; Widom, A.; Srivastava, Y. The Clausius–Mossotti phase transition in polar liquids. *Physica A: Statistical Mechanics and its Applications* **2005**, *345*, 356 – 366.

[67] Lüftner, D.; Refaely-Abramson, S.; Pachler, M.; Resel, R.; Ramsey, M. G.; Kronik, L.; Puschnig, P. Experimental and theoretical electronic structure of quinacridone. *Phys. Rev. B* **2014**, *90*, 075204.

[68] Manna, A. K.; Refaely-Abramson, S.; Reilly, A. M.; Tkatchenko, A.; Neaton, J. B.; Kronik, L. Quantitative Prediction of Optical Absorption in Molecular Solids from an Optimally Tuned Screened Range-Separated Hybrid Functional. *Journal of Chemical Theory and Computation* **2018**, *14*, 2919–2929, PMID: 29727172.

[69] Refaely-Abramson, S.; Jain, M.; Sharifzadeh, S.; Neaton, J. B.; Kronik, L. Solid-state optical absorption from optimally tuned time-dependent range-separated hybrid density functional theory. *Phys. Rev. B* **2015**, *92*, 081204.

[70] Bhandari, S.; Kronik, L.; Dunietz, B. D. Fundamental gaps of condensed-phase organic semiconductors from single-molecule polarization-consistent optimally-tuned screened range-separated hybrid functional (tentative title), to be published.

[71] Monthly Energy Review. http://www.eia.gov/totalenergy/data/monthly/, (accessed Jun 2018).

[72] Brabec, C. J. Organic photovoltaics: technology and market. *Solar Energy Materials and Solar Cells* **2004**, *83*, 273 – 292, The development of organic and polymer photovoltaics.

[73] Günes, S.; Neugebauer, H.; Sariciftci, N. S. Conjugated Polymer-Based Organic Solar Cells. *Chemical Reviews* **2007**, *107*, 1324–1338, PMID: 17428026.

[74] Thompson, B.; Fréchet, J. Polymer–Fullerene Composite Solar Cells. *Angewandte Chemie International Edition* **2007**, *47*, 58–77.

[75] Krebs, F. C. Fabrication and processing of polymer solar cells: A review of printing and coating techniques. *Solar Energy Materials and Solar Cells* **2009**, *93*, 394 – 412, Processing and Preparation of Polymer and Organic Solar Cells.

[76] Chen, L.-M.; Hong, Z.; Li, G.; Yang, Y. Recent Progress in Polymer Solar Cells: Manipulation of Polymer:Fullerene Morphology and the Formation of Efficient Inverted Polymer Solar Cells. *Advanced Materials* **2009**, *21*, 1434–1449.

[77] Li, G.; Zhu, R.; Yang, Y. Polymer solar cells. *Nature photonics* **2012**, *6*, 153.

[78] Heliatek Technical Data. http://www.heliatek.com/en/solar-films/technical-data, (accessed May 2018).

[79] Kippelen, B.; Bredas, J.-L. Organic photovoltaics. *Energy Environ. Sci.* **2009**, *2*, 251–261.

[80] Brewer, S. H.; Franzen, S. A quantitative theory and computational approach for the vibrational Stark effect. *The Journal of Chemical Physics* **2003**, *119*, 851–858.

[81] Baiz, C. R.; Kubarych, K. J. Ultrafast Vibrational Stark-Effect Spectroscopy: Exploring Charge-Transfer Reactions by Directly Monitoring the Solvation Shell Response. *Journal of the American Chemical Society* **2010**, *132*, 12784–12785, PMID: 20738086.

[82] Chai, J.-D.; Head-Gordon, M. Systematic optimization of long-range corrected hybrid density functionals. *The Journal of Chemical Physics* **2008**, *128*, 084106.

[83] Chai, J.-D.; Head-Gordon, M. Long-range corrected hybrid density functionals with damped atom-atom dispersion corrections. *Phys. Chem. Chem. Phys.* **2008**, *10*, 6615–6620.

[84] Krishnan, R.; Binkley, J. S.; Seeger, R.; Pople, J. A. Selfconsistent molecular orbital methods. XX. A basis set for correlated wave functions. *The Journal of Chemical Physics* **1980**, *72*, 650–654.

[85] Shao, Y. et al. Advances in molecular quantum chemistry contained in the Q-Chem 4 program package. *Molecular Physics* **2015**, *113*, 184–215.

[86] Morse, P. M. Diatomic Molecules According to the Wave Mechanics. II. Vibrational Levels. *Phys. Rev.* **1929**, *34*, 57–64.

[87] Wolfram Research, Inc., Mathematica, version 10.2. Champaign, I.L., 2015.

[88] Pauling, L.; E. Bright Wilson, J. *Introduction to Quantum Mechanics with Applications to Chemistry*; Dover Publications: New York, NY, 1985; Chapter 9.

[89] Fried, S. D.; Boxer, S. G. Measuring Electric Fields and Noncovalent Interactions Using the Vibrational Stark Effect. *Accounts of Chemical Research* **2015**, *48*, 998–1006, PMID: 25799082.

[90] Mulliken, R. S. Electronic Population Analysis on LCAO–MO Molecular Wave Functions. I. *The Journal of Chemical Physics* **1955**, *23*, 1833–1840.

[91] Lee, M. H.; Dunietz, B. D.; Geva, E. Calculation from First Principles of Intramolecular Golden-Rule Rate Constants for Photo-induced Electron Transfer in Molecular Donor-Acceptor Systems. *J. Phys. Chem. C* **2013**, *117*, 23391.

[92] Schneider, S. H.; Boxer, S. G. Vibrational Stark Effects of Carbonyl Probes Applied to Reinterpret IR and Raman Data for Enzyme Inhibitors in Terms of Electric Fields at the Active Site. *The Journal of Physical Chemistry B* **2016**, *120*, 9672–9684, PMID: 27541577.

[93] Plattner, N.; Meuwly, M. The Role of Higher CO-Multipole Moments in Understanding the Dynamics of Photodissociated Carbonmonoxide in Myoglobin. *Biophysical Journal* **2008**, *94*, 2505 – 2515.

[94] Muegge, I.; Qi, P. X.; Wand, A. J.; Chu, Z. T.; Warshel, A. The Reorganization Energy of Cytochrome c Revisited. *J. Phys. Chem. B* **1997**, *101*, 825.

[95] Romero, E.; Novoderezhkin, V. I.; van Grondelle, R. Quantum Design of Photosynthesis for Bio-inspired Solar-energy Conversion. *Nature* **2017**, *543*, 355.

[96] Bottari, G.; de la Torre, G.; Guldi, D. M.; Torres, T. Covalent and Noncovalent Phthalocyanine-Carbon Nanostructure Systems: Synthesis, Photoinduced Electron Transfer, and Application to Molecular Photovoltaics. *Chem. Rev.* **2010**, *110*, 6768.

[97] Rizzi, A. C.; van Gastel, M.; Liddell, P. A.; Palacios, R. E.; Moore, G. F.; Kodis, G.; Moore, A. L.; Moore, T. A.; Gust, D.; Braslavsky, S. E. Entropic Changes Control the Charge Separation Process in Triads Mimicking Photosynthetic Charge Separation. *J. Phys. Chem. A* **2008**, *112*, 4215.

[98] Tian, H.; Yu, Z.; Hagfeldt, A.; Kloo, L.; Sun, L. Organic Redox Couples and Organic Counter Electrode for Efficient Organic Dye-Sensitized Solar Cells. *J. Am. Chem. Soc.* **2011**, *133*, 9413.

[99] Mishra, A.; Fischer, M. K. R.; Bäuerle, P. Metal-Free Organic Dyes for Dye-Sensitized Solar Cells: From Structure: Property Relationships to Design Rules. *Angew. Chem., Int. Ed.* **2009**, *48*, 2474.

[100] Feldt, S. M.; Gibson, E. A.; Gabrielsson, E.; Sun, L.; Boschloo, G.; Hagfeldt, A. Design of Organic Dyes and Cobalt Polypyridine Redox Mediators for High-Efficiency Dye-Sensitized Solar Cells. *J. Am. Chem. Soc.* **2010**, *132*, 16714.

[101] Zhao, Y.; Liang, W. Charge Transfer in Organic Molecules for Solar Cells: Theoretical Perspective. *Chem. Soc. Rev.* **2012**, *41*, 1075.

[102] Marcus, R. A. On the Theory of Oxidation-Reduction Reactions Involving Electron Transfer. *J. Chem. Phys.* **1956**, *24*, 966.

[103] Marcus, R. A. Electrostatic Free Energy and Other Properties of States Having Nonequilibrium Polarization. *J. Chem. Phys.* **1956**, *24*, 979.

[104] Marcus, R. A. Electron Transfer Reactions in Chemistry. Theory and Experiment. *Rev. Mod. Phys.* **1993**, *65*, 599.

[105] Barbara, P. F.; Meyer, T. J.; Ratner, M. A. Contemporary Issues in Electron Transfer Research. *J. Phys. Chem.* **1996**, *100*, 13148.

[106] Sun, X.; Geva, E. Equilibrium Fermi's Golden Rule Charge Transfer Rate Constants in the Condensed Phase: The Linearized Semiclassical Method vs Classical Marcus Theory. *J. Phys. Chem. A* **2016**, *120*, 2976.

[107] Leggett, A. J.; Chakravarty, S.; Dorsey, A. T.; Fisher, M. P. A.; Garg, A.; Zwerger, W. Dynamics of the Dissipative Two-state System. *Rev. Mod. Phys.* **1987**, *59*, 1.

[108] Makri, N. The Linear Response Approximation and Its Lowest Order Corrections: An Influence Functional Approach. *J. Phys. Chem. B* **1999**, *103*, 2823.

[109] Cao, J.; Voth, G. A. Modeling Physical Systems by Effective Harmonic Oscillators: The Optimized Quadratic Approximation. *J. Chem. Phys.* **1995**, *102*, 3337.

[110] Weiss, U. *Quantum Dissipative Systems*; World Scientific: Singapore, 1999.

[111] Shi, Q.; Geva, E. Nonradiative Electronic Relaxation Rate Constants from Approximations Based on Linearizing the Path-integral Forward-backward Action. *J. Phys. Chem. A* **2004**, *108*, 6109.

[112] Manna, A. K.; Balamurugan, D.; Cheung, M. S.; Dunietz, B. D. Unraveling the Mechanism of Photoinduced Charge Transfer in Carotenoid–Porphyrin–C60 Molecular Triad. *J. Phys. Chem. Lett.* **2015**, *6*, 1231.

[113] Doorn, S. K.; Dyer, R. B.; Stoutland, P. O.; Woodruff, W. H. Ultrafast Electron Transfer and Coupled Vibrational Dynamics in Cyanide Bridged Mixed-Valence Transition-Metal Dimers. *J. Am. Chem. Soc.* **1993**, *115*, 6398.

[114] Wang, C.; Mohney, B. K.; Akhremitchev, B. B.; Walker, G. C. Ultrafast Infrared Spectroscopy of Vibrational States Prepared by Photoinduced Electron Transfer in (CN)5FeCNRu(NH3)5–. *J. Phys. Chem. A* **2000**, *104*, 4314.

[115] Bredenbeck, J.; Helbing, J.; Hamm, P. Labeling Vibrations by Light: Ultrafast Transient 2D-IR Spectroscopy Tracks Vibrational Modes during Photoinduced Charge Transfer. *J. Am. Chem. Soc.* **2004**, *126*, 990.

[116] Nibbering, E. T. J.; Elsaesser, T. Ultrafast Vibrational Dynamics of Hydrogen Bonds in the Condensed Phase. *Chem. Rev.* **2004**, *104*, 1887.

[117] Hamm, P.; Ohline, S. M.; Zinth, W. Vibrational Cooling After Ultrafast Photoisomerization of Azobenzene Measured by Femtosecond Infrared Spectroscopy. *J. Chem. Phys.* **1997**, *106*, 519.

[118] Herbst, J.; Heyne, K.; Diller, R. Femtosecond Infrared Spectroscopy of Bacteriorhodopsin Chromophore Isomerization. *Science* **2002**, *297*, 822.

[119] Bredenbeck, J.; Helbing, J.; Behrendt, R.; Renner, C.; Moroder, L.; Wachtveitl, J.; Hamm, P. Transient 2D-IR Spectroscopy: Snapshots of the Nonequilibrium Ensemble during the Picosecond Conformational Transition of a Small Peptide. *J. Phys. Chem. B* **2003**, *107*, 8654.

[120] Baiz, C. R.; McCanne, R.; Nee, M. J.; Kubarych, K. J. Orientational Dynamics of Transient Molecules Measured by Nonequilibrium Two-Dimensional Infrared Spectroscopy. *J. Phys. Chem. A* **2009**, *113*, 8907.

[121] Ovchinnikov, A. A.; Ovchinnikova, M. Y. Contribution to the Theory of Elementary Electron Transfer Reactions in Polar Liquids. *Sov. Phys.—JETP* **1969**, *29*, 688.

[122] Egorov, S. A.; Rabani, E.; Berne, B. J. Nonradiative Relaxation Processes in Condensed Phases: Quantum Vs. Classical Baths. *J. Chem. Phys.* **1999**, *110*, 5238.

[123] Nitzan, A. *Chemical Dynamics in Condensed Phases*; Oxford University Press: New York, 2006.

[124] Kubo, R.; Toyozawa, Y. Application of the Method of Generating Function to Radiative and Non-radiative Transitions of a Trapped Electron in a Crystal. *Prog. Theor. Phys.* **1955**, *13*, 160.

[125] Kestner, N. R.; Logan, J.; Jortner, J. Thermal Electron Transfer Reactions in Polar Solvents. *J. Phys. Chem.* **1974**, *78*, 2148.

[126] Jortner, J.; Bixon, M. Intramolecular Vibrational Excitations Accompanying Solvent-controlled Electron Transfer Reactions. *J. Chem. Phys.* **1988**, *88*, 167.

[127] Coalson, R. D.; Evans, D. G.; Nitzan, A. A Nonequilibrium Golden Rule Formula for Electronic State Populations in Nonadiabatically Coupled Systems. *J. Chem. Phys.* **1994**, *101*, 436.

[128] Izmaylov, A. F.; Mendive-Tapia, D.; Bearpark, M. J.; Robb, M. A.; Tully, J. C.; Frisch, M. J. Nonequilibrium Fermi Golden Rule for Electronic Transitions through Conical Intersections. *J. Chem. Phys.* **2011**, *135*, 234106.

[129] Endicott, J. S.; Joubert-Doriol, L.; Izmaylov, A. F. A Perturbative Formalism for Electronic Transitions through Conical Intersections in a Fully Quadratic Vibronic Model. *J. Chem. Phys.* **2014**, *141*, 034104.

[130] Feynman, R. P. *Quantum Mechanics and Path Integrals*; McGraw-Hill: New York, 1965.

[131] Schulman, L. S. *Techniques and Applications of Path Integration*; Wiley: New York, 1981.

[132] Kleinert, H. *Path Integrals in Quantum Mechanics, Statistics and Polymer Physics*; World Scientific: New Jersey, 1995.

[133] Shi, Q.; Geva, E. A Relationship between Semiclassical and Centroid Correlation Functions. *J. Chem. Phys.* **2003**, *118*, 8173.

[134] Shi, Q.; Geva, E. A Comparison between Different Semiclassical Approximations for Optical Response Functions in Nonpolar Liquid Solution II. the Signature of Excited State Dynamics on Two-dimensional Spectra. *J. Chem. Phys.* **2008**, *129*, 124505.

[135] Hillery, M.; O'Connell, R. F.; Scully, M. O.; Wigner, E. P. Distribution Functions in Physics: Fundamentals. *Phys. Rep.* **1984**, *106*, 121.

[136] Press, W. H.; Flannery, B. P.; Teukolsky, S. A.; Vetterling, W. T. *Numerical Recipes*; Cambridge University Press: Cambridge, 1986.

[137] Liddell, P. A.; Kuciauskas, D.; Sumida, J. P.; Nash, B.; Nguyen, D.; Moore, A. L.; Moore, T. A.; Gust, D. Photoinduced Charge Separation and Charge Recombination to a Triplet State in a Carotene-porphyrin-fullerene Triad. *J. Am. Chem. Soc.* **1997**, *119*, 1400.

[138] Carbonera, D.; Di Valentin, M.; Corvaja, C. EPR Investigation of Photoinduced Radical Pair Formation and Decay to a Triplet State in a Carotene-Porphyrin-Fullerene Triad. *J. Am. Chem. Soc.* **1998**, *120*, 4398.

[139] Gust, D.; Moore, T. A.; Moore, A. L. Mimicking Photosynthetic Solar Energy Transduction. *Acc. Chem. Res.* **2001**, *34*, 40.

[140] Kodis, G.; Liddell, P. A.; Moore, A. L.; Moore, T. A.; Gust, D. Synthesis and Photochemistry of a Carotene–porphyrin–fullerene Model Photosynthetic Reaction Center. *J. Phys. Org. Chem.* **2004**, *17*, 724.

[141] Rozzi, C. A.; Maria Falke, S.; Spallanzani, N.; Rubio, A.; Molinari, E.; Brida, D.; Maiuri, M.; Cerullo, G.; Schramm, H.; Christoffers, J. Quantum Coherence Controls the Charge Separation in a Prototypical Artificial Light-harvesting System. *Nat. Commun.* **2013**, *4*, 1602.

[142] Rego, L. G. C.; Hames, B. C.; Mazon, K. T.; Joswig, J.-O. Intramolecular Polarization Induces Electron–Hole Charge Separation in Light-Harvesting Molecular Triads. *J. Phys. Chem. C* **2014**, *118*, 126.

[143] Voityuk, A. A.; Rösch, N. Fragment Charge Difference Method for Estimating Donor-acceptor Electronic Coupling: Application to DNA -stacks. *J. Chem. Phys.* **2002**, *117*, 5607.

[144] Balamurugan, D.; Aquino, A. J. A.; de Dios, F.; Flores, L.; Lischka, H.; Cheung, M. S. Multiscale Simulation of the Ground and Photo-Induced Charge-Separated States of a Molecular Triad in Polar Organic Solvent: Exploring the Conformations, Fluctuations, and Free Energy Landscapes. *J. Phys. Chem. B* **2013**, *117*, 12065.

[145] Jakalian, A.; Jack, D. B.; Bayly, C. I. Fast, Efficient Generation of High-Quality Atomic Charges. AM1-BCC Model: II. Parameterization and Validation. *J. Comput. Chem.* **2002**, *23*, 1623.

[146] Case, D. A. et al. Amber 14. University of California, San Francisco, 2014.

[147] Starovoytov, O. N.; Zhang, P.; Cieplak, P.; Cheung, M. S. Induced Polarization Restricts the Conformational Distribution of a Light-harvesting Molecular Triad in the Ground State. *Phys. Chem. Chem. Phys.* **2017**, *19*, 22969.

[148] Cornell, W. D.; Cieplak, P.; Bayly, C. I.; Gould, I. R.; Merz, K. M.; Ferguson, D. M.; Spellmeyer, D. C.; Fox, T.; Caldwell, J. W.; Kollman, P. A. A Second Generation Force Field for the Simulation of Proteins, Nucleic Acids, and Organinc Molecules. *J. Am. Chem. Soc.* **1995**, *117*, 5179.

[149] Cornell, W. D.; Cieplak, P.; Bayly, C. I.; Gould, I. R.; Merz, K. M.; Ferguson, D. M.; Spellmeyer, D. C.; Fox, T.; Caldwell, J. W.; Kollman, P. A. A Second Generation Force Field for the Simulation of Proteins, Nucleic Acids, and Organic Molecules. *J. Am. Chem. Soc.* **1996**, *118*, 2309.

[150] Wang, J.; Wolf, R. M.; Caldwell, J. W.; Kollman, P. A.; Case, D. A. Development and Testing of a General Amber Force Field. *J. Comput. Chem.* **2004**, *25*, 1157.

[151] Ciccotti, G.; Ryckaert, J. P. Molecular Dynamics Simulation of Rigid Molecules. *Comput. Phys. Rep.* **1986**, *4*, 346.

[152] Darden, T.; York, D.; Pedersen, L. Particle Mesh Ewald: An Nlog(N) Method for Ewald Sums in Large Systems. *J. Chem. Phys.* **1993**, *98*, 10089.

[153] Smirnov, S. N.; Liddell, P. A.; Vlassiouk, I. V.; Teslja, A.; Kuciauskas, D.; Braun, C. L.; Moore, A. L.; Moore, T. A.; Gust, D. Characterization of the Giant Transient Dipole Generated by Photoinduced Electron Transfer in a Carotene-Porphyrin-Fullerene Molecular Triad. *J. Phys. Chem. A* **2003**, *107*, 7567.

[154] King, G.; Warshel, A. Investigation of the Free Energy Functions for Electron Transfer Reactions. *J. Chem. Phys.* **1990**, *93*, 8682.

[155] Schulten, K.; Tesch, M. Coupling of Protein Motion to Electron Transfer: Molecular Dynamics and Stochastic Quantum Mechanics Study of Photosynthetic Reaction Centers. *Chem. Phys.* **1991**, *158*, 421.

[156] Jansen, T. L. C.; Knoester, J. A Transferable Electrostatic Map for Solvation Effects on Amide I Vibrations and Its Application to Linear and Two-dimensional Spectroscopy. *J. Chem. Phys.* **2006**, *124*, 044502.

[157] Jansen, T. L. C.; Dijkstra, A. G.; Watson, T. M.; Hirst, J. D.; Knoester, J. Modeling the Amide I Bands of Small Peptides. *J. Chem. Phys.* **2006**, *125*, 044312.

[158] Kwac, K.; Cho, M. Molecular Dynamics Simulation Study of N-methylacetamide in Water. II. Two-dimensional Infrared Pump-probe Spectra. *J. Chem. Phys.* **2003**, *119*, 2256.

[159] Hayashi, T.; Zhuang, W.; Mukamel, S. Electrostatic DFT Map for the Complete Vibrational Amide Band of NMA. *J. Phys. Chem. A* **2005**, *109*, 9747.

[160] Sun, X.; Geva, E. Nonequilibrium Fermi's Golden Rule Charge Transfer Rates via the Linearized Semiclassical Method. *J. Chem. Theory Comput.* **2016**, *12*, 2926.

[161] Lee, M. H.; Geva, E.; Dunietz, B. D. Calculation from First Principles of Golden-Rule Rate Constants for Photo-Induced Subphthalocyanine/Fullerene Interfacial Charge Transfer and Recombination in Organic Photovoltaic Cells. *J. Phys. Chem. C* **2014**, *118*, 9780.

[162] Lee, M. H.; Dunietz, B. D.; Geva, E. Donor-to-Donor vs. Donor-to-Acceptor Interfacial Charge Transfer States in the Phthalocyanine-Fullerene Organic Photovoltaic System. *J. Phys. Chem. Lett.* **2014**, *5*, 3810.

[163] Lee, M. H.; Geva, E.; Dunietz, B. D. The Effect of Interfacial Geometry on Charge-Transfer States in the Phthalocyanine/Fullerene Organic Photovoltaic System. *J. Phys. Chem. A* **2016**, *120*, 2970.

[164] Bildstein, V. et al. Comparison of deuterated and normal liquid scintillators for fast-neutron detection. *Nuclear Instruments and Methods in Physics Research Section A: Accelerators, Spectrometers, Detectors and Associated Equipment* **2013**, *729*, 188 – 197.

[165] Becchetti, F.; Raymond, R.; Torres-Isea, R.; Fulvio, A. D.; Clarke, S.; Pozzi, S.; Febbraro, M. Deuterated-xylene (xylene-d10; EJ301D): A new, improved deuterated liquid scintillator for neutron energy measurements without time-of-flight. *Nuclear Instruments and Methods in Physics Research Section A: Accelerators, Spectrometers, Detectors and Associated Equipment* **2016**, *820*, 112 – 120.

[166] Becchetti, F.; Raymond, R.; Torres-Isea, R.; Fulvio, A. D.; Clarke, S.; Pozzi, S.; Febbraro, M. Recent developments in deuterated scintillators for neutron measurements at low-energy accelerators. *Nuclear Instruments and Methods in Physics Research Section A: Accelerators, Spectrometers, Detectors and Associated Equipment* **2017**, *874*, 72 – 78.

[167] Fuchs, C.; Heisel, F. Temporal analysis of the delayed fluorescence in isotropic and anisotropic aromatic media under electron excitation. *Radiation Physics and Chemistry (1977)* **1978**, *12*, 95 – 105.

[168] Sternlicht, H.; Nieman, G. C.; Robinson, G. W. Triplet–Triplet Annihilation and Delayed Fluorescence in Molecular Aggregates. *The Journal of Chemical Physics* **1963**, *38*, 1326–1335.

[169] Newton, M. D.; Sutin, N. Electron Transfer Reactions in Condensed Phases. *Annual Review of Physical Chemistry* **1984**, *35*, 437–480.

[170] Newton, M. D. Quantum chemical probes of electron-transfer kinetics: the nature of donor-acceptor interactions. *Chemical Reviews* **1991**, *91*, 767–792.

[171] Mikkelsen, K. V.; Ratner, M. A. Electron tunneling in solid-state electron-transfer reactions. *Chemical Reviews* **1987**, *87*, 113–153.

[172] Jortner, J. Temperature dependent activation energy for electron transfer between biological molecules. *The Journal of Chemical Physics* **1976**, *64*, 4860–4867.

[173] Liang, K. K.; Mebel, A. M.; Lin, S. H.; Hayashi, M.; Selzle, H. L.; Schlag, E. W.; Tachiya, M. Influence of distortion and Duschinsky effects on Marcus-type theories of electron transfer rate. *Phys. Chem. Chem. Phys.* **2003**, *5*, 4656–4665.

[174] Nan, G.; Yang, X.; Wang, L.; Shuai, Z.; Zhao, Y. Nuclear tunneling effects of charge transport in rubrene, tetracene, and pentacene. *Phys. Rev. B* **2009**, *79*, 115203.

[175] Efrima, S.; Bixon, M. Vibrational effects in outer-sphere electron-transfer reactions in polar media. *Chemical Physics* **1976**, *13*, 447 – 460.

[176] Huang, K.; Rhys, A. Theory of light absorption and non-radiative transitions in F-centres. *Proceedings of the Royal Society of London A: Mathematical, Physical and Engineering Sciences* **1950**, *204*, 406–423.

[177] Vault, D. D.; Chance, B. Studies of Photosynthesis Using a Pulsed Laser: I. Temperature Dependence of Cytochrome Oxidation Rate in Chromatium. Evidence for Tunneling. *Biophysical Journal* **1966**, *6*, 825 – 847.

[178] Yin, S.; Li, L.; Yang, Y.; Reimers, J. R. Challenges for the Accurate Simulation of Anisotropic Charge Mobilities through Organic Molecular Crystals: The Phase of mer-Tris(8-hydroxyquinolinato)aluminum(III) (Alq3) Crystal. *The Journal of Physical Chemistry C* **2012**, *116*, 14826–14836.

[179] Truong, T. N.; Stefanovich, E. V. A new method for incorporating solvent effect into the classical, ab initio molecular orbital and density functional theory frameworks for arbitrary shape cavity. *Chemical Physics Letters* **1995**, *240*, 253 – 260.

[180] Barone, V.; Cossi, M. Quantum Calculation of Molecular Energies and Energy Gradients in Solution by a Conductor Solvent Model. *The Journal of Physical Chemistry A* **1998**, *102*, 1995–2001.

[181] Cossi, M.; Rega, N.; Scalmani, G.; Barone, V. Energies, structures, and electronic properties of molecules in solution with the C-PCM solvation model. *Journal of Computational Chemistry* **2003**, *24*, 669–681.

[182] Clark, T.; Chandrasekhar, J.; Spitznagel, G. W.; Schleyer, P. V. R. Efficient diffuse functionaugmented basis sets for anion calculations. III. The 321+G basis set for firstrow elements, Li–F. *Journal of Computational Chemistry* **1983**, *4*, 294–301.

[183] Henderson, T. M.; Janesko, B. G.; Scuseria, G. E. Generalized gradient approximation model exchange holes for range-separated hybrids. *The Journal of Chemical Physics* **2008**, *128*, 194105.

[184] Marian, C. M. Spin–orbit coupling and intersystem crossing in molecules. *Wiley Interdisciplinary Reviews: Computational Molecular Science* **2012**, *2*, 187–203.

[185] Lhost, O.; Brédas, J. L. Theoretical study of torsion potentials in transstilbene and substituted transstilbenes: Modeling torsions in poly(paraphenylene vinylene) and derivatives. *The Journal of Chemical Physics* **1992**, *96*, 5279–5288.

[186] Galvão, D. S.; Soos, Z. G.; Ramasesha, S.; Etemad, S. A parametric method 3 (PM3) study of transstilbene. *The Journal of Chemical Physics* **1993**, *98*, 3016–3021.

[187] Arenas, J. F.; Tocon, I. L.; Otero, J. C.; Marcos, J. I. A Priori Scaled Quantum Mechanical Vibrational Spectra of trans- and cis-Stilbene. *The Journal of Physical Chemistry* **1995**, *99*, 11392–11398.

[188] Molina, V.; Merchán, M.; Roos, B. O. Theoretical Study of the Electronic Spectrum of trans-Stilbene. *The Journal of Physical Chemistry A* **1997**, *101*, 3478–3487.

[189] Massuyeau, F.; Faulques, E.; Latouche, C.; Barone, V. New insights into the vibrational and optical signatures of trans-stilbene via integrated experimental and quantum mechanical approaches. *Phys. Chem. Chem. Phys.* **2016**, *18*, 19378–19385.

[190] Yanagida, T.; Watanabe, K.; Fujimoto, Y. Comparative study of neutron and gamma-ray pulse shape discrimination of anthracene, stilbene, and p-terphenyl. *Nuclear Instruments and Methods in Physics Research Section A: Accelerators, Spectrometers, Detectors and Associated Equipment* **2015**, *784*, 111 – 114, Symposium on Radiation Measurements and Applications 2014 (SORMA XV).

[191] Robertson, J. M.; Woodward, M. A. X-ray analysis of the dibenzyl series IV–detailed structure of stilbene. *Proceedings of the Royal Society of London A: Mathematical, Physical and Engineering Sciences* **1937**, *162*, 568–583.

[192] Finder, C. J.; Newton, M. G.; Allinger, N. L. An improved structure of trans-stilbene. *Acta Crystallographica Section B* **1974**, *30*, 411–415.

[193] Bouwstra, J. A.; Schouten, A.; Kroon, J. Structural studies of the system trans-azobenzene/trans-stilbene. II. A reinvestigation of the disorder in the crystal structure of trans-stilbene, C14H12. *Acta Crystallographica Section C* **1984**, *40*, 428–431.

[194] Hoekstra, A.; Meertens, P.; Vos, A. Refinement of the crystal structure of trans-stilbene (TSB). The molecular structure in the crystalline and gaseous phases. *Acta Crystallographica Section B* **1975**, *31*, 2813–2817.

[195] Kwasniewski, S. P.; Claes, L.; François, J.-P.; Deleuze, M. S. High level theoretical study of the structure and rotational barriers of trans-stilbene. *The Journal of Chemical Physics* **2003**, *118*, 7823–7836.

[196] Brown, J. S.; Collins, A.; Duguid, P. Situated Cognition and the Culture of Learning. *Educational Researcher* **1989**, *18*, 32–42.

[197] Orgill, M. Situated Cognition. In *Theoretical Frameworks for Research in Chemistry/Science Education*; Bodner, G. M., Orgill, M., Eds.; Prentice Hall: Upper Saddle River, N.J., 2007; pp 187–203.

[198] Lave, J. *Cognition in Practice: Mind, Mathematics and Culture in Everyday Life*; Cambridge University Press: Cambridge, U.K., 1988.

[199] Brown, J. S.; Duguid, P. *The Social Life of Information*; Harvard Business School Press: Boston, M.A., 2000.

[200] Wilson, A. L. The Promise of Situated Cognition. *New Directions for Adult and Continuing Education* **1993**, *57*, 71–79.

[201] Sadler, T. D. Situated Learning in Science Education: SocioScientific Issues as Contexts for Practice. *Studies in Science Education* **2009**, *45*, 1–42.

[202] Bretz, S. L. Novak's Theory of Education: Human Constructivism and Meaningful Learning. *Journal of Chemical Education* **2001**, *78*, 1107–1115.

[203] Ausubel, D. P. *The Psychology of Meaningful Verbal Learning*; Grune and Stratton: New York, N.Y., 1963.

[204] Lombardi, M. M. Authentic Learning for the 21st Century: An Overview. *Educause Learning Initiative* **2007**, *1*, 1–12.

[205] Vázquez, A. V.; McLoughlin, K.; Sabbagh, M.; Runkle, A. C.; Simon, J.; Coppola, B. P.; Pazicni, S. Writing-To-Teach: A New Pedagogical Approach To Elicit Explanative Writing from Undergraduate Chemistry Students. *Journal of Chemical Education* **2012**, *89*, 1025–1031.

[206] Pavelich, M. J.; Abraham, M. R. Guided Inquiry Laboratories for General Chemistry Students. *Journal of College Science Teaching* **1977**, *7*, 23–26.

[207] Farrell, J. J.; Moog, R. S.; Spencer, J. N. A Guided-Inquiry General Chemistry Course. *Journal of Chemical Education* **1999**, *76*, 570–574.

[208] Gottfried, A. C.; Sweeder, R. D.; Bartolin, J. M.; Hessler, J. A.; Reynolds, B. P.; Stewart, I. C.; Coppola, B. P.; Holl, M. M. B. Design and Implementation of a Studio-Based General Chemistry Course. *Journal of Chemical Education* **2007**, *84*, 265–270.

[209] Varma-Nelson, P.; Coppola, B. P. Team Learning. In *Chemist's Guide to Effective Teaching*; Pienta, N., Cooper, M. M., Greenbowe, T., Eds.; Pearson: Saddle River, N.J., 2005; pp 155–169.

[210] Prince, M. Does Active Learning Work? A Review of the Research. *Journal of Engineering Education* **2004**, *93*, 223–231.

[211] Coppola, B. P.; Daniels, D. S.; Pontrello, J. Using Structured Study Groups to Create Chemistry Honors Sections. In *Student Assisted Teaching and Learning*; Miller, J., Groccia, J., Dibiasio, D., Eds.; Anker: New York, N.Y., 2001; pp 116–122.

[212] Wolfram Demonstrations Project Home Page. http://demonstrations.wolfram.com.

[213] Compute-to-Learn Home Page. http://umich.edu/~pchem/compute-to-learn.html.

[214] Choi, J.-I.; Hannafin, M. Situated Cognition and Learning Environments: Roles, Structures, and Implications for Design. *Educational Technology Research and Development* **1995**, *43*, 53–69.

[215] Sawyer, R. K. Optimising Learning: Implications of Learning Sciences Research. In *Innovating to Learn, Learning to Innovate*; Grandrieux, D., Shadoian, V., Eds.; OECD Publishing: Paris, France, 2008; pp 45–65.

[216] Wolfram Mathematica. Customer Stories. http://www.wolfram.com/mathematica/customer-stories/, (accessed Jul 2017).

[217] Wolfram Demonstrations Project. Heat Flow Between Two Reservoirs. http://demonstrations.wolfram.com/HeatFlowBetweenTwoReservoirs/, (accessed Jul 2017).

[218] Adams, W. K.; Wieman, C. E.; Perkins, K. K.; Barbera, J. Modifying and Validating the Colorado Learning Attitudes about Science Survey for Use in Chemistry. *Journal of Chemical Education* **2008**, *85*, 1435–1439.